

Optical Designs for Improved Solar Cell Performance

Thesis by
Emily Dell Kosten

In Partial Fulfillment of the Requirements
for the Degree of
Doctor of Philosophy



California Institute of Technology
Pasadena, California

2014

(Defended May 15, 2014)

© 2014
Emily Dell Kosten
All Rights Reserved

To Mom and Dad, who always encouraged my questions.

Acknowledgements

I am very grateful to the many people who helped make this thesis possible. Most importantly, I was very fortunate to have Harry Atwater as my adviser. He was endlessly supportive and enthusiastic, and his ideas and advice were crucial to much of this work. In addition, Harry taught me so much about crafting a paper and telling the story behind the science. Perhaps most importantly, though, the kind, collaborative research group he established was a wonderful place to work for five years.

The other students and post-docs in the Atwater group have been wonderful collaborators and friends. While I am very grateful to all of the folks who helped create the friendly atmosphere in the group, there are many who require specific mention. First, Greg Kimball taught me how to be a grad student during my first few months in the group. I was also very fortunate to have Mike Deceglie, Adele Tamboli, Morgan Putnam, Dennis Callahan, Matt Sheldon, Victor Brar, and Dagny Fleischman as my officemates over the years. Mike, Adele, and Matt were very helpful as I was starting out, and all my officemates provided lots of useful and fun discussion.

Later on, the full spectrum team, consisting of Matt Escarra, Cris Flowers, John Lloyd, Sunita Darbe, Kelsey Whitesell, Michelle Dee, Carissa Eisler, and Emily Warman, became close collaborators as well as a lovely group of friends. I am particularly grateful to John for his significant contributions to the light trapping filtered concentrator work, especially the ray tracing. Cris also provided significant Python help which was crucial to automating the ray tracing work. Emily contributed substantially to the light trapping filtered concentrator work with cell bandgap optimizations, multijunction code, and detailed balance calculations. The advice and technical help she provided with the GaAs experiments, particularly contacting, were crucial. I have also very much enjoyed our chats over tea. In addition to our collaboration on the full spectrum project, Carissa provided significant expertise with photoluminescence measurements and sputtering, helpful discussion, and funny cat stories.

Jeff Bosco, Chris Chen, Naomi Coronel, Hal Emmer, Jim Fakonas, and Sam Wil-

son all entered the group at the same time as I did. I have very much appreciated their friendship and help over the years. In particular, Hal provided significant useful discussion on silicon solar cells, and Jeff and Sam were very helpful on device physics and fabrication questions. Carrie Hoffmann, Vivian Ferry, Imogen Pryce, Stan Burgos, Mike Kelzenberg, and Dan Turner-Evans provided significant mentorship and advice, with particular assistance from Dan and Mike on the silicon microwires project. Carrie was also very helpful in her role as assistant director of the LMI-EFRC and adviser to the full spectrum project, and provided the LaTeX template files for this thesis. I've also appreciated technical help and discussions with Will Whitney, Ana Brown, and Nick Batara.

Jennifer Blankenship, Tiffany Kimoto, Lyra Haas, and April Neidholdt provided invaluable administrative support, as well as many enjoyable chats over the years. Their help with the administrative side was crucial to my graduate school experience. Within the applied physics department, Christy Jenstad and Mabel Chik were also very kind and helpful with purchasing and administration. Donna Driscoll, the physics department coordinator, provided invaluable assistance as I navigated classes, qualifying exams, candidacy, and finally the thesis and defense.

The other members of my committee, Michael Cross, Michael Roukes, and Keith Schwab, have been generous with their time and feedback over the years. I've also very much appreciated advice from Neil Fromer, about both science and broader career questions. This work also benefited significantly from collaborators within the LMI-EFRC, particularly Emily Warren in the Lewis group at Caltech, Owen Miller in the Yablonovitch group at Berkeley, and Paul Braun and his group at UIUC. Collaboration with Albert Polman and his group at FOM AMOLF in Amsterdam has also proved highly productive. Albert's encouragement for my work on angle restriction in silicon was particularly appreciated, as was assistance from Bonna Newman, Piero Spinelli, and James Parsons in his group. Brendan Kayes at Alta Devices was very generous with samples and advice, and his cells were crucial to the experimental work in GaAs presented in this thesis. Finally, John Geisz, Myles Steiner, and Daniel Friedman at NREL were helpful in discussing the details of GaAs cells, and providing

samples.

Beyond my work friends, I've also greatly enjoyed the wonderful group of friends I've found in Pasadena. Emzo de los Santos, Branimir Čačić, Nate Glasser, Stephanie Barnes, Greg Loos, Betty Wong, Emily Capra, and Jackson Cahn were always up for boardgames, adventurous meals, and trivia, providing many a welcome break from work. I've also been lucky enough to have several old and dear friends, Carolyn Brennan, Katie Gose, and Leo Ungar, in Pasadena during graduate school, and it has been wonderful to spend time with them on a regular basis.

Finally, I'd like to thank my family. My parents introduced me to science and have always encouraged me. I'm very grateful for all their love, support, and interest in my work. I always look forward to seeing and hearing from my sisters, Sarah and Margaret. I really appreciate their love, and taking the time to visit and chat despite their own busy lives. Finally, I'd like to thank my husband, Joe Zipkin. He has been wonderfully helpful and loving through graduate school. I don't know what I would have done without his care and support. I love you so, honey, and I'm so grateful for our little family of you, me, and the kitty.

Emily D. Kosten

May 2014

Pasadena, CA

Abstract

The solar resource is the most abundant renewable resource on earth, yet it is currently exploited with relatively low efficiencies. To make solar energy more affordable, we can either reduce the cost of the cell or increase the efficiency with a similar cost cell. In this thesis, we consider several different optical approaches to achieve these goals. First, we consider a ray optical model for light trapping in silicon microwires. With this approach, much less material can be used, allowing for a cost savings. We next focus on reducing the escape of radiatively emitted and scattered light from the solar cell. With this angle restriction approach, light can only enter and escape the cell near normal incidence, allowing for thinner cells and higher efficiencies. In Auger-limited GaAs, we find that efficiencies greater than 38% may be achievable, a significant improvement over the current world record. To experimentally validate these results, we use a Bragg stack to restrict the angles of emitted light. Our measurements show an increase in voltage and a decrease in dark current, as less radiatively emitted light escapes. While the results in GaAs are interesting as a proof of concept, GaAs solar cells are not currently made on the production scale for terrestrial photovoltaic applications. We therefore explore the application of angle restriction to silicon solar cells. While our calculations show that Auger-limited cells give efficiency increases of up to 3% absolute, we also find that current amorphous silicon-crystalline silicon heterojunction with intrinsic thin layer (HIT) cells give significant efficiency gains with angle restriction of up to 1% absolute. Thus, angle restriction has the potential for unprecedented one sun efficiencies in GaAs, but also may be applicable to current silicon solar cell technology. Finally, we consider spectrum splitting, where optics direct light in different wavelength bands to solar cells with band gaps tuned to those wavelengths. This approach has the potential for very high efficiencies, and excellent annual power production. Using a light-trapping filtered concentrator approach, we design filter elements and find an optimal design. Thus, this thesis explores silicon microwires, angle restriction, and spectral splitting as different optical approaches for improving the cost and efficiency of solar cells.

Contents

List of Figures	xii
List of Tables	xv
1 Introduction	1
1.1 Motivation	1
1.2 Solar Cell Fundamentals	2
1.2.1 Solar Cell Structure	2
1.2.2 Current: Absorption and Carrier Collection	3
1.2.3 Current-Voltage Relationship	6
1.3 Optics Background	7
1.3.1 Ray Optics	7
1.3.2 Lambertian Light Trapping Surfaces	8
1.3.3 Interference-based Optical Coatings	10
1.4 Overview of Thesis	11
2 Light Trapping in Silicon Microwires	13
2.1 Motivation	13
2.2 Modeling Wire Array Intensity Enhancement under Isotropic Illumination	14
2.2.1 Model Set-up: Balancing Fluxes	14
2.2.2 Evaluation of Side Losses with a Radial Escape Approximation	18
2.2.3 Evaluating Side Absorption: Shadowing	20

2.3	Results for Wire Array Intensity Enhancement under Isotropic Illumination	21
2.4	Modeling Wire Array Intensity Enhancement with a Lambertian Back Reflector	23
2.4.1	Governing Equation: Back Reflector Model	23
2.4.2	Evaluating Side Loss with Reflector Scattering	25
2.4.3	Evaluating Side Absorption with Reflector Scattering	27
2.5	Results for Wire Array Intensity Enhancement with a Lambertian Back Reflector	29
2.6	Comparison of Model with Experimental Data	31
2.6.1	Including Absorption in Ray Optics Model	31
2.6.2	Experimental Methods	32
2.6.3	Comparison of Model and Experiment: The Importance of Wave Optical Effects	33
2.7	Conclusions	35
3	Modeling the Effects of Angle Restriction	37
3.1	Angle Restriction and Photon Entropy	37
3.2	Enhanced Light Trapping and Photon Recycling	40
3.3	Detailed Balance Models	41
3.3.1	Cells in the Radiative Limit	41
3.3.2	Accounting for Non-Radiative Losses	44
3.4	Absorptivity in Light Trapping and Planar Cells	45
3.4.1	Accounting for Modal Structure	45
3.4.2	Absorption in a Light Trapping Cell with Non-Ideal Back Reflector	46
3.4.3	Parasitic Absorption of Emitted Light in a Light Trapping Cell	48
3.4.4	Absorption in a Planar Cell	49
4	Angle Restriction in GaAs Solar Cells	51
4.1	Motivation	51

4.2	Angle Restriction in a Light Trapping GaAs Cell: Limits to Efficiency	52
4.2.1	Cell in the Radiative Limit	52
4.2.2	Effect of Auger Recombination	53
4.3	Ideal and Non-Ideal Back Reflectors for a Light Trapping Cell	55
4.3.1	Effect of a Non-Ideal Back Reflector	55
4.3.2	Dielectric Mirrors Approaching Unity Reflectivity	56
4.4	Comparison with a Planar Cell Geometry	58
4.5	Comparison to Previous Work: The Radiative Efficiency Approach	58
4.6	Radiative Efficiency in Current GaAs Cell Technology	62
4.7	Broadband Angle Restrictor Designs	63
4.8	Narrowband Angle Restrictor Design	67
4.9	Conclusions	75
5	Experimental Demonstration of Enhanced Photon Recycling in GaAs	
	Solar Cells	77
5.1	Motivation	77
5.2	Narrowband Multilayer Angle Restrictor	79
5.3	Dark Current Measurements	82
5.4	Voltage Enhancements Under Illumination	84
5.5	Modified Detailed Balance Model	86
5.6	Variable Angle Restrictor Coupling	89
5.7	Bandgap Raising and Angle Restriction Effects	92
5.8	Materials and Methods	92
5.8.1	Cell Contacting and Characterization	92
5.8.2	Optical Coupler Fabrication and Characterization	93
5.8.3	Current-Voltage Measurements	94
5.8.4	Implementation of the Modified Detailed Balance Model	95
5.8.5	Gradual Coupling Measurements	96
5.9	Conclusions	96

6	Angle Restriction in Silicon Solar Cells	98
6.1	Motivation	98
6.2	Effects of Angle Restriction in Ideal and Realistic Silicon Cells	101
6.2.1	Angle Restriction in Ideal Cells	101
6.2.2	Angle Restriction in Realistic Cells	103
6.2.3	Angle Restriction with External Concentration	111
6.3	Angle Restrictor Designs	114
6.3.1	Narrowband Angle Restrictor	115
6.3.2	Broadband Angle Restrictor	117
6.4	Conclusions	120
7	Light-Trapping Filtered Concentrator For Spectral Splitting	122
7.1	Motivation	122
7.2	The Light Trapping Filtered Concentrator	126
7.3	Basic Design Considerations: The Multipass Model	127
7.3.1	The Thick Slab Assumption	127
7.3.2	Initial Subcell Optimization	131
7.3.3	Reducing Probability of Slab Escape: Design Tradeoffs	131
7.4	Designing Omnidirectional Filters	133
7.5	Optimizing Geometry and Filter Selection: Ray Trace Results	138
7.5.1	Filter Selection	138
7.5.2	Subcell Re-Optimization	140
7.5.3	Angle Restrictor Geometry Optimization	143
7.6	Conclusions	144
8	Conclusions and Outlook	146
A	Detailed Balance Code for GaAs	150
B	Detailed Balance Code for Silicon	155

List of Figures

1.1	Solar Cell Schematic: p-n Junction.	2
1.2	Solar Cell Bandgap and Current	4
1.3	Light Trapping and Planar Geometry	5
1.4	Current-Voltage Curve	6
1.5	The $2n^2$ Light Trapping Limit	9
1.6	Reflectivity of Periodic and Aperiodic Thin Film Multilayers	10
2.1	Schematic: Microwire Array without Back Reflector	17
2.2	Light Trapping Factor Variation with Microwire Array Filling Fraction	22
2.3	Schematic: Microwire Array with Lambertian Back Reflector	24
2.4	Variation of Power with Array Filing Fraction	30
2.5	Comparison of Ray Optics Model to Experimental Absorption Measurement	34
3.1	Photon Entropy Increase in a Conventional Solar Cell	37
3.2	Photon Entropy in Concentrator and Angle Restrictor Systems	39
3.3	Light Trapping and Photon Recycling with Angle Restriction	40
3.4	Balancing Photon Fluxes in the Detailed Balance Model	42
4.1	Angle Restriction in a Light Trapping GaAs Cell	54
4.2	Broadband Omnidirectional Dielectric Reflectors	57
4.3	Angle Restriction in a Planar GaAs Cell.	59
4.4	Angle Restriction and Cell Geometry: Radiative Efficiency Model	61
4.5	Broadband Angle Restrictor Designs	65

4.6	Rugate Angle Restrictor Design	69
4.7	Rugate Angle Restrictor Calculated Reflectivity	71
4.8	Current Effects of Rugate Design	72
4.9	Predicted Efficiency with Rugate Design	73
4.10	Predicted Efficiency with Rugate Design and Concentration	74
5.1	Enhanced Photon Recycling in a Planar GaAs Cell	80
5.2	Narrowband Dielectric Angle Restrictor Design and Fabrication	81
5.3	Dark Current Measurements and Fits	83
5.4	Voltage Increase with Current Losses	85
5.5	Voltage Increase with Equalized Currents	87
5.6	Loss of Emitted Light From Sides for Variable Coupling	90
5.7	Voltage Effects of Variable Angle Restrictor Coupling	91
6.1	Angle Restriction in Silicon: Light Trapping	99
6.2	Effect of Angle Restriction in Auger Limited Silicon	104
6.3	Bulk Lifetime and Surface Recombination Estimation: IBC Cells	107
6.4	Bulk Lifetime and Surface Recombination Estimation: HIT Cells	108
6.5	Angle Restriction in HIT and IBC Cells	110
6.6	Effect of Bulk Lifetime, Back Reflectivity, and Surface Recombination in Silicon Cells	112
6.7	Effect of External Concentration with Angle Restriction	114
6.8	Effect of Narrowband Angle Restrictor Design	116
6.9	Effect of Broadband Angle Restrictor Design	119
7.1	Efficiency Increases with Many Solar Cell Junctions	124
7.2	Light-Trapping Filtered Concentrator	126
7.3	Monte-Carlo Model to Determine Dielectric Slab Thickness	128
7.4	Optical Efficiency with Multipass Model	129
7.5	Slab Probability of Escape: Acceptance Angle and Refractive Index	132
7.6	Nearly Omnidirectional Long Pass Filter	134

7.7	Parasitic Loss and Transmission Trade-offs	135
7.8	Varying Cutoff Wavelength	137
7.9	Reflectivity of Selected Filter Set	139
7.10	Photon Flux at Each Subcell	142
7.11	Angle Restrictor Optimization Sweep	143
7.12	Variation of External Concentration	144

List of Tables

6.1	Cell Parameters for Ideal and Realistic Cell Models	106
7.1	Sets of Subcells Optimized for AM 1.5D	130
7.2	Subcells Optimized for Resulting Photon Flux	141

Portions of this thesis have been drawn from the following publications:

“Limiting Light Escape Angle in Silicon Photovoltaics: Ideal and Realistic Cells.” E. D. Kosten, B. K. Newman, J. V. Lloyd, A. Polman and H. A. Atwater, in preparation.

“Experimental demonstration of enhanced photon recycling in angle-restricted GaAs solar cells.” E. D. Kosten, B. M. Kayes, and H. A. Atwater, *Energy & Environmental Science* **7**, 1907-1912 (2014).

“Spectrum splitting photovoltaics: Light trapping filtered concentrator for ultrahigh photovoltaic efficiency.” E. D. Kosten, J. Lloyd, E. Warmann and H. A. Atwater, *Proceedings of the 39th IEEE Photovoltaic Specialists Conference (PVSC)* 3053-2057 (2013).

“Highly efficient GaAs solar cells by limiting light emission angle.” E. D. Kosten, J. H. Atwater, J. Parsons, A. Polman, and H. A. Atwater, *Light: Science & Applications* **2**, e45 (2013).

“Ray optical light trapping in silicon microwires: exceeding the $2n^2$ intensity limit.” E. D. Kosten, E. L. Warren, and H. A. Atwater, *Optics Express* **19**, 3316-3331 (2011).

Chapter 1

Introduction

1.1 Motivation

Solar energy is the world's most abundant source of renewable energy. With an incoming power of 1.2×10^5 terawatts, the solar resource dwarfs current worldwide energy consumption, estimated at 13 terawatts [1]. Despite the abundance of this renewable resource, fossil fuels provide greater than 80% our energy [1]. While previously the high cost of photovoltaics prevented more widespread adoption, recent developments in the Chinese solar cell industry have greatly increased production and reduced price. In fact, current module prices have allowed photovoltaics to achieve a levelized cost of energy similar to coal and natural gas, though the long-term sustainability of such prices is a matter of debate [2]. However, further cost reductions may yet be required for solar energy to become a substantial part of the energy portfolio, as these cost estimates do not include the storage necessitated by the intermittency of the solar resource.

In reducing the cost of photovoltaic energy production, two approaches have been pursued. The first has focused on novel materials, such as organic semiconductors, quantum dots, and semiconductor nanowires, that could lead to cells that are substantially cheaper than current technologies but with somewhat lower efficiencies. The silicon microwires discussed in Chapter 2 are an example of such an approach, where the goal is to use microwires to reduce the cost of the cell significantly with a relatively small reduction in efficiency relative to crystalline silicon solar cells. An alternative approach is to improve the efficiency of the cell while attempting to minimize any associated cost increases. If efficiency can be increased without significant

increased cell cost, the cost per Watt will be reduced, as less cell area is required to produce the same amount of power. Furthermore, “balance of systems” costs, such as permitting, land, installation, and structural supports, are approximately half of the cost of a photovoltaic installation [3]. As many of these costs scale with area, improving cell efficiency also reduces balance of systems costs. With the exception of Chapter 2, this thesis will focus primarily on increasing efficiency for high performing cells as a means to reduce cost. The bulk of this thesis focuses on restricting the angles of emitted light to improve efficiency in gallium arsenide (GaAs) and silicon solar cells, two high performing materials. Finally, in the last chapter, we consider splitting light into separate spectral bands to improve the efficiency of high performing III-V solar cell materials.

1.2 Solar Cell Fundamentals

1.2.1 Solar Cell Structure

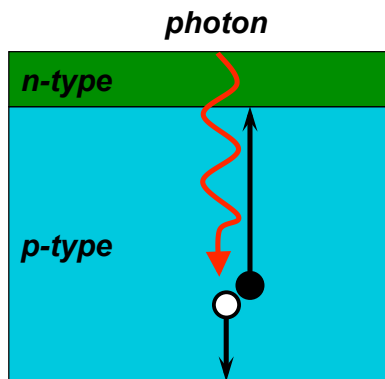


Figure 1.1. Photons are absorbed by a solar cell to generate electrons and holes. These generated charge carriers are collected by a p-n junction, as shown above, or by some other form of selective contact.

Solar cells made from inorganic semiconductors often consist of a p-n junction, as shown in Figure 1.1. The basic concept is that incoming light is absorbed in the semiconductor and the resulting electrons and holes are collected by the junction.

While Figure 1.1 illustrates a planar p-n junction, not all cells utilize such a geometry. Furthermore, a p-n junction is not actually required, as all that is necessary are selective contacts to collect the electrons and holes separately. In silicon cells with an interdigitated back contact, for example, the bulk of the semiconductor has very low doping, and alternating n-type and p-type heavily doped regions at the back of the cell provide selective contacts to collect the electrons and holes respectively [4]. Finally, while many solar cells use homojunctions, where the selective contacts utilize the same material as the primary cell absorber, heterojunctions may also be utilized, where the selective contacts are formed from a different material than the primary absorber. Some III-V cells utilize this approach, as well as HIT (heterojunction with intrinsic thin-layer) silicon cells, where amorphous silicon is used to form the selective contact [5, 6].

1.2.2 Current: Absorption and Carrier Collection

The absorption in a solar cell is determined by the semiconductor bandgap. As shown in Figure 1.2, only photons with energy larger than the solar cell bandgap are absorbed by the solar cell, which limits the efficiency. In addition, high energy photons in this region are not utilized very efficiently, as the resulting carriers thermalize to the band edge, and are collected at the same voltage as lower energy photons. The short circuit current of a solar cell corresponds directly to the number of absorbed photons. Thus, the limiting short circuit current is determined by the number of photons in the solar spectrum that are above the band gap of the solar cell.

While the limiting short circuit current (I_{sc}) is determined by the band gap and solar spectrum, the actual short circuit current depends on how effectively the solar cell absorbs the light above the bandgap. The absorptivity at a given wavelength is determined by the path length of light within the solar cell, as well as the absorption length of the semiconductor. Direct bandgap semiconductors, such as GaAs, have short absorption lengths, and thus cells need only be a few microns thick to absorb most of the incoming light. Indirect bandgap semiconductors, such as Si, have much longer absorption lengths, and thus cells are on the order of 100 microns thick.

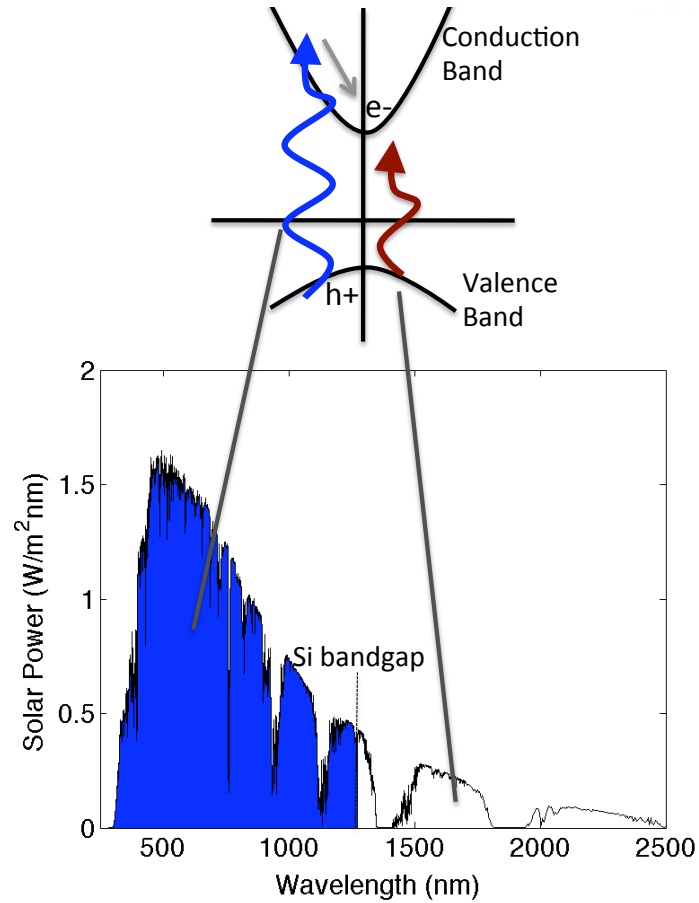


Figure 1.2. Only photons with energy larger than the semiconductor bandgap (shown in blue) are absorbed in the solar cell. This region is marked in blue for silicon in the plot of the AM 1.5G solar spectrum (below). Photons with energy above the band gap generate electron hole pairs that thermalize (gray arrow) to the band edge. Thus, high energy photons lose a substantial portion of their energy. Photons with energy less than the band gap (shown in red) are not absorbed in the semiconductor, and do not contribute to the solar cell current.

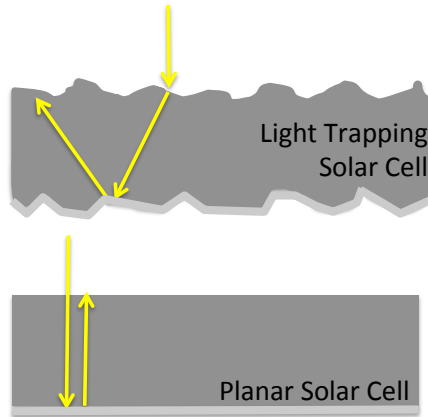


Figure 1.3. A light trapping geometry (top) enhances the light path length and resulting absorption relative to a planar geometry (bottom). Both cells have back reflectors.

Despite the thickness of current silicon cells, absorption is weak enough that light trapping is required to enhance the path length of light within the cell. Using a light trapping texture scatters the light, so it is trapped by total internal reflection, as shown in Figure 1.3. As will be further discussed in Section 1.3.2, this offers a significant path length enhancement relative to a planar cell. For direct bandgap materials, dual pass absorption, as shown in Figure 1.3, is sufficient, and cells generally utilize a planar geometry. A planar geometry also reduces surface recombination and easily accommodates epitaxially grown window layers, which are crucial for high quality III-V materials.

In a solar cell, it is key to collect the generated carriers, by either drift or diffusion, before they recombine. Recombination can occur at bulk trap states, as in Shockley-Read-Hall recombination, as well as at surfaces. These processes depend on the quality of the solar cell material and surface passivation layers. In addition, two intrinsic recombination processes occur within the bulk of the material. Radiative recombination occurs when an electron and hole recombine to form a photon, and is the inverse process to absorption. Auger recombination is a three particle process involving either two electrons and a hole or two holes and an electron. The inverse process to impact ionization, it involves the recombination of the electron hole pair

and the transfer of energy to the remaining carrier. This high energy carrier then thermalizes to the band edge, ultimately producing heat.

1.2.3 Current-Voltage Relationship

At short circuit, all photogenerated carriers are collected before excess carrier population can build up within the cell. However, the excess carrier population within the cell leads to the cell voltage, and thus there is no voltage or power production at open circuit. At open circuit, in contrast, no carriers are collected, so the cell does not generate current or power. At open circuit, the excess carrier population and open circuit voltage (V_{oc}) are determined by the balance between absorption and recombination within the cell. (This will be discussed more fully in Chapter 3.) As radiative recombination and absorption are set by the bandgap, V_{oc} is generally 400-500 mV lower than the bandgap for high quality cells. A larger V_{oc} -bandgap offset thus indicates that more non-radiative recombination is occurring in the cell.

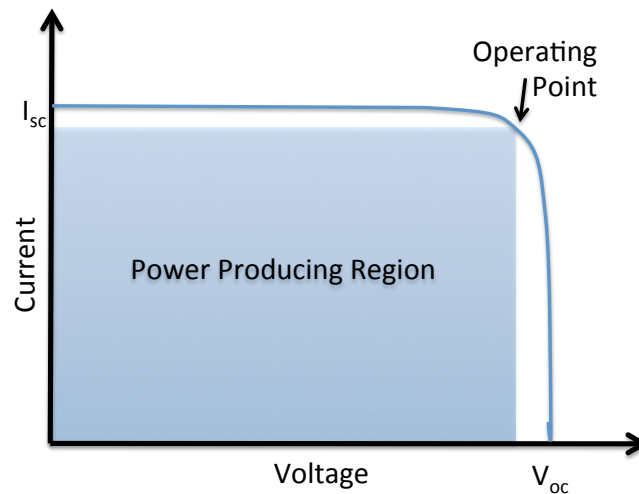


Figure 1.4. A schematic current-voltage curve illustrates short circuit current, I_{sc} , open circuit voltage, V_{oc} , and the maximum power point where the cell operates. The area of the power producing region corresponds to the power produced at the operating point.

While the short and open circuit conditions provide valuable information about

absorption and recombination in the cell, neither produce any power. The shape of the current-voltage relationship, or I-V curve, may be approximated as:

$$I(V) \approx I_{sc} - I_o e^{qV/kT} \quad (1.1)$$

where I is the current, V the voltage, I_o the dark or recombination current, q the electron charge, k the Boltzmann constant, and T the temperature. Because of the exponential shape, a small reduction in voltage relative to V_{oc} , allows for currents near I_{sc} , as is shown schematically in Figure 1.4. Thus, a voltage somewhat less than open circuit allows for maximum power production in the cell. This voltage is known as the maximum power or operating point, and the voltage is referred to as the operating voltage (V_{op}) of the cell. The power generated by the cell at the operating point (P_{op}) is then:

$$P_{op} = I(V_{op})V_{op} = FF I_{sc} V_{oc} \quad (1.2)$$

where FF is the fill factor of the cell, or the area of the rectangle representing the power producing region at the maximum power point divided by I_{sc}, V_{oc} product. The fill-factor indicates how “square” the I-V curve is and increased series resistance within the cell tends to degrade the fill-factor. The efficiency (η) of the cell is:

$$\eta = \frac{P_{op}}{P_{sun}} = \frac{FF I_{sc} V_{oc}}{P_{sun}} \quad (1.3)$$

where P_{sun} is the power in the solar spectrum.

1.3 Optics Background

1.3.1 Ray Optics

Ray optics refers to the interaction of light with structures that are significantly larger than the wavelength of light in the material. One rule of thumb is that the relevant length scale of a structure should be at least ten times larger than the wavelength of light in the material. This is very relevant when modeling the optics within solar cells.

For example, when modeling silicon solar cells, the largest wavelength of interest is about 1100 nm, and the refractive index is about 3.5. Thus, the wavelength of light in the material is about 300 nm, and we can feel confident using ray optics assumptions for cells where the minimum dimension is at least 3 μm .

For cells that are thinner than the ray optic limit, optical guided modes develop within the thickness of the cell. These guided modes are based on the allowed solutions to Maxwell's equations, and more guided modes are present for thicker cells. Once cells are in the ray optic limit, there are so many guided modes that they become a continuum of optical states corresponding to angles of light that lie outside the escape cone defined by total internal reflection. For cells thinner than the ray optic limit, we must account for the finite number of guided modes in considering light trapping within the cell. This will be discussed in more detail in Section 3.4.

For structures in the ray optic limit, ray tracing may be used to model the optical properties. These simulations consist of starting a certain number of rays, and using the Fresnel equations to follow their progress as they interact with various surfaces. Receivers are used to detect the final location of each ray and determine the performance. Both home-built and commercial ray trace software was utilized in this work.

1.3.2 Lambertian Light Trapping Surfaces

When considering light trapping, Lambertian textured surfaces are often considered as an ideal light trapping structure. These surfaces scatter light with equal brightness in all directions, similar to a white sheet of paper. Alternatively, the intensity is proportional to the cosine of the angle between the surface normal and the direction of observation. For solar cells, Lambertian scattering leads to significant light trapping benefits, including an approximately 50 times path length enhancement, for solar cells in the ray optic limit [7].

To understand light trapping with a Lambertian surface, we assume that the solar cell is not absorbing for purposes of calculating the intensity of light within the cell. This is reasonable as light trapping is only important where light is weakly absorbed.

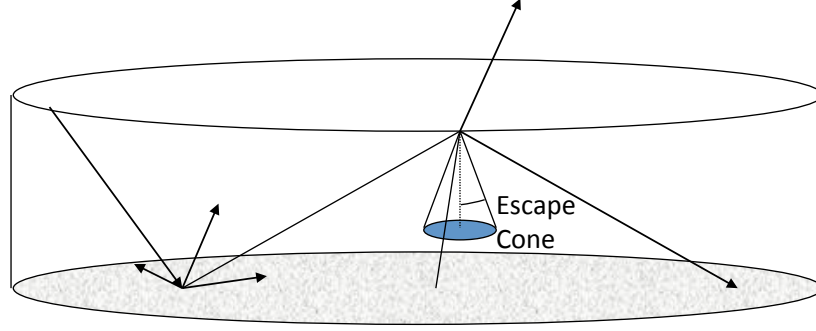


Figure 1.5. For a solar cell with a Lambertian back reflector, incoming light is scattered in all directions, but only light that is not totally internally reflected and lies within the escape cone can leave the cell. This leads to increased light intensity within the cell relative to the intensity of incoming light.

Under the principles of detailed balance, at steady state in a non-absorbing material, the light entering and escaping the material must balance. We assume an incoming light intensity I_{inc} , and a light intensity within the cell of I_{int} . However, the escape cone defined by total internal reflection allows only $1/2n^2$ of the light within the cell to escape, where n is the cell index of refraction. Thus, for the outgoing and incoming fluxes to balance:

$$I_{inc} = \frac{I_{int}}{2n^2} \quad (1.4)$$

and

$$I_{int} = 2n^2 I_{inc} \quad (1.5)$$

This is known as the ergodic light trapping limit. For a solar cell without a back reflector, the light intensity enhancement is n^2 [7].

When weak absorption is included, the absorptivity of the cell, a , is:

$$a(E) = \frac{\alpha(E)}{\alpha(E) + \frac{1}{4n^2W}} \quad (1.6)$$

where E is the energy of light for which absorptivity is being evaluated, α is the absorption coefficient, and W is the cell thickness. This can be understood intuitively as the ratio of absorption to all sources of light loss, including absorption and light

escape. We also see a $4n^2$, or approximately 50 times, path length enhancement, relative to a single pass through the cell. The additional factor of two relative to the probability of light escape is due to enhanced path length from light at oblique angles [7].

1.3.3 Interference-based Optical Coatings

In an optical thin film, interference occurs between light reflected at each interface, and the patterns of constructive and destructive interference result in the reflectivity of the film. The simplest example is a single layer anti-reflective coating, where destructive interference of reflected beams leads to enhanced transmission. The principle is similar to impedance matching in electronics. With many alternating high and low index layers in an optical coating, known as a Bragg stack, high reflectivity bands result from constructive interference of the reflections from each interface. While Bragg stacks are traditionally periodic, introducing aperiodicity into a Bragg stack can increase transmission around the reflecting band, as shown in Figure 1.6.

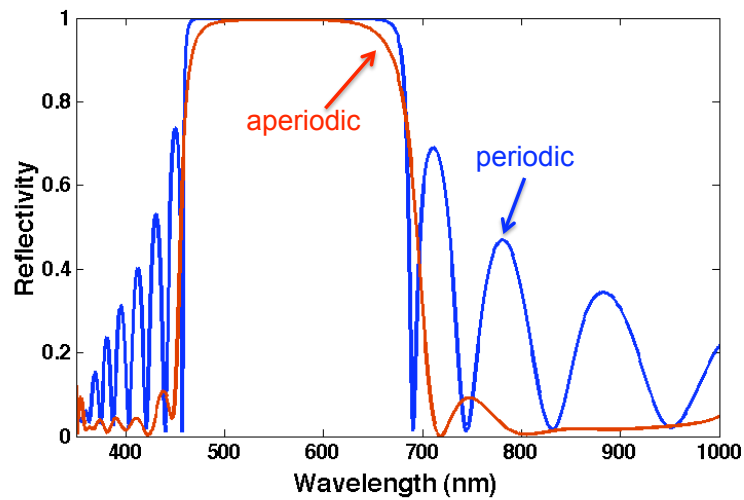


Figure 1.6. Optical multilayers with alternating high and low index layers lead to high reflectivity bands. As these two reflectance spectra show, introducing aperiodicity can increase transmission away from the reflecting bands.

To produce the interference effect, each layer in the thin film will have a thickness on the order of the wavelength of light. To model such structures, the transfer matrix method is traditionally used. In this method, the propagation of the electric field through each layer is represented by a matrix. The matrices for each layer are then multiplied together, and the resulting matrix is used to determine the electric field on either side of the optical multilayer, allowing the reflection and transmission coefficients to be determined. Essentially, this method provides a simple formalism for imposing the boundary conditions from Maxwell's equations across each interface in the multilayer.

1.4 Overview of Thesis

This thesis explores several problems related to optics and solar cells. In the second chapter, we focus on light trapping in silicon microwires, developing a ray optical model, and comparing to experimental measurements of absorption in the wires. For the rest of the thesis we focus on very high quality cells performing near the thermodynamic efficiency limits, and explore how optics can be utilized to further increase the efficiency of such cells. The bulk of the thesis, Chapters 3-6, focuses on utilizing optics that limit the angles at which light is emitted from a solar cell to enhance efficiency. Using such optics both reduces the loss of radiatively emitted light, and enhances light trapping for incoming light. In these chapters we introduce the detailed balance model used to calculate the effects of angle restriction, and explore the effects of angle restriction in both GaAs and Si for ideal and more realistic cells. We also explore various optical structures that may be used to restrict the emission angle and discuss a proof-of-concept experiment demonstrating the voltage benefits to angle restriction. Finally, the last portion of the thesis, Chapter 7, focuses on spectrum splitting, where external optics split the incoming light into spectral bands of different energies. These spectral bands are then directed onto cells with bandgaps tuned to the appropriate energy, thus reducing losses due to carrier thermalization and lack of absorption. This chapter will discuss the benefits of spectrum splitting and

then focus on one particular optical design, the light-trapping filtered concentrator, which applies many of the optical concepts discussed previously.

Chapter 2

Light Trapping in Silicon Microwires

2.1 Motivation

Silicon nanowire and microwire arrays have attracted significant interest as an alternative to traditional wafer-based technologies for solar cell applications [8-19]. Originally, this interest stemmed from the device physics advantages of a radial junction, which allows for the decoupling of the absorption length from the carrier collection length. In a planar cell, both of these lengths correspond to the thickness of the cell, and high quality material is necessary so that the cell can absorb most of the light while successfully collecting the carriers. In contrast, a radial junction offers the possibility of using lower quality, lower cost materials without sacrificing performance [12, 13]. More recently, such arrays have been found to exhibit significant light trapping and absorption properties [8-10], and this absorption has been modeled in the nanowire regime with a variety of wave optical models [15, 20-24].

As discussed previously, enhancing the light trapping and absorption within a solar cell leads to an increase in short circuit current, and light trapping is particularly important in silicon owing to the relatively low absorption in the material. Under the light trapping limit for textured planar solar cells, known as the ergodic limit, the intensity of light inside the solar cell is n^2 times the intensity of light incident upon the cell, or $2n^2$ for the case of a back-reflector, where n is the index of refraction for the cell [7]. Some very recent experimental results have suggested that nano and microwire arrays can exceed the ergodic limit [8, 9]. To explore this further, we follow the approach used to derive the ergodic limit in the planar case to find the expected light trapping and absorption for wires in the ray optics limit. This allows

us to compare to the ergodic limit and consider wires of a different scale than those considered previously.

While much of the previous work has considered nanowires in the subwavelength regime, far below the ray optics limit, large diameter microwires can be grown by vapor-liquid-solid (VLS) techniques [8]. Previous device physics modeling suggests that for efficient carrier collection wires should have diameters similar to the minority carrier diffusion length, [13] and experimental measurements show diffusion lengths for VLS grown microwires of 10 microns [25]. Because wires with such diameters could approach the ray optics limit for solar wavelengths, it seems sensible to model these structures in the ray optics regime. In addition, comparison of the ray optics model with experimental data provides insight into the relative importance of wave optics effects for wires of various diameters.

We begin by assuming there is no absorption in the wires and examine the case for isotropic illumination so that we can compare to the ergodic light trapping limit for textured, weakly absorbing solar cells with a traditional planar geometry. To make this comparison, it is also necessary to postulate textured surfaces for the wires. We then examine the case of wires on a Lambertian back reflector, which are illuminated isotropically over the upper half sphere. Finally, we add a weak absorption term and find the absorption as a function of wavelength and angle of incidence, allowing us to compare with experimental data.

2.2 Modeling Wire Array Intensity Enhancement under Isotropic Illumination

2.2.1 Model Set-up: Balancing Fluxes

We base our model on the principle of detailed balance, as was done to derive the ergodic limit for textured planar sheets, discussed in Section 1.3.2 [7]. Under detailed balance, in steady state the light escaping from the wires is set equal to the light entering the wires. To illustrate our approach and show proof of concept for the model,

we first imagine a hexagonal array of wires suspended in free space and isotropically illuminated. Furthermore, we assume that the wire surfaces are roughened such that they act as Lambertian scatterers. In other words, the brightness of the wire surfaces will be equal regardless of the angle of observation [26]. This fully randomizes the light inside the wires in the limit of low absorption, just as the roughened surfaces of planar solar cells do. The randomization of light within the wires serves to trap the light inside by total internal reflection.

With these assumptions in mind, we find the governing equation by simply balancing the inflows and outflows of light within a single wire.

$$I_{inc}2A_{end}\bar{T}_{end} + I_{inc}A_{sides}\bar{F} = \frac{I_{int}2A_{end}\bar{T}_{end}}{n^2} + \frac{I_{int}A_{sides}\bar{L}}{n^2} \quad (2.1)$$

Above, I_{inc} is the intensity of the incident radiation, I_{int} is the the intensity of light within the wires, A_{sides} is the area of the wires sides, A_{end} is the area of one wire end, and n is the index of refraction of the wire. In addition, \bar{T}_{end} is the average transmission factor through the end, \bar{L} is light from the sides which escapes the array, and \bar{F} is the incident light which enters through the sides.

The terms on the left hand side represent the energy entering the wire array, with the two terms representing the incident light which enters through the side and tops of the wire, respectively. For the top of the wire, the calculation is quite simple because there is no shadowing or multiple scattering, assuming that the wires are all the same height. Thus, we need only average transmission into the top over the incident angles to find \bar{T}_{end} . For light entering through the sides, we take into account transmission into the wire in addition to shadowing and multiple scattering. Thus, for a given incident angle, we determine \bar{F} , which gives the fraction of light transmitted through the sides, averaged over the angles of the incident radiation.

On the right hand side, we have the energy outflows. Once again, the outflows from the top are quite simple, as all light that leaves the top is lost to the array. The factor of $1/n^2$ is due to total internal reflection of the randomized light inside the wire, as Yablonoitch previously demonstrated for ergodic structures [7]. Due to the

isotropic incident radiation, the averaged transmission fractor T_{end} is the same for incident and escaping light. For losses through the sides, much of the emitted light will be transmitted into other wires, and not lost from the array. Thus, an average loss factor, \bar{L} , is found, which gives the side losses that are not transmitted into other wires.

We rearrange the above equation to find the degree of light-trapping, or I_{int}/I_{inc} .

$$\frac{I_{int}}{I_{inc}} = \frac{n^2(2A_{end}\bar{T}_{end} + A_{sides}\bar{F})}{2A_{end}\bar{T}_{end} + A_{sides}\bar{L}} \quad (2.2)$$

Note that in the limit where the area of the sides goes to zero, the light trapping factor is n^2 , which reproduces the ergodic limit for a planar textured sheet that is isotropically illuminated, as we expect. If \bar{F} is larger than \bar{L} , the light trapping in this structure could exceed the ergodic limit. This seems unlikely, however, as time-reversal invariance would suggest that $\bar{L} = \bar{F}$ because each path into the array must also be an equally efficient path out of the array. Furthermore, from a thermodynamics perspective, we expect that the light trapping in this structure should be exactly n^2 . This is because the equipartition theorem states that all the states or modes should be equally occupied in thermodynamic equilibrium, and the density of states within the wires is n^3 the of states in free space. (When calculating the intensity, it is necessary to multiply by the group velocity which goes as $1/n$, such that the intensity is increased by n^2 [7].) Thus, this case will allow us to assess the accuracy of the model and the assumptions necessary to simplify the calculation.

Averaging over all solid angles, with an appropriate intensity weighting, gives \bar{T}_{end} :

$$\bar{T}_{end} = \frac{\int_0^{2\pi} \int_0^{\pi/2} T(\phi) \cos(\phi) \sin(\phi) d\phi d\theta}{\int_0^{2\pi} \int_0^{\pi/2} \cos(\phi) \sin(\phi) d\phi d\theta} = \frac{\int_0^{2\pi} \int_0^{\pi/2} T_n \cos^2(\phi) \sin(\phi) d\phi d\theta}{\int_0^{2\pi} \int_0^{\pi/2} \cos(\phi) \sin(\phi) d\phi d\theta} = \frac{2}{3}T_n \quad (2.3)$$

where ϕ is the angle of incidence and T_n is the transmission factor at normal incidence, and where we have used the transmission factor associated with a Lambertian surface ($T_n \cos(\phi)$) [26].

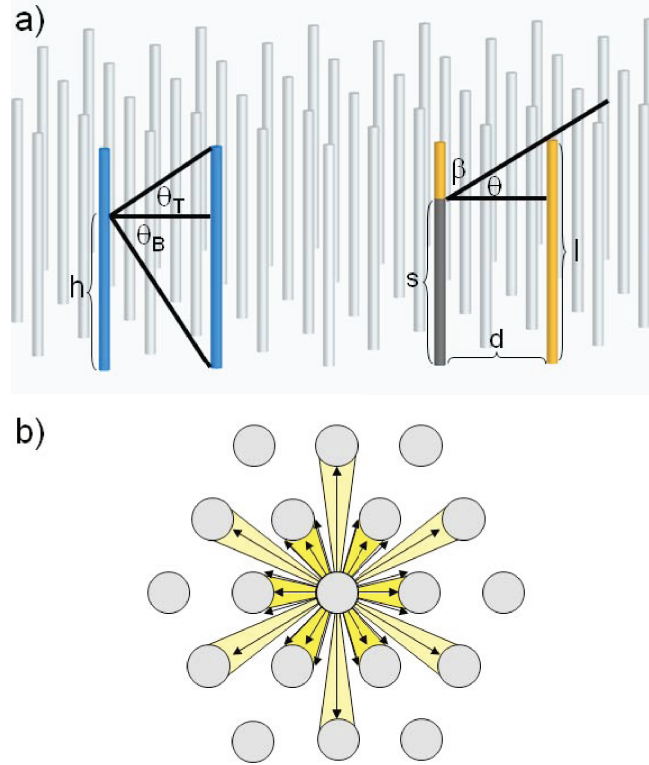


Figure 2.1. a) Schematic of the wire array for isotropic illumination. The blue wires illustrate how light escaping from the side of a wire impinges on a neighboring wire a given distance away. The orange wires illustrate how the sides of the wires are shadowed by neighboring wires for a given distance and angle of incidence. b) A top-down view of the wire array illustrates the radial escape approximation. The arrows show the directions of light escape being considered, and the yellow areas give the in-plane angle subtended by the neighboring wires, with the distinct shades indicating neighboring wires at two distinct distances. The wires farther away will have greater loss associated than the closer wires.

2.2.2 Evaluation of Side Losses with a Radial Escape Approximation

To calculate \bar{L} , we determine the fraction of light, g , escaping from the sides of a given wire that impinges on neighboring wires. Then we determine the transmission into those neighboring wires and the effect of multiple scattering from neighboring wires. To find g , we invoke a radial escape approximation where we treat each wire as if it were a line extending upward from the plane of the array. This approximation will be more accurate for low filling fraction arrays, because greater distance between the wires means that neighboring wires will more closely approximate line sources. The radial escape approximation serves to significantly simplify the treatment of the in-plane shadowing. With this assumption, we only need to calculate the portion of the in-plane angle that is subtended by wires at a given distance, and the losses associated with each distance in order to find g . As Figure 2.1b illustrates, the in-plane angle subtended by neighboring wires at a given distance is calculated geometrically.

The fraction of light that impinges on a wire a given distance away, $f(h)$, is easily calculated from geometrical arguments and the properties of Lambertian surfaces, as Figure 2.1a illustrates. To simplify the calculation we ignore the increase in wire to wire distance as the wires curve away from each other. As before, this approximation will be more accurate for lower filling fractions, where the wires are farther apart and this effect will be smaller.

$$f(h) = \frac{\int_{-\theta_B}^{\theta_T} \cos(\theta) d\theta}{\int_{-\pi/2}^{\pi/2} \cos(\theta) d\theta} = \frac{\sin(\theta_T) + \sin(\theta_B)}{2} \quad (2.4)$$

To find $g(d)$, we integrate $f(h)$ over the height of the wire and normalize.

$$g(d) = \frac{\int_0^l \sin(\theta_T) + \sin(\theta_B) dh}{2l} = \frac{\sqrt{l^2 + d^2} - d}{l} \quad (2.5)$$

Then g is an average of $g(d)$ weighted by the angles subtended at each distance.

Naturally, not all of the light which strikes a neighboring wire will be transmitted into the wire. As before, we calculate a transmission factor as a function of distance,

$T_{int}(d)$, and take a weighted average to find the overall internal transmission factor, T_{int} . Here, however, we must account for the curvature of the wire because this significantly affects the angle the transmitted light makes with the wire surface. Assuming equal brightness for the allowed in-plane and out-of-plane angles, the expression for $T_{int}(d)$ is:

$$T_{int}(d) = \frac{\int_0^l \int_{-\theta_B}^{\theta_T} \int_{-\alpha_1}^{\alpha_2} T_n \cos^2(\phi) d\alpha d\theta dl}{\int_0^l \int_{-\theta_B}^{\theta_T} \int_{-\alpha_1}^{\alpha_2} \cos(\phi) d\alpha d\theta dl} \quad (2.6)$$

where the θ 's give the bounds of the out-of-plane angles, the α 's the bounds of the in-plane angles, and ϕ is the overall angle made with the wire.

To find \bar{L} we sum the losses in each pass through the wire array. For the first pass through the wire array, $1 - g$ of light which left the wire side is lost, because it does not impinge on any of the other wires, and escapes. This is multiplied by \bar{T}_{end} because the light must leave the side of the wire before it can escape the array. On the second pass, the losses, L_2 , are as follows:

$$L_2 = \bar{T}_{end} g (1 - T_{int}) (1 - g) \quad (2.7)$$

This assumes that the reflected light has a uniform height distribution. In reality, more of the light emitted from the sides of the wires will impinge on the middle of the neighboring wire than either end, owing to the Lambertian distribution of light from the emitting wire. Thus, this assumption will overestimate the losses on succeeding passes through the array, but greatly reduces the computational intensity of the calculation by allowing for a generalization of the losses on the i th pass through the array as:

$$L_i = \bar{T}_{end} (g(1 - T_{int}))^{i-1} (1 - g) \quad (2.8)$$

This can easily be summed to give \bar{L} .

$$\bar{L} = \bar{T}_{end} (1 - g) \sum_{n=0}^{\infty} (g(1 - T_{int}))^n = \frac{1 - g}{1 - g(1 - T_{int})} \quad (2.9)$$

2.2.3 Evaluating Side Absorption: Shadowing

In calculating \bar{F} , the main additional phenomenon we must address is shadowing. As Figure 2.1a illustrates, the shadowing fraction, u , as a function of wire to wire distance and angle of incidence is:

$$u(d, \beta) = \frac{l - s}{l} = \frac{d \cot(\beta)}{l} \quad (2.10)$$

We then take a weighted average over the angle subtended at each distance to find $u(\beta)$, and also find the transmission factor for the incoming light as a function of β by averaging over all in-plane angles α .

$$T_0(\beta) = \frac{\int_{-\pi/2}^{\pi/2} T_n \cos^2(\phi) d\alpha}{\int_{-\pi/2}^{\pi/2} \cos(\phi) d\alpha} \quad (2.11)$$

As before, ϕ is the overall angle the incoming ray makes with the wire, which will depend on both α and β . Finally, we modify the multiple scattering model because light will only be reflected off the unshadowed portion of the wire, which will vary as a function of β . For the losses on the first pass through the array:

$$L_1(\beta) = u(\beta)(1 - T_0(\beta))(1 - g_1(\beta)) \quad (2.12)$$

For $i > 1$,

$$L_i(\beta) = (1 - g)u(\beta)(1 - T_0(\beta))g_1(\beta)(1 - T_1(\beta))[g(1 - T_{int})]^{i-2} \quad (2.13)$$

where L_i gives the losses on the i th bounce, as before, and T_1 and g_1 give the transmission and impingement factors associated with the light reflected from the unshadowed portion of the wires. Summing to find the total losses:

$$L_t(\beta) = u(\beta)(1 - T_0(\beta)) \left(1 - g_1(\beta) + \frac{(1 - g)g_1(\beta)(1 - T_1(\beta))}{1 - g(1 - T_{int})} \right) \quad (2.14)$$

Thus, for a given angle, β , the amount of light which is transmitted into the wires, $F(\beta)$, accounting for multiple scattering and shadowing is:

$$F(\beta) = u(\beta) - L_t(\beta) \quad (2.15)$$

Averaging over all the angles of incidence gives \bar{F} .

$$\bar{F} = \frac{\int_0^{2\pi} \int_0^{\pi/2} F(\beta) \sin^2(\beta) d\beta d\eta}{\int_0^{2\pi} \int_0^{\pi/2} \sin^2(\beta) d\beta d\eta} \quad (2.16)$$

Above, η is the polar angle, $\sin(\beta)d\beta d\eta$ is the differential solid angle, and the additional factor of sine gives the change in intensity with angle of incidence.

2.3 Results for Wire Array Intensity Enhancement under Isotropic Illumination

Inserting the expressions found above into Equation 2.2, we calculate the light trapping factor across a range of areal filling fractions, the fraction of the array covered by wires, for various wire aspect ratios. The results are given in Figure 2.2 and are indicated by the curves labeled “no back reflector”. For very large filling fractions we approach the ergodic limit, because the terms involving the wire sides become very small. We also reproduce the ergodic limit for very low filling fractions, where the radial escape approximation will be most accurate.¹ In between the results fall below the ergodic limit, likely because the side loss factor, \bar{L} , is overestimated in the radial escape approximation. Because we expect thermodynamically that the result should be n^2 , this suggests that our approximations are reasonable, especially for low filling fractions, which are more likely to be of experimental interest. We also note that our

¹Our model very slightly exceeds the ergodic limit across all aspect ratios for the smallest filling fraction. This is observed across aspect ratios, with no trend with increasing aspect ratios. The maximum amount by which the ergodic limit is exceeded is approximately 1% and is likely due to small inaccuracies in the model.

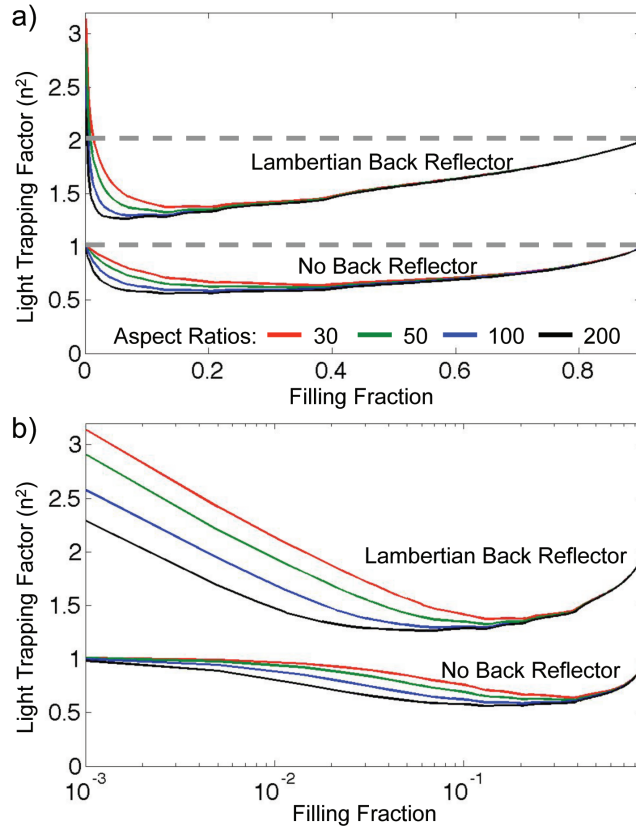


Figure 2.2. The variation of the light trapping factor, as a multiple of n^2 , as a function of areal filling fraction, for various aspect ratios (height/radius). $n=3.53$. Because we assume a cylindrical wire geometry, the maximum attainable packing fraction is approximately 90%, which corresponds to the sides of the wires touching each other. The minimum filling fraction shown is 0.1%. Both cases approach their respective ergodic limits (denoted by gray dashed lines) for large filling fractions. The no back reflector case is also very close to the ergodic limit for very small filling fractions where the radial escape approximation is accurate. Parts a and b show the same data plotted against a linear and log scale.

results are closer to the ergodic limit for smaller aspect ratios. This is likely because the terms involving the wire sides are relatively smaller, and thus inaccuracies in those terms, such as overestimating \bar{L} , will have less impact. Thus, our approach reasonably approximates the result we expect from thermodynamics, and the inaccuracies introduced by the radial escape approximation are well understood.

2.4 Modeling Wire Array Intensity Enhancement with a Lambertian Back Reflector

2.4.1 Governing Equation: Back Reflector Model

We now investigate the effect of having a Lambertian back reflector with isotropic illumination in the upper half-sphere. In this case, no light will enter or escape through the bottom ends of the wires, which are covered by the back-reflector, and light that strikes the reflector will be scattered. In the planar case, the ergodic light trapping limit for such a geometry is $2n^2$, owing to the back reflector. Additionally, it seems that this geometry would give optimal scattering, as can be understood by basic physical arguments. Experimentally, it has been found that placing scatterers within the wire array can, in combination with a back-reflector, improve the performance of the array [8, 14]. This is because scatterers prevent light which is at normal or nearly normal incidence from going between the wires and bouncing off a planar back-reflector and out of the array. Imagine that we could place scatterers at any height level within the wire array. The light that scatters upward from the scatterers near the bottom of the array will be more likely to impinge on a wire, as Figure 2.3 shows. For optimal scattering, then, the scatterers should be placed at the bottom of the array. Since a Lambertian back reflector is similar to placing scatterers on a planar back reflector, this geometry allows us to investigate an optimal scattering regime as well as providing an interesting comparison to the planar case.

The governing equation for this case once again relies on detailed balance, as

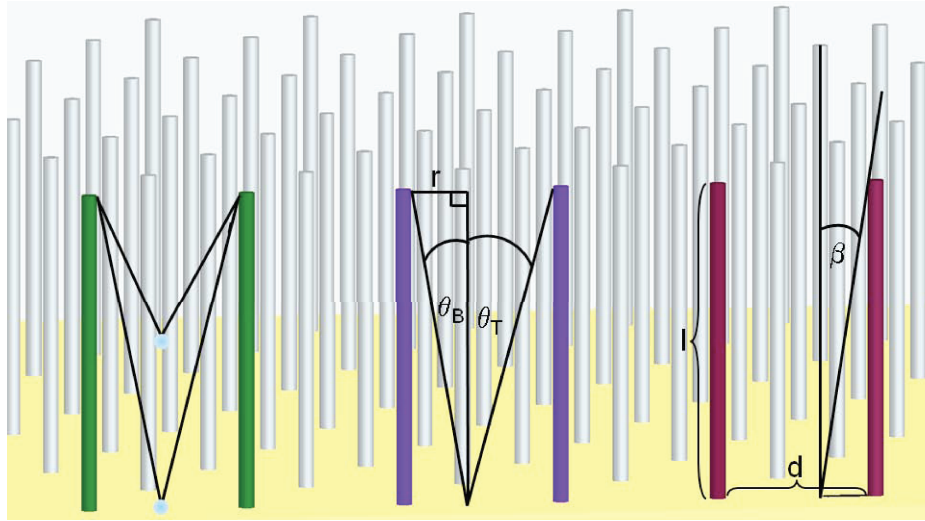


Figure 2.3. A schematic of the Lambertian back reflector case. The green wires show the effects of scatterers placed at different heights within the array. Note that for the lower scatterer light from a much smaller range of angles is able to escape. The purple wires illustrate the light which bounces off the reflector at a given point r that escapes between the surrounding wires. Between the red wires the shadowing of the reflector for incident light at a given angle and wires at a given distance is shown.

shown below.

$$I_{inc}A_{end}\bar{T}_{end} + I_{inc}A_{sides}\bar{F}' + I_{inc}A_{refl}\bar{R}' = \frac{I_{int}A_{end}\bar{T}_{end}}{2n^2} + \frac{I_{int}A_{sides}\bar{L}'}{2n^2} \quad (2.17)$$

The terms on the left give the light entering a wire, and the terms on the right give the amount of light escaping. Note that a factor of $1/2n^2$ replaces the $1/n^2$ factor because the back reflector doubles the intensity of the light within the wires [7]. In addition, \bar{L} and \bar{F} are replaced with \bar{L}' and \bar{F}' , indicating that we need to account for the Lambertian back reflector when calculating them. Finally, we note that there is a term accounting for the light that initially falls between the wires and strikes the reflector. \bar{R}' gives the fraction of the light which initially strikes the back reflector that subsequently enters a wire, accounting for shadowing and multiple scattering. With a one wire unit cell, A_{refl} , is simply the reflector area associated with a single wire. As before, we rearrange the above equation to find the relative intensities inside and outside the wire.

$$\frac{I_{int}}{I_{inc}} = \frac{2n^2(A_{end}\bar{T}_{end} + A_{sides}\bar{F}' + A_{refl}\bar{R}')}{A_{end}\bar{T}_{end} + A_{sides}\bar{L}'} \quad (2.18)$$

Once again, in the limit of zero side area, the light trapping reduces to the planar ergodic limit of $2n^2$, as expected.

2.4.2 Evaluating Side Loss with Reflector Scattering

To find the appropriate expressions for \bar{L}' we note that g and T_{int} will both be modified by the back reflector. Therefore, using the modified values of these, g' and T'_{int} , in our previous multiple scattering model gives \bar{L}' . To find g' , we tally the light lost. Half of the losses from the non-reflector case remain, corresponding to the light that escapes from the top. The other half of the non-reflector losses are multiplied by the losses associated with light bouncing off the reflector and not striking a wire, L_{refl} .

$$1 - g' = (1 - g)/2 + (1 - g)/2 * L_{refl} \quad (2.19)$$

As Figure 2.3 illustrates, we consider two wires a distance d apart, and of height l , with the light being reflected from a point r on the reflector. The fraction of light which escapes at a given location on the reflector will be

$$L(r) = \frac{\int_{-\theta_B}^{\theta_T} \cos(\theta) d\theta}{\int_{-\pi/2}^{\pi/2} \cos(\theta) d\theta} = \frac{\sin(\tan^{-1}(r/l)) + \sin(\tan^{-1}((d-r)/l))}{2} = \frac{\frac{r}{\sqrt{r^2+l^2}} + \frac{d-r}{\sqrt{(d-r)^2+l^2}}}{2} \quad (2.20)$$

Summing the light coming from all points along the two neighboring wires and accounting for the Lambertian nature of the wire surfaces, we find the intensity of light at point r :

$$I(r) = \int_0^l \cos(\eta_1) dh + \int_0^l \cos(\eta_2) dh = \int_0^l \frac{r}{\sqrt{r^2+h^2}} dh + \int_0^l \frac{d-r}{\sqrt{(d-r)^2+h^2}} dh \quad (2.21)$$

where η_1 is the angle to the horizontal made by a ray escaping the wire at a height h to strike the reflector at a point r , and η_2 is the same quantity for the other wire. Averaging over all the points between the two wires with the appropriate intensity weighting gives:

$$L_{refl}(d) = \frac{\int_0^d I(r) \left[\frac{r}{\sqrt{r^2+l^2}} + \frac{d-r}{\sqrt{(d-r)^2+l^2}} \right] dr}{2 \int_0^d I(r) dr} \quad (2.22)$$

$L_{refl}(d)$ is inserted into Equation 2.19 to find $g'(d)$. We then take a weighted average of $g'(d)$ with respect to the angle subtended at each distance to find g' .

To find T'_{int} we note that light which impinges without striking the back reflector has a transmission factor which remains unchanged from the non-reflector case. Thus, once the transmission factor for light which bounces off the back reflector is calculated, these two transmission factors can be appropriately weighted together to give an overall transmission factor.

The approach to finding the transmission factor for light that has bounced off the back reflector is similar to the approach for finding the transmission factor for incident side light. Thus, we take $T_0(\beta)$ (see Equation 2.11), and weight it by the cosine dependence associated with the back reflector. Finally, we average over the

position along the reflector with a weighting to account for the varying intensity, as shown below.

$$T_{refl}(d) = \frac{\int_0^d I(r) \left(\int_{\theta_T}^{\pi/2} \int_{-\pi/2}^{\pi/2} T_n \cos(\theta) \cos^2(\phi) d\alpha d\theta + \int_{\theta_B}^{\pi/2} \int_{-\pi/2}^{\pi/2} T_n \cos(\theta) \cos^2(\phi) d\alpha d\theta \right) dr}{\int_0^d I(r) \left(\int_{\theta_T}^{\pi/2} \int_{-\pi/2}^{\pi/2} \cos(\phi) \cos(\theta) d\alpha d\theta + \int_{\theta_B}^{\pi/2} \int_{-\pi/2}^{\pi/2} \cos(\phi) \cos(\theta) d\alpha d\theta \right) dr} \quad (2.23)$$

Since $g' - g$ is the additional light impingement which results from light which has struck the back reflector, we find:

$$T'_{int}(d) = \frac{g(d)T_{int}(d) + (g'(d) - g(d))T_{refl}(d)}{g'} \quad (2.24)$$

Then the overall T'_{int} is a weighted average with the in-plane angles subtended at each distance. Finally, g' and T'_{int} are used in place of their unprimed counterparts in the multiple scattering model (see Equation 2.9) to find \bar{L}' .

2.4.3 Evaluating Side Absorption with Reflector Scattering

To find \bar{F}' we insert g' and T'_{int} in the multiple scattering model in place of their unprimed counterparts. However, as Equation 2.14 shows, we also need to find T'_1 and g'_1 . To find g'_1 we estimate the impact of the reflector, R , using the following expression:

$$R = (1 - g_1(d)) - (1 - g(d))/2 \quad (2.25)$$

This estimates the amount of light that would be lost, but instead strikes the reflector. Because the top part will always be shadowed last, we assume the losses from the top are constant and equal $(1 - g(d))/2$. Thus, everything else will strike the reflector, and we use our previous result for L_{refl} to find the total losses, $1 - g'_1(d)$.

$$1 - g'_1(d) = R * L_{refl} + (1 - g(d))/2 \quad (2.26)$$

This allows us to modify the transmission factor:

$$T_1'(d) = \frac{T_1(d)g_1(d) + T_{refl}(d)(g_1'(d) - g_1(d))}{g_1'(d)} \quad (2.27)$$

Inserting all the primed quantities for their unprimed counterparts in the equation for \bar{F} and dividing by two to account for the hemispherical illumination gives \bar{F}' . Obviously, the shadowing fraction, u , and the transmission factor prior to any reflection, T_0 , are unchanged by the presence of the reflector since the sun is directly striking the wire.

To find \bar{R}' , we first determine the shadowing of the reflector as a function of wire to wire distance and angle of incidence. From Figure 2.3, the shadowed fraction of the reflector $u(d, \beta)$ is:

$$u(d, \beta) = \frac{d - l \tan(\beta)}{d} \quad (2.28)$$

Taking a weighted average with respect to angle subtended at a given distance gives $u(\beta)$. We average over all β 's, including the differential solid angle and a weighting for intensity, to find u .

$$u = \frac{\int_0^{\pi/2} u(\beta) \sin(\beta) \cos(\beta) d\beta}{\int_0^{\pi/2} \sin(\beta) \cos(\beta) d\beta} \quad (2.29)$$

Next we develop a multiple scattering model. The losses from light that doesn't hit a wire after the initial reflection is L_{inc} , which we find by averaging $L(r)$ over the unshadowed portion of the reflector at each distance, with appropriate weighting for shadowing and the angle subtended at each distance. T_{inc} , the transmission of light after initial reflection, is found in an exactly analogous manner. $(1 - L_{inc})(1 - T_{inc})$ is reflected back into the array after bouncing once off the wire. From the previous result, $(1 - g')/(1 - g'(1 - T'_{int}))$ of this light will be lost. Thus, the total losses for light that initially strikes the reflector are:

$$L_{tot} = L_{inc} + (1 - L_{inc})(1 - T_{inc}) \frac{1 - g'}{1 - g'(1 - T'_{int})} \quad (2.30)$$

Then,

$$\bar{R}' = (1 - L_{tot})u \quad (2.31)$$

To find \bar{R}' , we have approximated the shadowing of the reflector using the closest distance between two wires, leading to an overestimation of the shadowing impact, which should be larger for high filling fractions. This is consistent with our use of the closest distance between two wires for wire to wire shadowing and losses.

2.5 Results for Wire Array Intensity Enhancement with a Lambertian Back Reflector

Inserting the terms derived above into Equation 2.18, we find the light trapping factor, which is plotted as a function of filling fraction in Figure 2.2 by the curves labeled “Lambertian back reflector”. The results closely approach the relevant ergodic limit of $2n^2$ for large filling fractions as the terms involving the wire sides and the reflector become very small. As in the no back reflector case, the light trapping factor falls below the ergodic limit as the filling fraction is decreased from the maximum. It seems likely that, as before, the overestimation of \bar{L} in the radial escape approximation for these filling fractions is at least partially responsible for the decrease. This is supported by the trend in aspect ratios, which is similar to that for the no back reflector case.

Interestingly, we see that for small filling fractions, the light trapping increases asymptotically, significantly exceeding the ergodic limit, in contrast to the no back reflector case. As we previously noted, our approximations improve with decreasing filling fractions. Thus, there is no reason to suspect that surpassing the ergodic limit is an artifact of the modeling assumptions. Furthermore, we can understand the observed asymptotic increase physically by considering the limit of small filling fraction. For very small filling fractions, the side loss factor, \bar{L}' , and the side transmission factor, \bar{F}' , are nearly constant, as they have nearly reached their maxima. In addition, the radius is rapidly approaching zero. Thus, all the terms in Equation 2.18, with the

exception of the back reflector term, are decreasing as the square of the radius. However, the reflector area remains nearly constant with decreasing filling fraction, as the array is already almost entirely reflector. Thus, if \bar{R}' is decreasing less quickly than the radius squared, we should see asymptotic increase. In fact, fitting the asymptotic regions of each of the curves, we find that the curves are increasing as r^{-p} , where p has values between 0.33 and 0.37. Figure 2.4 uses the fit in the calculation of the power to give a sense of the goodness of the fit. The fits are quite good across all the curves, and the values of p do not trend with aspect ratio. These fits suggests that the back reflector transmission goes approximately as the radius to the 5/3 power in the low filling fraction regime, across the range of aspect ratios explored here. The variation of the onset of asymptotic behavior with aspect ratio is also consistent with this explanation, as the denominator of the light trapping factor will decrease more rapidly for shorter wires.

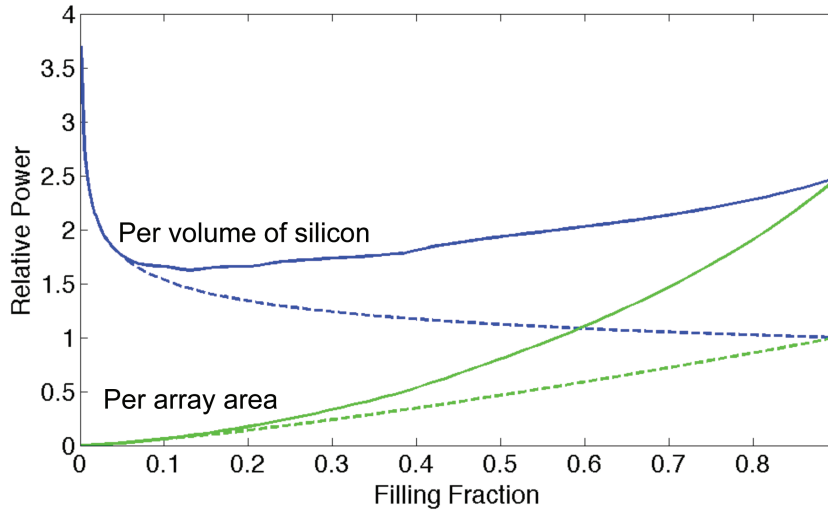


Figure 2.4. The variation of power with filling fraction, for aspect ratio=50. The dotted lines use the asymptotic fits across all filling fractions, so that the goodness of fit can be evaluated. The solid lines use the model results across all filling fractions. Note that while the asymptotic increase produces increased power per volume of silicon, it does not produce increased power per unit area in the array.

To explore this further, we evaluated the relative power, per unit area and per unit

volume of silicon, for an array with an aspect ratio of 50. We assume constant solar cell fill factor² with increasing filling fraction, and assume that the short circuit current is proportional to the volume and the light trapping factor. For an axial junction, the open circuit voltage is proportional to $\ln(J_{sc}/J_0)$, where J_{sc} is the short circuit current density and J_0 is the saturation current. We assume that for a light trapping factor of $2n^2$ the short circuit current density is 30 mA/cm² and the saturation current density is 10^{-12} A/cm². As Figure 2.4 illustrates, while the asymptotic increase does produce an increase in power per unit volume of silicon, as we expect, it does not produce an increase in the power per unit area. This is because the reduced volume of silicon per unit area leads to a reduced short circuit current, which is not overcome by the relatively small increase in open circuit voltage. Thus, in some sense, the Lambertian back reflector is acting as a concentrator, leading to increased power per unit volume of silicon at the cost of power per unit area.

2.6 Comparison of Model with Experimental Data

2.6.1 Including Absorption in Ray Optics Model

Absorption measurements have been reported as a function of angle of incidence and wavelength for VLS-grown microwire arrays [8]. We therefore calculate the absorption for such an array in the ray optics limit. This will give us insight as to the importance of wave optic effects, and will allow us to determine the accuracy of the model for arrays at various scales. We consider an array embedded in PDMS, with a quartz slide underneath it. This very similar to the non-reflector case, except for the fact that we have PDMS/quartz ($n=1.4$) instead of free space. In addition, we include an absorption term in the governing equation. As Yablonovitch has shown, this term should be equal to $2\alpha V I_{int}$, where α is the absorption coefficient, and V is the volume

²This should not be confused with the areal filling fraction of the wire array. As mentioned previously, in solar cells the power can be calculated by multiplying the short circuit current, the open circuit voltage, and the fill factor, where the fill factor accounts for the fact that the current-voltage curve is not square in the power-producing region.

where the absorption is occurring [7].

Thus, the governing equation for a given angle of incidence θ , is:

$$A'_{sides} I_{max} \sin(\theta) F(\theta) + 2A_{end} I_{max} \cos(\theta) T(\theta) = 2\alpha V I_{int} + \frac{2A_{end} \bar{T}_{end} I_{int}}{n^2} + \frac{A_{sides} \bar{L} I_{int}}{n^2} \quad (2.32)$$

where I_{max} is the intensity of the incident light at normal incidence, and the factors of $\sin(\theta)$ and $\cos(\theta)$, account for the decreased intensity at non-normal incidence. Note that for the light entering through the sides we have A'_{sides} instead a A_{sides} , to denote that we need to account for decreased intensity as the wire turns away from the in-plane direction from which the light enters. Rearranging to find I_{int} gives:

$$I_{int} = \frac{A'_{sides} I_{max} \sin(\theta) F(\theta) + 2A_{end} I_{max} \cos(\theta) T(\theta)}{2\alpha V + \frac{2A_{end} \bar{T}_{end}}{n^2} + \frac{A_{sides} \bar{L}}{n^2}} \quad (2.33)$$

The fraction of light absorbed, A , is:

$$A = \frac{2\alpha V I_{int}}{A_{tot} I_{max} \cos(\theta)} = \frac{2\alpha V (A'_{sides} F(\theta) \tan(\theta) + 2A_{end} T(\theta))}{A_{tot} (2\alpha V + \frac{2A_{end} \bar{T}_{end}}{n^2} + \frac{A_{sides} \bar{L}}{n^2})} \quad (2.34)$$

where A_{tot} is the total area of one unit cell. With the exception of A'_{sides} , these terms follow directly from our previous work. However, between various in plane angles, the amount of shadowing will vary. Previously, to find \bar{F} we averaged this over all the in-plane angles. Experimentally, though, the light will only come from one in-plane direction, which in this case was aligned in the direction of maximal shadowing. In addition, to account for a non-free space medium, all the factors of $1/n^2$ are replaced with n_1^2/n_2^2 , where n_1 is the index of the embedding medium and n_2 is the index of the wires, due to the relative density of modes between the two media.

2.6.2 Experimental Methods

To find the experimental absorption data, arrays of silicon microwires were grown by the VLS mechanism from SiCl_4 precursors as reported previously [27]. The geometry of the arrays was defined by the photolithographic mask used to pattern the VLS

catalyst islands. Wires with a radius of $1\mu\text{m}$ were grown from a hexagonally packed mask with $3\mu\text{m}$ diameter holes with a center to center spacing of $9\mu\text{m}$. Larger wires with a radius of approximately $4\mu\text{m}$ were grown from a hexagonally packed mask with $15\mu\text{m}$ diameter holes and $30\mu\text{m}$ center to center spacing.

After growth, the metal VLS catalyst was removed from the wires and the height and diameter of the wires were measured using scanning electron microscopy. The wires were embedded in polydimethylsiloxane (PDMS, Sylgard) as reported previously [27]. The PDMS was dropcast onto the wires and spun at 3000 rpm, and then cured at $120\text{ }^\circ\text{C}$ for 30 minutes. Wires were removed from the substrate by scraping the PDMS film with a razor blade. Integrated reflection and transmission measurements were performed with a custom-built 4 inch integrating sphere apparatus using a Fianium supercontinuum laser illumination source and a 0.25 m monochromator [8]. The absorption of each sample was determined from the wavelength and angle resolved transmission and reflection measurements [13].

We then input structural parameters, as determined by SEM, from these measured arrays into the model developed above. The PDMS embedding material was included in the model, but the PDMS/air interface was neglected. (The PDMS/air interface gives about 3% reflection.) For each angle of incidence and wavelength we found the various absorption and loss terms, using wavelength specific n and α data. For wires with an approximately $1\mu\text{m}$ radius, results are given in Figure 2.5a and b. We also compare to wires with a radius of approximately $4\mu\text{m}$ and a similar aspect ratio, which should be closer to the ray optics limit. The results are shown in 2.5c and d.

2.6.3 Comparison of Model and Experiment: The Importance of Wave Optical Effects

We found that the results for the larger wires are much more similar to the experimental data, though there is still significant disagreement. This suggests that there are significant wave optics effects in the $1\mu\text{m}$ radius case, which become less significant for the $4\mu\text{m}$ array. For example, if we examine the maximal absorption at near normal

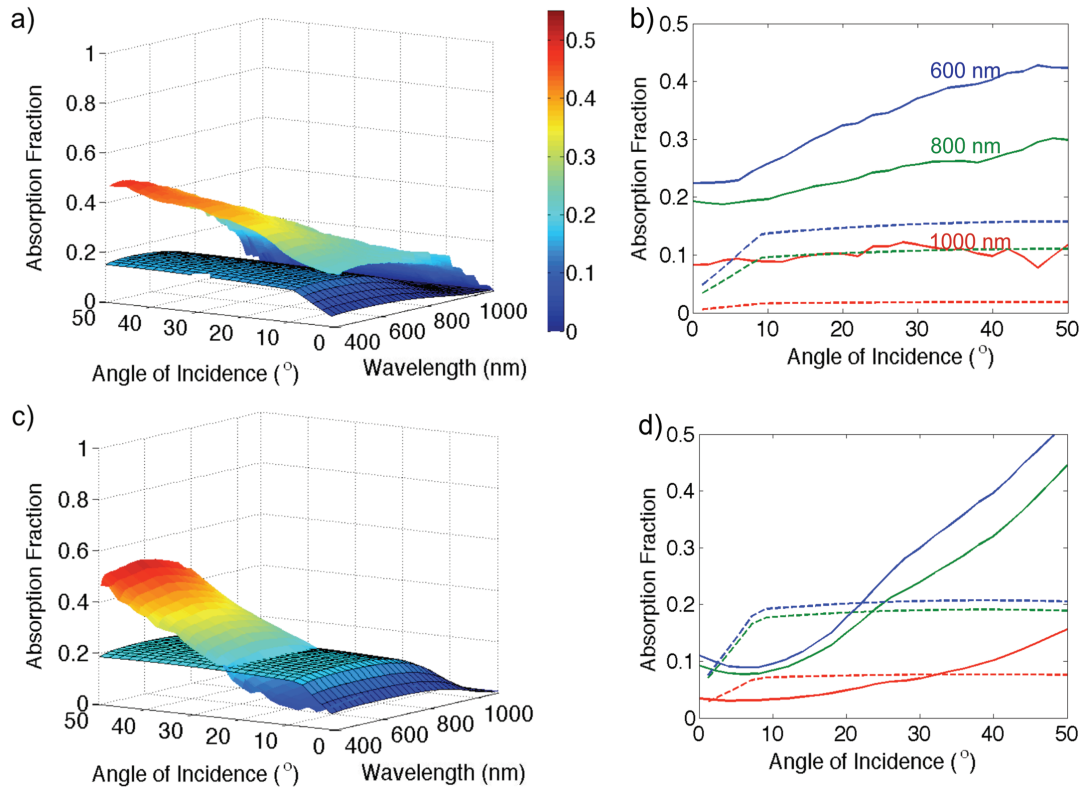


Figure 2.5. a) The outlined surface gives the model output for wires with a 4.9% filling fraction, a $1 \mu\text{m}$ radius, and a height of $44 \mu\text{m}$. The upper surface is the experimental result for such an array. b) The solid lines show the experimental data for various wavelengths, and the dotted lines show the model output. Note that even for the low absorbing 1000 nm curves, the model significantly underpredicts the absorption. c) The outlined surface gives the model output for wires with a 7.3% filling fraction, a $4 \mu\text{m}$ radius, and a height of $160 \mu\text{m}$. The other surface is the experimental result for such an array. d) As before, the solid lines show the experimental data and the dotted lines show the model output. Note the reasonable agreement, especially at 1000 nm.

incidence, we see that the model produces values similar to the filling fractions, and the $4\mu\text{m}$ array gives a value fairly close to the filling fraction, with 11% absorption for a 7% filling fraction. However, for the $1\mu\text{m}$ array we see 23% absorption for a 5% filling fraction, suggesting a significant wave optic effect in this regime. In fact, it is well known that particles on the order of the wavelength of light can have scattering and absorption cross sections considerably larger than their physical size, whereas in ray optics the cross section corresponds to the physical size [28]. It seems likely that this effect is causing the enhanced absorption observed in the smaller wires.

Despite the reasonable agreement for angles of incidence relatively near normal, the ray optics model fails to capture the strong increase in absorption observed with large angles of incidence for wavelengths where the absorption is strong. However, our model assumes that the light is fully randomized before any significant absorption takes place, which will not occur in strongly absorbing wavelength regimes. Thus, it is not surprising that our model fails to explain this behavior. As we expect, the agreement is improved for wavelengths where the absorption is low and this randomization condition is more accurate, as is shown in Figure 2.5d. However, even in this case, the shape of the curve is not captured particularly accurately, most likely due to differences between the experimental and modeled wires. For example, if the experimental wire surfaces were not perfectly Lambertian, but somewhat specular, the angular profile would likely be sloped across a wider range of angles, as is seen here. This is because the light which strikes the wire sides would reflect in one direction rather than be scattered in all directions, so light at near normal incidence would be less likely to enter the sides than for specular wires. Thus, our model works reasonably well in the low absorbing ray optics regime, but does not quite capture the angular dependence, perhaps due to non-Lambertian experimental wire surfaces.

2.7 Conclusions

The model developed in this paper addresses wire geometries from a ray optics perspective, assuming Lambertian surfaces and weak absorption. In the non-reflector

case, the model produces light trapping close to the ergodic limit of n^2 for filling fractions approaching zero and approaching unity. This conforms with our thermodynamic expectation and allows us to understand the accuracy of the approximations used for computational feasibility. In addition, it confirms our physical expectations about the regimes for which the approximations will be most accurate.

Applying the model to the case of a Lambertian back reflector, we observe significant intensity enhancements, including asymptotic increases for small filling fractions that significantly exceed the ergodic limit of $2n^2$. Quantitatively, for a filling fraction of 0.1%, the enhancement can exceed $3n^2$, and the asymptotic increase goes approximately as $r^{-1/3}$, where r is the wire radius. These asymptotic increases result from the reflector acting as a concentrator. Fitting these results gives insight into the asymptotic behavior of the transmission factor for light that initially strikes the reflector, which goes as approximately $r^{5/3}$. It seems that a more sophisticated back reflector, which preferentially scattered light sideways, could allow for asymptotic behavior which would be even more dramatic, a topic that deserves further study. However, while the asymptotic increases found here do give increased power per volume of silicon, there is reduced power per unit wire array area, owing to reduced silicon volume at low filling fractions.

Finally, in comparing the model with experimental absorption data, there is agreement with experiment for large ($4 \mu\text{m}$ radius) wires in the low absorbing regime where the model is valid. The results suggest that the very strong absorption observed in smaller wires ($1 \mu\text{m}$ radius) may be significantly due to wave optical effects, and analysis using a wave optics formalism is required in order to understand this strong absorption. Thus, even though previous modeling has suggested that large wires could be superior from a device physics perspective, they appear to be less optimal from a light trapping perspective. This trade-off deserves further study, as do the wave optics effects observed in smaller wires.

Chapter 3

Modeling the Effects of Angle Restriction

3.1 Angle Restriction and Photon Entropy

Under direct sunlight, conventional solar cells emit light isotropically, while receiving light only from the angles spanned by the solar disk, as shown in Figure 3.1. This increase in the angular distribution of light corresponds to an increase in the photon entropy, and the inherent entropy increase reduces the solar cell efficiency [29-32]. Thus, efficiency may be increased by reducing the angular spread of emitted light

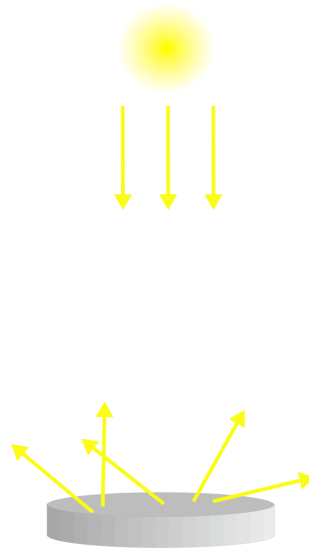


Figure 3.1. In a conventional solar cell under direct sunlight, light is received from a narrow angular range but emitted from the cell into a wide angular range, resulting in a photon entropy increase and associated efficiency reduction. Here, the sun is illustrated at normal incidence to the solar cell, as we assume a tracking system.

from the solar power conversion system.

Figure 3.2 illustrates two possible approaches to reducing the photon entropy increase. Most commonly, concentrating solar systems partially exploit this angular photon entropy term by redirecting the solar cell light emission into a narrow angular range, as shown in Figure 3.2a. As is well known from deployed systems and experimental measurements of solar cells under concentration, this leads to efficiency increases at low to moderate concentration ratios, due to increases in the solar cell voltage. While higher concentration ratios further reduce the angular spread of emitted light and resulting photon entropy increase, they do not practically realize the further efficiency gains that would be expected. At high concentration and the resulting high current densities, increased series resistance and heating degrade the cell efficiency, so that maximum efficiencies are achieved around a few hundred suns for typical high concentration cells, rather than the approximately 46,000 suns possible at maximum solar concentration [33-35].

While concentration has been employed with significant success, the heating and series resistance losses mentioned earlier limit the possible benefits of photon entropy management. With angle restriction, as shown in Figure 3.2b, an optic is placed above the cell that allows light to enter or leave the cell only near normal incidence. Thus, light that would otherwise be emitted at oblique angles is reflected back into the cell, a process known as photon recycling [32]. Since cells with angle restriction operate with current densities similar to traditional flat plate cells, heating and series resistance do not contribute additional losses, and efficiencies above 40% are predicted in ideal systems [31, 32]. However, while concentration has been implemented in commercial systems, until recently it was thought that the benefits of angle restriction and photon recycling would not be observable in experimental solar cells, owing to non-radiative recombination [32].



Figure 3.2. a) A concentrator system takes the light emitted from all angles in a solar cell and reflects it to within a narrow range of angles. As concentration ratio increases, the emission angle from the concentrator is reduced, so to fully reduce the angle of emission, maximum concentration is required. b) We propose a design for a thin coupler which limits the emission angle without concentrating. This avoids the deleterious heating and series resistance effects observed in high concentration solar systems. Key to achieving the highest possible efficiencies with design are the thin cell and the highly reflective, light trapping back reflector shown in the schematic.

3.2 Enhanced Light Trapping and Photon Recycling

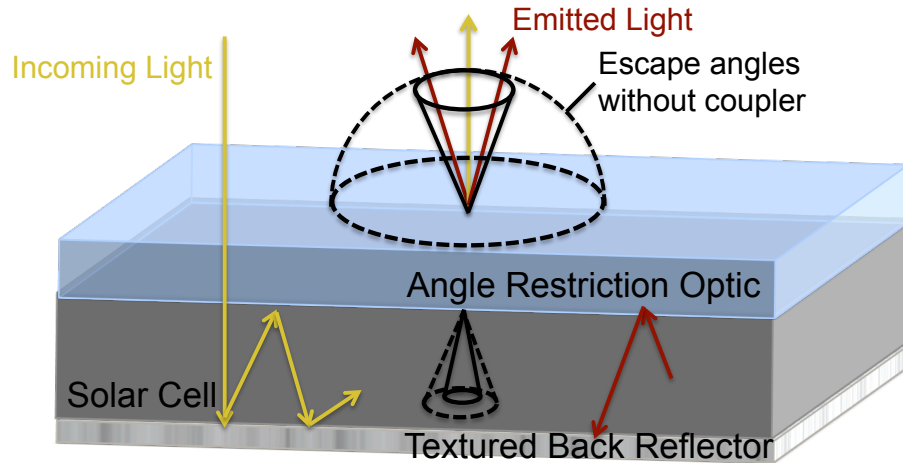


Figure 3.3. With angle restriction, the escape cone within the cell is narrowed. The dotted lines illustrate the escape cone and corresponding range of emitted angles without angle restriction, and the solid lines indicate the escape cone and emitted angles under angle restriction. The narrowed escape cone leads to enhanced light trapping of incoming light (left), as well as enhanced photon recycling of emitted light (right).

In a more mechanistic picture, the benefits to angle restriction are due to a narrowed escape cone. As shown in Figure 3.3, total internal reflection in a non-angle restricted cell leads to an escape cone of 16° . With angle restriction, this escape cone and the angular range of emission are both narrowed. This leads to enhancements in both light trapping and photon recycling as it is more difficult for both emitted and scattered light to escape. Enhanced light trapping occurs only in a cell with a randomizing surface. (Such cells will be referred to as “light trapping” cells, while cells without a randomizing surface will be referred to as “planar”.) Incoming light is scattered by the randomizing surface, and the narrower escape cone leads to an enhanced path length inside the the cell. This modifies our previous expression

(Equation 1.6) for the absorptivity in a light trapping cell:

$$a(E) = \frac{\alpha(E)}{\alpha(E) + \frac{\sin^2(\theta)}{4n^2W}} \quad (3.1)$$

where θ is the emission angle of the solar cell [7, 30, 36]. Note that this expression reproduces Equation 1.6 where there is no angle restriction ($\theta = 90^\circ$). Most importantly, angle restriction allows for full light absorption in a thinner cell.

Enhanced photon recycling occurs because radiatively emitted photons that would otherwise leave the cell are reflected back by the narrowed escape cone. Thus, radiatively emitted photons are more likely to be re-absorbed and losses from radiative recombination are reduced, leading to an increase in voltage. Note that enhanced photon recycling can occur in either a light trapping or planar geometry, as radiative emission occurs in all directions, randomizing the emitted light. However, the benefits of enhanced photon recycling will only be significant for materials where radiative recombination and emission is a major loss mechanism, like GaAs or other III-V materials. In silicon, where non-radiative processes like Auger recombination limit the voltage, enhanced photon recycling has little effect on efficiency. Instead, as enhanced light trapping allows for full absorption in a thinner cell, losses from bulk non-radiative processes are reduced, with a resulting increase in voltage and efficiency.

3.3 Detailed Balance Models

3.3.1 Cells in the Radiative Limit

To model the effects of angle restriction, we implement a detailed balance model, originally developed by Shockley and Queisser [29]. In modeling angle restriction with GaAs, detailed balance allows us to account for photon recycling effects, which are not routinely included in device physics solar cell models. As in previous work, we initially assume that all recombination is radiative, known as the radiative limit [29, 32, 36]. While this may seem unrealistic in a real cell, experimental GaAs cells have recently come within a few percentage points of the detailed balance efficiency, and have

also achieved high external radiative efficiency¹ (ERE) values, indicating that they are approaching the radiative limit [37, 39]. Detailed balance also assumes that each photon absorbed above the bandgap produces a single electron hole pair, which immediately thermalizes to the solar cell bandgap [29]. Because of the thermalization energy loss, the model balances photon number flux, rather than energy flux.

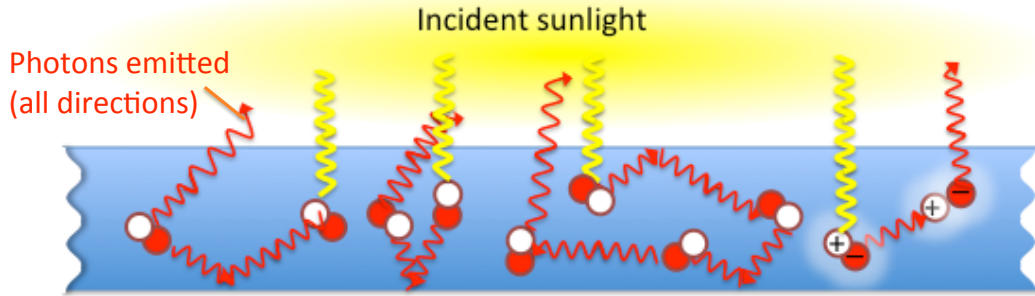


Figure 3.4. In a detailed balance model the photon flux from the sun (yellow) must equal the emitted photon flux (red) from the cell at open circuit. The population of excess carriers (electron-hole pairs) builds up within the cell until these two photon fluxes balance, defining the open circuit voltage. Figure courtesy of Carrie Hofmann.

As shown in Figure 3.4, we consider a cell in the radiative limit, so at open circuit the only route for carrier loss from the cell is via a radiatively emitted photon [29, 32, 36]. As the sun shines on the cell, the excess carrier concentration inside the cell increases, increasing the rate of radiatively emitted photon loss until steady state is reached and the photon fluxes balance. In steady state the carriers created from the solar photons absorbed by the cell must equal the carriers lost via radiatively

¹External radiative efficiency (ERE) is the probability that a recombination event results in a photon emitted from the cell. Internal radiative efficiency (IRE), refers to the probability of a recombination event resulting in a photon emitted within the cell. In high quality GaAs, IRE values greater than 90% are expected. However, owing to strong total internal reflection and re-absorption of internally emitted photons, recent world-record cells have ERE values in the 22.5-48% range [37, 38]. In the radiative limit, both IRE and ERE are 100%.

emitted photons leaving the cell:

$$\int_{E_g}^{\infty} S(E)a(E)dE = \int_{\Omega_c} \int_{E_g}^{\infty} a(E) \frac{2}{h^3 c^2} \frac{E^2}{e^{(E-qV_{oc})/kT} - 1} dE \cos(\theta) d\Omega \quad (3.2)$$

where $a(E)$ is the fraction of photons at energy, E , absorbed by the solar cell, Ω_c is the solid angle the cell emits into, $S(E)$ is the solar spectrum, and qV_{oc} equals the chemical potential of the cell due to excess carrier concentration [32]. The left side is the flux of solar photons absorbed by the cell, and the right side is the flux of radiatively emitted photons leaving the cell, as given by Planck's law with increased emission owing to the chemical potential, or voltage, of the cell. To find the net current at conditions other than open circuit, V_{oc} is replaced by an input voltage, and the radiatively emitted flux from the cell is subtracted from the solar flux to find the net current. Tracing out the current-voltage relationship in this way, we find the maximum power point and the cell efficiency, as well as J_{sc} and V_{oc} if desired. As in the original work, this assumes that carriers are collected without loss [29]. This assumption is quite accurate for GaAs, silicon, and most other well-developed inorganic solar cell materials, as solving the charge transport problem is necessary to achieving reasonable efficiencies.

Assuming that the V_{oc} does not closely approach the bandgap, we may approximate the V_{oc} from Equation 3.2 as

$$V_{oc} \approx kT \ln \left(\frac{\int_{E_g}^{\infty} S(E)a(E)dE}{\int_{\Omega_c} \int_{E_g}^{\infty} a(E) \frac{2}{h^3 c^2} \frac{E^2}{e^{(E-qV_{oc})/kT} - 1} dE \cos(\theta) d\Omega} \right) = kT \ln(J_{sc}/J_0) \quad (3.3)$$

where J_{sc} is the short-circuit current and J_0 is the dark current, which is solely due to radiatively emitted light under these assumptions. Thus, reducing Ω_c with angle restriction reduces J_0 and increases V_{oc} . Similarly, increasing J_{sc} by operating the cell under concentrated sunlight also leads to increased V_{oc} . In fact, the V_{oc} increase for an ideal cell from maximum concentration is the same as from angle restriction to the solar disk, as we expect from photon entropy arguments.

3.3.2 Accounting for Non-Radiative Losses

While the original detailed balance formulation includes only radiative emission, to model more realistic cells, non-radiative recombination and absorption in non-ideal back reflectors must be included. In the low injection limit, for n-type material, we include these losses as:

$$\int_{E_g}^{\infty} S(E)a(E)dE = \int_{E_g}^{\infty} \left[\int_{\Omega_c} a(E) \cos(\theta) d\Omega + \pi n_r^2 a'(E) \right] \frac{2q}{h^3 c^2} \frac{E^2}{e^{(E-qV)/kT} - 1} dE + qW(C_n n^2 p + C_p p^2 n) + 2qSp + Wqp/\tau_{SRH} \quad (3.4)$$

As before, the right hand side of the equation gives all the sources of loss from the cell. The first term includes radiative light emitted from the cell or absorbed in the back reflector, where $a(E)$ is the angle-averaged emissivity of the cell, and $a'(E)$ is the angle averaged absorption in the back reflector. n_r is the index of refraction in GaAs, and is included because light only needs to be emitted into the cell, rather than air, to be absorbed in the back reflector [32, 40]. The next terms account for Auger recombination and surface recombination where C_n and C_p are the Auger coefficients [41], W is the cell thickness, and S is the surface recombination velocity. The surface recombination term is multiplied by two, to account for both the front and back surfaces of the cell, where S is an average over the two surfaces. The final term accounts for bulk recombination due to Shockley-Read-Hall recombination in trap states, where τ_{SRH} is the lifetime associated with this recombination mechanism [42]. As with Auger recombination, this term is also multiplied by the cell thickness as both are bulk recombination mechanisms. n and p , the electron and hole concentrations, are assumed to be constant across the cell and are determined from the assumed base doping, the neutrality condition, the cell voltage, and the law of mass action [43, 44].

While low injection is a reasonable assumption for GaAs, silicon cells often have lower base doping than GaAs, and often operate at or near the high injection limit. To account for this, we use the full expressions for surface and Shockley-Read-Hall recombination, as will be discussed in detail in Chapter 6 [42]. In addition, band gap

narrowing, free carrier absorption, and a more sophisticated Auger parameterization are included in the silicon model. These will also be discussed in more detail in Chapter 6.

3.4 Absorptivity in Light Trapping and Planar Cells

3.4.1 Accounting for Modal Structure

While Equation 3.1 works well for solar cells in the ray optic limit, such as silicon cells, thin GaAs cells are not in this limit, and the optical modes of the cell must be accounted for in calculating $a(E)$. To accurately model thin cells, we follow the approach taken by Stuart and Hall [45]. This approach is similar to the ergodic limit derived in the introduction, but the guided modes and their group velocities are accounted for. First, the modal structure of the solar cell is calculated, neglecting the absorption within the cell. We assume that all radiating and guided optical modes of the cell are equally occupied by a randomizing, scattering mechanism, such as a textured back reflector or cladding layer. This scattering mechanism is unspecified, and we therefore neglect it in calculating the modal structure. The modal occupancy is calculated as a function of the light intensity entering the cell from the bulk ray optical modes outside the cell, just as in the ergodic limit [45]. To account for the limited emission angle, we reduce the density of these in- and out-coupling bulk modes, denoted as ρ_0 by a factor of $\sin^2(\theta)$, where θ is the emission angle.

Propagating this modification through Stuart and Hall's analysis, we arrive at the following expression:

$$a(E) = \frac{\rho_{rad}}{\rho_{tot}} \frac{\alpha}{\alpha + \frac{\sin^2(\theta)\rho_0 v_g^0}{4W\rho_{tot}v_g^{rad}}} + \sum_m \frac{\rho_m}{W\rho_{tot}} \frac{\Gamma_m \alpha}{\Gamma_m \alpha + \frac{\sin^2(\theta)\rho_0 v_g^0}{4W\rho_{tot}v_g^m}} \quad (3.5)$$

where ρ gives the optical mode density, v_g is the group velocity, α the absorption coefficient at the relevant energy, and Γ the confinement factor for the trapped modes. Quantities related to the trapped modes are indexed by m , the radiating

modes are labelled by *rad*, and the in- and out-coupling modes by 0. This expression can be understood intuitively as a weighted average of the fraction of light absorbed in the trapped and radiating modes of the cell. The weighting factors give the modal density of a given optical mode as a fraction of the total modal density of the cell, and the absorption factors are the ratio of the modal absorption rate to the total modal loss rate due to absorption and light out-coupling. With angle restriction, the number of in- and out-coupling modes is reduced with decreasing angle of emission, thus increasing the absorption factors. This result reduces to the ray optical result (Equation 3.1) under limited emission angle for a thick cell, and recovers the original Stuart and Hall result for a thin cell without limited emission angle [30, 45].

3.4.2 Absorption in a Light Trapping Cell with Non-Ideal Back Reflector

To find the parasitic absorption in a light trapping cell, we include the parasitic absorption in all non-guided optical modes of the cell as an absorption coefficient:

$$\alpha' = \frac{1 - \bar{R}}{4W} \quad (3.6)$$

where α' is the parasitic absorption length owing to non-unity reflectivity at the back surface and \bar{R} is the angle averaged back surface reflectivity [46]. The factor of four results from path length enhancements for light traveling at all angles, as in the ergodic limit, as well as the dual pass through the cell associated with each reflection at the back reflector. This can be easily incorporated into Equation 3.1 as an additional loss mechanism:

$$a(E) = \frac{\alpha(E)}{\alpha(E) + \alpha'(E) + \frac{\sin^2(\theta)}{4n^2W}} \quad (3.7)$$

Thus, along with losses due to useful absorption and light escape, parasitic absorption is an additional loss mechanism. Note that this parasitic loss reduces the useful absorption of light in the solar cell, $a(E)$. To include free carrier absorption, as in

silicon, we simply add it as an additional parasitic loss:

$$\alpha'(E) = \frac{1 - \bar{R}}{4W} + \alpha_{FCA} \quad (3.8)$$

where α_{FCA} is the absorption coefficient for free carrier absorption.

For the cells with modal structure, the absorption rate for the non-guided or radiating modes is increased by the absorption in the back reflector. (We neglect free carrier absorption in all GaAs cells, which are the only cells where we are concerned with the modal structure.) We assume the guided modes do not suffer back reflector absorption, as they are confined to the semiconductor core by thick cladding layers. Thus, in analogy to the semiconductor absorption:

$$r_{abs}^{rad} = \alpha' L_{rad} A W \Omega_{rad} \quad (3.9)$$

where r_{abs}^{rad} is the parasitic absorption rate in the radiating modes, L_{rad} is the radiance in the radiative modes, and Ω_{rad} is the solid angle occupied by radiating modes. Note that with limited emission angle, all the radiating modes as defined by Stuart and Hall may not actually radiate, owing to the reduced escape cone. However, these modes have the same group velocity and absorption properties as under non-angle limited conditions. Since the calculation only considers these properties of the modes, they continue to be classified as radiating modes. In addition, all radiating modes, as originally defined, will suffer parasitic loss from the back reflector, as they are not confined to the semiconductor.

Propagating this modification through Stuart and Hall's analysis, we find that the absorption in the semiconductor is:

$$a(E) = \frac{\rho_{rad}}{\rho_{tot}} \frac{\alpha}{\alpha + \alpha' + \frac{\sin^2(\theta)\rho_0 v_g^0}{4W\rho_{tot} v_g^{rad}}} + \sum_m \frac{\rho_m}{W\rho_{tot}} \frac{\Gamma_m \alpha}{\Gamma_m \alpha + \frac{\sin^2(\theta)\rho_0 v_g^0}{4W\rho_{tot} v_g^m}} \quad (3.10)$$

Intuitively this makes sense as the parasitic absorption in the back reflector represents another loss channel for each radiating mode, and should therefore reduce the absorption factor for these modes. Furthermore, as the reflectivity of the back surface

decreases, the amount of light absorbed in the semiconductor is reduced, reducing the short circuit current. Note that for both the ray optical and modal structure case, the reduction in short circuit current is somewhat overestimated, as we have assumed that all the modes are equally occupied before any substantial absorption occurs. If the randomization occurs at the back surface only, most of the light in the blue portion of the spectrum will have been absorbed before it is randomized.

3.4.3 Parasitic Absorption of Emitted Light in a Light Trapping Cell

In addition to the reduction in short circuit current with a non-ideal back reflector, as shown above, there is a decrease in photon recycling due to parasitic absorption of radiatively emitted light in the back reflector. Thus, as in Equation 3.4, we must find an expression for $\alpha'(E)$. To do this, we use a reciprocity approach developed by Martì, where the parasitic loss of emitted light at the back surface is determined by finding the fraction of light coming through the back surface that is ultimately absorbed in the cell [32, 40]. While the expression originally developed with this approach refers to a fully absorbing back reflector and a planar cell, it can be modified to account for a partially reflective back surface. We treat all parasitic loss as an angle averaged back surface reflectivity R_b defined as:

$$R_b = 1 - 4W\alpha' \quad (3.11)$$

Then, $1 - R_b$ of the light can enter “through” the back reflector, and we assume that it is immediately scattered in a light trapping cell. The absorption of the scattered light then gives the parasitic absorption of emitted light. For cells in the ray optics limit:

$$a'(E) = (1 - R_b) \frac{\alpha(E)}{\alpha(E) + \alpha'(E) + \frac{\sin^2(\theta)}{4n^2W}} \quad (3.12)$$

For cells with modal structure, the scattering also occupies guided modes:

$$a'(E) = (1 - R_b) \left[\frac{\rho_{rad}}{\rho_{tot}} \frac{\alpha}{\alpha + \alpha' + \frac{\sin^2(\theta)\rho_0 v_g^0}{4W\rho_{tot}v_g^{rad}}} + \sum_m \frac{\rho_m}{W\rho_{tot}} \frac{\Gamma_m \alpha}{\Gamma_m \alpha + \frac{\sin^2(\theta)\rho_0 v_g^0}{4W\rho_{tot}v_g^m}} \right] \quad (3.13)$$

Note that in these expressions, the parasitic losses increase as the back reflectivity decreases. In addition, parasitic loss of emitted light occurs only at wavelengths where there is band to band absorption, as we expect.

3.4.4 Absorption in a Planar Cell

For the planar case, while the governing equation is unchanged, the absorptivities are modified based on the geometry. In addition, the absorptivity now depends on the angle of incidence, as the light is not randomized. The absorptivity in GaAs is now due to double pass absorption:

$$a(E, \theta) = 1 - e^{\frac{-\alpha W}{\cos(\theta)}} + e^{\frac{-\alpha W}{\cos(\theta)}} \bar{R} (1 - e^{\frac{-\alpha W}{\cos(\theta)}}) \quad (3.14)$$

where θ is the angle of the light in GaAs. We assume that incoming light enters at normal incidence, and that the absorptivity for emitted light is averaged within the emission angle. Owing to the high index of refraction inside the cell, the effect of incidence angle on absorption is small. We note that neglecting the modal structure of the cell in this case is reasonable, as there is no mechanism for light in the trapped modes to access free space, and thus they do not contribute to the absorptivity.

Similarly, for parasitic absorption, the modal structure may be neglected. While radiative emission into guided modes will occur, we assume light in the guided modes will not experience parasitic absorption in the back reflector, as it will be confined by the cladding layers. Thus, we utilize a ray optical approach to calculate parasitic absorption of emitted light in these cells. As there is no scattering, for $a'(E)$ we consider separately light within the escape cone, and light that lies outside this escape cone. We again extend Martí's approach and imagine light entering "through" the back reflector and then passing through the cell many times, being absorbed in both

the cell and back reflector [32, 40]. The fraction of light absorbed in the back reflector is then expressed as:

$$a'(E, \theta) = \frac{(1 - R_b)(1 - e^{-2\alpha W / \cos \theta})}{1 - R_b e^{-2\alpha W / \cos \theta}} \quad (3.15)$$

where R_b is the reflectivity of the back reflector, α is the absorption coefficient of GaAs, and θ is the angle in GaAs. For light inside the escape cone, we use the same approach, but consider the reflectivity, R_c , and transmissivity, T_c , of the cell surface to find the back reflector absorption:

$$a'(E, \theta) = \frac{(1 - R_b)(1 - T_c e^{-\alpha W / \cos \theta} - R_c e^{-2\alpha W / \cos \theta})}{1 - R_b R_c e^{-2\alpha W / \cos \theta}} \quad (3.16)$$

Finally, to calculate $a'(E)$ we evaluate $a'(E, \theta)$ for all angles, and take an angle average at each energy. For our previous expressions we neglected reflections at the cell surface, as anti-reflective coatings are quite advanced. However, many of the experimental cells do not have anti-reflective coatings, so reflection at the cell surface is more significant, and is included for the analysis of these cells, as in Chapter 5. We also include realistic anti-reflective performance at the cell-glass interface in Section 4.8. For all other calculations in Chapter 4, we assume $T_c = 1$, as with an ideal anti-reflective coating. We note that similar expressions have been derived by other authors for a perfectly absorbing back reflector, and that these expressions are a straightforward extension of the same approach. Furthermore, these results reduce to the previously derived results [32, 40].

Chapter 4

Angle Restriction in GaAs Solar Cells

4.1 Motivation

In this chapter, we consider the effects of limiting the solar cell emission angle in GaAs solar cells. By limiting the solar cell emission angle, as discussed in the previous chapter, photons emitted by radiative recombination are less likely to escape from a solar cell, reducing dark current and increasing efficiency. This photon recycling effect is inherent in Shockley and Queisser's original detailed balance analysis, but the limited emission angle case was not considered explicitly [29]. While it has been calculated that limiting emission angle could yield efficiencies exceeding 40%, more recent work analyzing this effect in a planar GaAs cell concluded that no advantage would exist for a realistic material owing to non-radiative recombination [32]. In contrast, we find that utilizing a light-trapping-rather than planar-cell geometry mitigates losses from non-radiative recombination, so significant benefits are possible with angle restriction. In fact, using the detailed balance model introduced in the last chapter, we demonstrate that efficiencies exceeding 38% are potentially achievable with limited emission angle and an ideal back reflector.

As discussed in the previous chapter, for cells with a light-trapping structure, limiting the solar cell emission angle reduces the optical escape cone and enhances the light trapping effect [7, 36]. Previously, efficiency benefits under angular restriction have been considered with silicon in a light-trapping geometry [30]. However, photon recycling benefits are minimal due to low radiative efficiency in silicon, and were not included in the model. Here we consider a light trapping GaAs cell, where photon recycling is much more prominent owing to high radiative efficiency in GaAs. Thus

while previous work has considered either light trapping or photon recycling, the thin, light trapping GaAs solar cells considered here maximize both of these effects, and we find a new regime of higher efficiencies that were not previously considered achievable for a single junction solar cell under one sun illumination [30, 32, 47]. We also illustrate that a light trapping geometry allows for thinner cells with higher efficiencies, significantly increasing the feasibility of the scheme.

While an angle restriction system, like a concentrator system, will require solar tracking, the one-sun nature of the angle restricting system avoids the deleterious heating and series resistance effects associated with high concentrations that were mentioned in the previous chapter [33-35]. Furthermore, the light trapping nature of the cells allows for cells that are 1/60th the thickness of current technology with full light absorption. Assuming that junctions and window layers can be fabricated with high quality in such a thin layer, this allows some of the materials savings associated with concentrating systems to be realized in a flat plate geometry, without the high aspect ratio optics found in traditional high concentration systems. We thus envision a flat plate tracking system with thin, light trapping GaAs cells operating efficiencies significantly higher than those achievable today.

4.2 Angle Restriction in a Light Trapping GaAs Cell: Limits to Efficiency

4.2.1 Cell in the Radiative Limit

Using the expression for the absorptivity found in the previous chapter, along with the air mass 1.5 direct solar spectrum (AM 1.5 D)¹ and the optical constants of GaAs, detailed balance efficiencies were calculated for various GaAs cell thicknesses,

¹This is the standard solar spectrum for terrestrial applications. In these calculations we utilize the direct, rather than global, solar spectrum, which includes only light coming directly from the sun. Scattered, diffuse solar illumination from clouds or air particulates are included in the global spectrum. However, limiting the emission angle will reduce the absorption of this diffuse light, and therefore we consider only the direct portion of the solar spectrum.

assuming silicon nitride on both sides of the cell in the modal calculation. As shown in Figure 4.1a, As the angle of emission narrows, both light trapping and photon recycling are enhanced. With narrow angle restriction, to about 7° , cell performance is independent of cell thickness, as increased light trapping allows all the light to be absorbed within even a 50 nm thick cell, or approximately 1/60th of the material in a conventional non-angle restricted cell.

The angular accuracy of a tracker is usually expressed as a concentration, with higher concentrations corresponding to improved angular accuracy. As the angular accuracy of the tracker must be smaller than the emission angle, concentration factors which correspond to a given emission angle are marked in Figure 4.1a to illustrate the tracking accuracy required. As 1000x trackers are currently commercially available, with higher accuracies demonstrated in research systems, we see that very high single junction efficiencies are possible using existing two-axis solar tracking technology [48, 49].

4.2.2 Effect of Auger Recombination

While the results in Figure 4.1a are encouraging, they assume all recombination is radiative, which is unrealistic in a real material. Since GaAs can be fabricated with very high purity and excellent surface passivation via III-V capping layers, for now we consider only Auger recombination as it is the sole intrinsic, unavoidable source of non-radiative recombination [41, 46, 50-52]. As in the previous chapter, we include Auger recombination in the detailed balance equation as:

$$\int_0^\infty S(E)a(E)dE = \int_{\Omega_c} \int_0^\infty a(E) \frac{2}{h^3 c^2} \frac{E^2}{e^{(E-qV_{oc})/kT} - 1} dE \cos(\theta) d\Omega + CWn_i^3 e^{3qV_{oc}/2kT} \quad (4.1)$$

where C is the Auger coefficient of $7 \times 10^{-30} \text{cm}^6 \text{s}^{-1}$, and n_i is the intrinsic carrier concentration in GaAs [40, 41, 47]. In contrast to the expression in the previous chapter, this expression is applicable under high injection, where the carrier concentration is dominated by light generation and is proportional to $n_i e^{qV_{oc}/2kT}$. Since we are interested in the efficiency limits with only intrinsic sources of recombination, we assume

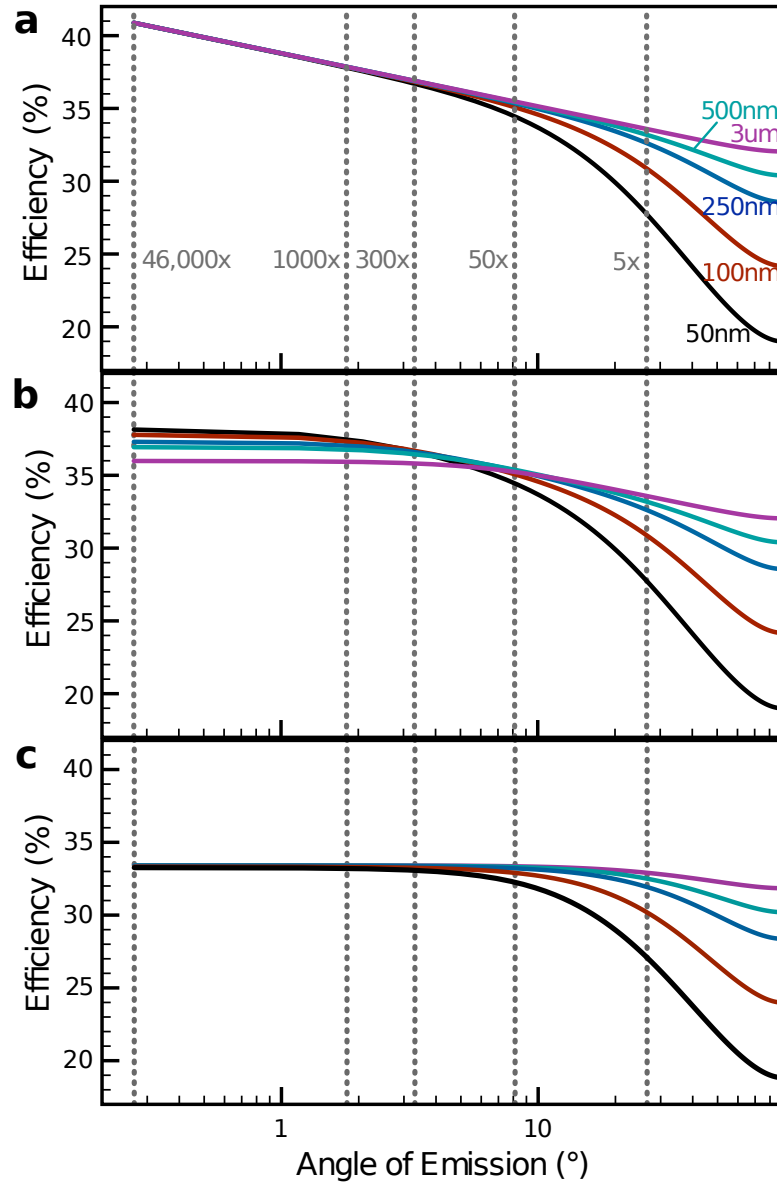


Figure 4.1. Detailed balance efficiencies as a function of emission angle for various thickness light trapping GaAs solar cells with thick silicon nitride cladding. In panel a, all recombination is assumed to be radiative with an ideal back reflector. In panel b, Auger recombination is accounted for assuming an ideal back reflector. In panel c, the back reflector is assumed to have 98% angle-averaged reflectivity, as is typical in silver, and Auger recombination is included. The dotted lines indicate the concentration factors which have the same degree of angular restriction to illustrate the tracking difficulty.

that the cell is very lightly doped, so it will operate in high injection. High quality material with a Shockley-Read-Hall lifetime greater than $14.3 \mu\text{sec}$ and surface recombination velocity less than 1.75 cm/sec for a 500 nm thick cell is required for Auger recombination to be dominant at open circuit.

With increased voltage from photon recycling, Auger recombination increases relative to radiative emission. Thus, as Figure 4.1b illustrates, the effect of Auger recombination is greatest for narrow emission angles, and there is little benefit for emission angles below one degree. Interestingly, thinner cells show the best performance for small emission angle because the Auger term is minimized while enhanced light trapping allows for full absorption.

4.3 Ideal and Non-Ideal Back Reflectors for a Light Trapping Cell

4.3.1 Effect of a Non-Ideal Back Reflector

While a nearly ideal back reflector may be achieved utilizing a dielectric stack reflector in air, a metallic back reflector is more likely to be cost effective [53]. However, an imperfect back reflector will reduce the absorbed solar flux and photon recycling via parasitic absorption of solar and radiatively emitted photons. Using expressions found in Section 3.4.2 in the previous chapter, we calculate efficiencies for a 98% reflective rear surface, as is typical for silver, in Figure 4.1c [54]. While the benefits of limiting emission angle persist, particularly for thinner cells, the maximum achievable efficiency is significantly reduced. In contrast to the ideal reflector case, the performance of cells of all thicknesses converge for sufficiently limited angles. While these results demonstrate the feasibility of the scheme, they also indicate the importance of a highly reflective back surface, and suggest that either dielectric or metallodielectric back reflectors with higher reflectivity may be worth the additional cost and fabrication difficulties.

4.3.2 Dielectric Mirrors Approaching Unity Reflectivity

Given the importance of an ideal back reflector for achieving maximum efficiencies with angle restriction scheme, it is important to understand how closely an ideal omnidirectional back reflector could be approximated with a real optical structure. For this purpose we examined a chirped, multilayer dielectric mirror, similar to the Bragg stacks mentioned in Chapter 1, with an air gap separating the cell and the mirror. Such dielectric omnidirectional reflectors with light incident from air have been fabricated and experimentally validated in the visible regime, with the results closely matching calculations [53]. However, we desire a mirror with high omnidirectional reflectivity from about 400 to 870 nm, while the previous workers used ZnS, which absorbs below 590nm. ²

We therefore have performed some simple calculations to show that our wavelength requirements can be achieved with a similar approach. Rather than a ZnS/SiO₂ stack, we consider a mirror made from alternating layers of TiO₂ and SiO₂, sacrificing index contrast for transparency in the blue. Figure 4.2 shows the results of these calculations [55]. We consider a dielectric stack with 200 TiO₂/SiO₂ layers, with an initial thicknesses of 125 nm and 190 nm, respectively, and linear chirping to 30% of the initial thickness values. For this structure, unity reflectivity is achieved or very closely approached for all angles across the wavelength range of interest, giving an angle and wavelength averaged reflectivity of 99.999%. We also consider a thinner structure with sixty TiO₂/SiO₂ layers, with initial thicknesses of 136 nm and 203 nm, respectively, and linear chirping to 30% of the initial thickness as before. Performance is excellent except at oblique angles, and is omnidirectional at the radiative emission wavelengths, giving an overall angle and wavelength averaged reflectivity of 99.6%. Depending on the cell thickness, such a reflector may give similar performance with less fabrication difficulty than the 200 layer stack. Thus, we find that a dielectric

²While there is solar radiation below 400 nm the external quantum efficiency in GaAs cells is low, owing to absorption in the window layer [39]. In addition, GaAs has absorption lengths less than 15 nm in this portion of the spectrum. Thus, more than 96% of the ultraviolet light is absorbed on the first pass in a 50 nm thick cell and avoids the back reflector.

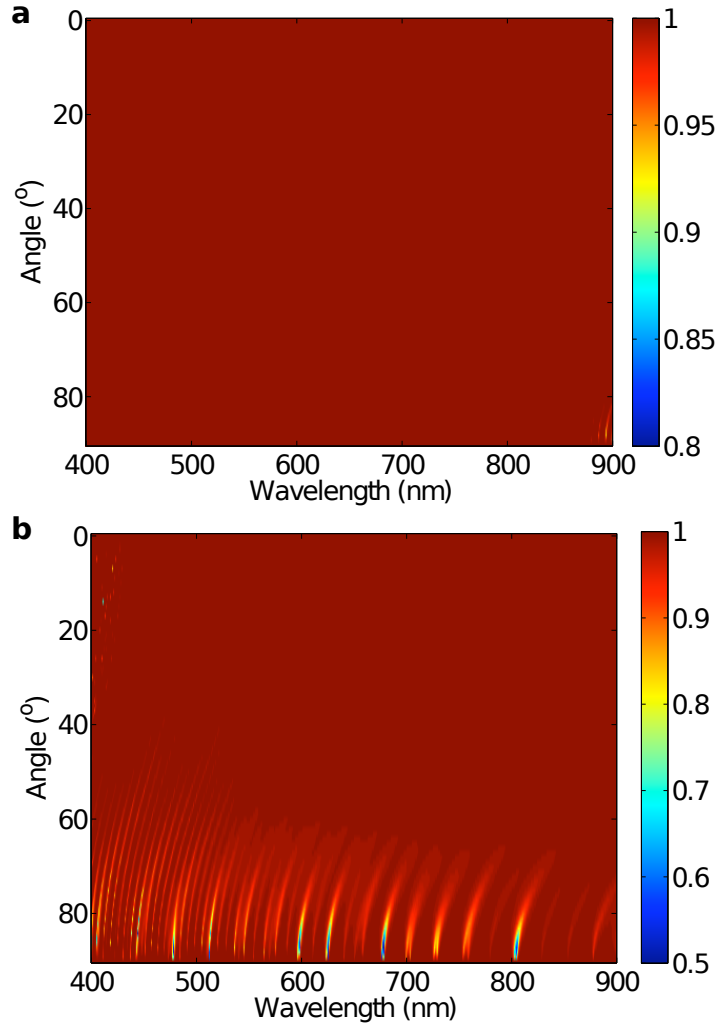


Figure 4.2. Calculated reflectivity in air as a function of incidence angle and wavelength from 400 to 870 nm. a) Reflector with 200 $\text{TiO}_2/\text{SiO}_2$ layers with initial thickness of 125 nm/190 nm and linear chirping to 30% of the initial thickness. b) Reflector with 60 $\text{TiO}_2/\text{SiO}_2$ layers with initial thickness of 136 nm/203 nm and linear chirping to 30% of the initial thickness.

stack with broadband omnidirectional calculated reflectivity closely approximating unity is achievable, and have also demonstrated a design that sacrifices reflectivity at oblique angles for simpler fabrication.

4.4 Comparison with a Planar Cell Geometry

Figure 4.3 gives analogous results for a planar, rather than light-trapping, cell geometry using expressions derived in Section 3.4.4 of the previous chapter. As we expect, thinner cells have low efficiencies in a planar geometry owing to poor absorption. Thus, for the Auger-limited case, significantly higher efficiencies are achievable with the light-trapping geometry. In fact, we would expect such a trend in any cell where bulk recombination processes, like Auger or Shockley-Read-Hall recombination, are dominant. However, with a metallic back reflector, the achievable efficiencies are similar in the light-trapping and planar cases, though these efficiencies are achievable in a much thinner cell with the light-trapping geometry. Thus, light trapping allows for much thinner cells in all cases, and with an excellent back reflector it allows for significantly higher overall efficiencies.

4.5 Comparison to Previous Work: The Radiative Efficiency Approach

Previously, Martí and co-workers have argued that a limited emission angle scheme would not be feasible in planar GaAs, as a ratio of non-radiative to radiative lifetime of 0.1 eliminated any benefit [32]. While a voltage dependent internal radiative efficiency is inherent in the more realistic Auger recombination model presented previously, we also consider a model which allows for explicit variation of the internal radiative efficiency. This allows for comparison with the previous work. We find that with a light-randomizing geometry even reasonable levels of non-radiative recombination are not disastrous to the scheme.

To include non-radiative recombination, we re-write the detailed balance equation

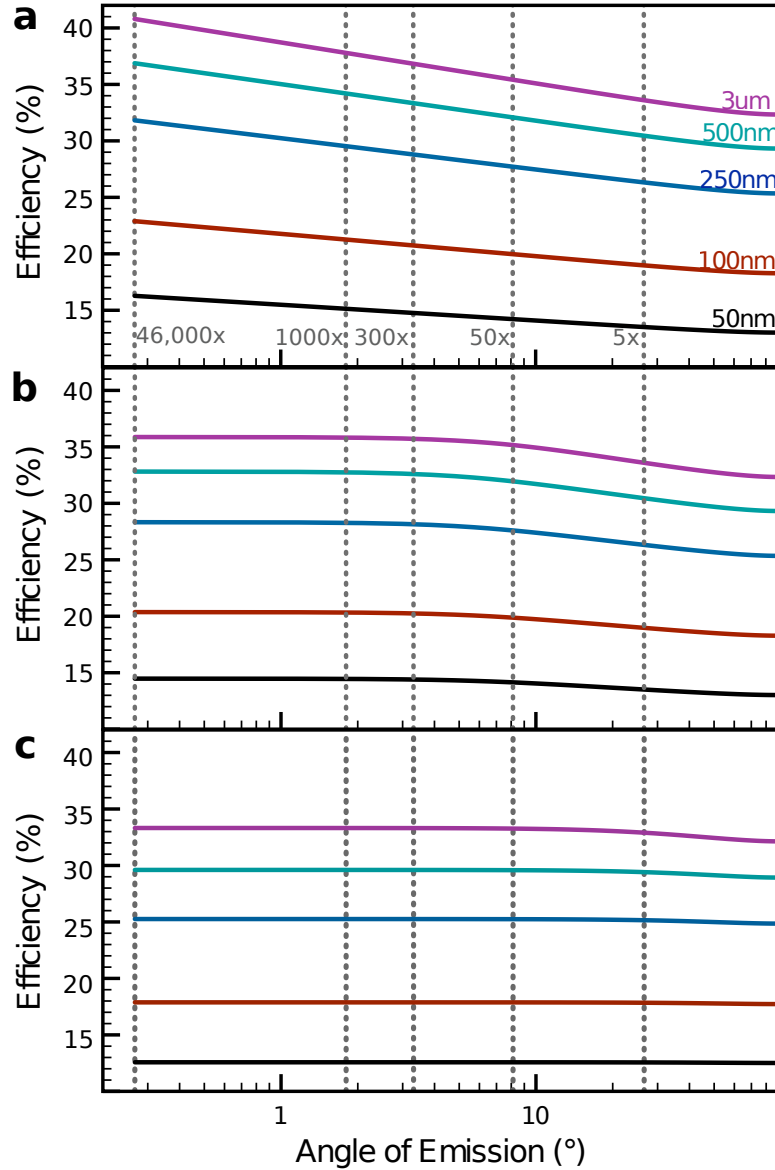


Figure 4.3. Detailed balance efficiencies as a function of maximum emission angle for various thickness planar GaAs solar cells. In panel a, all recombination is assumed to be radiative with an ideal back reflector. In panel b, Auger recombination is accounted for assuming an ideal back reflector. In panel c, the back reflector is assumed to have 98% angle-averaged reflectivity, as is typical in silver, and Auger recombination is also included. The dotted lines indicate the concentration factors which have the same degree of angular restriction to illustrate the tracking difficulty.

as:

$$\int_0^\infty S(E)a(E)dE = 1 + R \left[\int_{\Omega_c} \int_0^\infty a(E) \frac{2}{h^3 c^2} \frac{E^2}{e^{(E-qV_{oc})/kT} - 1} dE \cos(\theta) d\Omega \right] \quad (4.2)$$

where R times the radiative emission gives the non-radiative recombination [56]. Then the external radiative efficiency, or the fraction of recombination events that result in light escaping the cell, is:

$$\eta_{ext} = \frac{1}{1 + R} \quad (4.3)$$

Parallel to previous analysis of light emitting diodes, we have modified an expression relating the external and internal radiative efficiency of a randomizing bulk slab with an ideal back reflector to account for narrowing of the escape cone by a factor of $\sin^2(\theta)$ [46].

$$\eta_{ext} = \frac{\eta_{int} \sin^2(\theta)/4n^2}{\sin^2(\theta)/4n^2 + (1 - \eta_{int})\alpha W} \quad (4.4)$$

Considering the radiatively emitted light from a planar cell gives a parallel expression for the external radiative efficiency in this geometry:

$$\eta_{ext} = \frac{\eta_{int}(1 - a_{int})}{1 - \eta_{int}a_{int}} \quad (4.5)$$

where a_{int} is the probability that an internally emitted photon will be re-absorbed before it escapes the cell, which has been modified to account for a limited emission angle [57].

$$a_{int} = 1 - \frac{(1 - e^{-2\alpha W}) \sin^2(\theta)}{4n^2\alpha W} \quad (4.6)$$

For non-unity internal radiative efficiency, external radiative efficiency is reduced as the emission angle is limited, leading to relatively more non-radiative recombination. Also, thicker cells have lower external radiative efficiency for a given internal radiative efficiency, as we expect. In the above expressions, the fraction of the light within the escape cone under no angle restriction is approximated as $1/4n^2$, a ray optics result. To account for modal structure in thin cells, we replace $1/4n^2$ with half the fraction of total optical modal density from radiating, as opposed to trapped,

modes as defined by the Stuart and Hall absorptivity model presented in the previous chapter [45]. This corresponds to the escape cone in the bulk ray optics limit with the factor of one half due to escape occurring only from the top of the cell. For a closer comparison to Martí's model, the cladding layers considered in the main manuscript are omitted in the modal calculation, and are replaced by air.

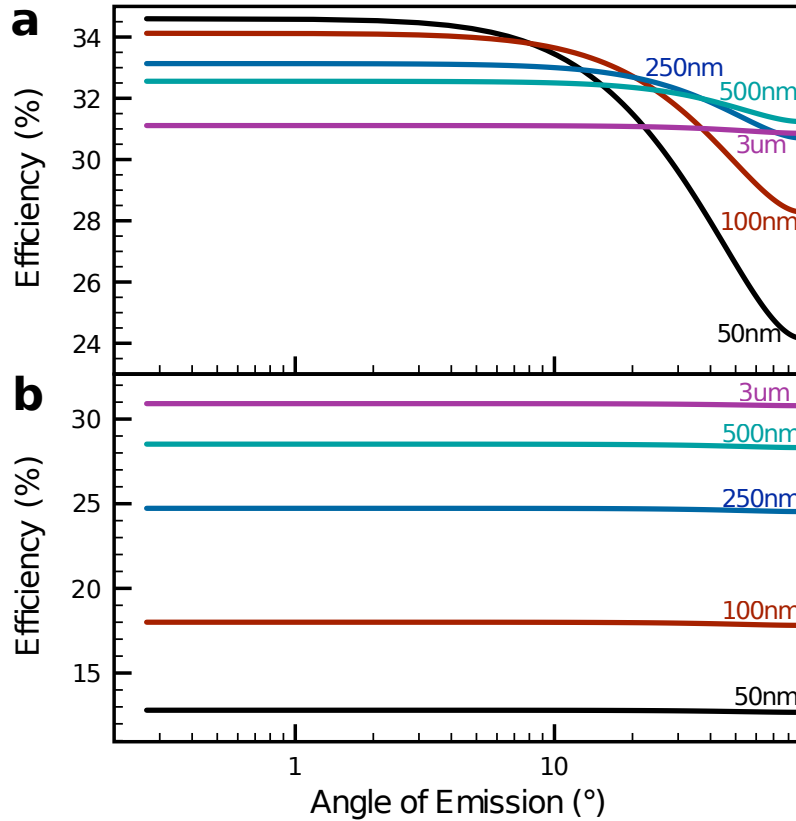


Figure 4.4. Detailed balance efficiency calculations for a textured (a) and planar (b) cell geometry with a constant internal radiative efficiency of 90%. An ideal back reflector and an air front interface are assumed. Note that for the textured case the 3 μm thick cell performs worse than the 500 nm thick cell. This is due to reduced external radiative efficiency in the 3 μm cell and nearly full light absorption in the 500 nm cell.

Figure 4.4 shows efficiency results for 90% internal radiative efficiency in the planar and light trapping cases. As noted, previous work considering non-randomizing cells

found that benefits did not persist for non-unity internal radiative efficiency, and our results are consistent with this conclusion, despite slight differences in the models [32]. However, for a given internal radiative efficiency and thickness a light trapping cell will have a larger external radiative efficiency and less non-radiative recombination than a non-randomizing cell. Thus, as in the main manuscript, there are significant efficiency benefits to angle restriction in these cells, particularly if the cells are thin. Clearly, then, a light trapping structure is key to overcoming non-radiative losses and obtaining the maximum benefit in an angle restriction strategy.

4.6 Radiative Efficiency in Current GaAs Cell Technology

While this chapter has suggested the significant advantages possible with angle restriction, it is unclear if current GaAs technology has sufficiently low non-radiative recombination to benefit. Recently, there has been considerable progress in increasing the world record single junction efficiencies via GaAs solar cells with high voltages, suggesting a high material quality and a good back reflector [39, 58]. While these cells are likely thick with a planar geometry and are thus unlikely to benefit significantly from angle restriction, they are an excellent example of current GaAs material quality, and external radiative efficiencies have been calculated [37]. Thus, by assuming a $2\mu m$ thick planar cell with 98% back reflectivity, we can estimate the internal radiative efficiency, and determine the feasibility of the angle restriction approach with current material quality. Using the same procedure as was used above to find η_{ext} for a planar cell with an ideal reflector, we find

$$\eta_{ext} = \frac{\eta_{int}(1 - a_{tot})}{1 - \eta_{int}a_{cell}} \quad (4.7)$$

where a_{tot} is the total reabsorption of light in the cell and loss back reflector and a_{cell} is the reabsorption of light in the cell. Then,

$$a_{tot} = \left(1 - \frac{1}{2n^2}\right) + \frac{1}{2n^2}a_{tot,esc} \quad (4.8)$$

and

$$a_{cell} = a_{tot} = \left(1 - \frac{1}{2n^2}\right) (1 - a_{refl,trap}) + \frac{1}{2n^2}a_{cell,esc} \quad (4.9)$$

where esc denotes light within the escape cone, $trap$ denotes light outside the escape cone, and a_{refl} denotes light absorbed in the lossy reflector. Finally, then:

$$a_{tot,esc} = \left(1 - \frac{1 - e^{-\alpha L}}{\alpha L}\right) + \frac{1}{2}R \left(\frac{1 - e^{-\alpha L}}{\alpha L}\right) (1 - e^{-\alpha L}) + \frac{1}{2}(1 - R) \left(\frac{1 - e^{-\alpha L}}{\alpha L}\right) \quad (4.10)$$

$$a_{cell,esc} = \left(1 - \frac{1 - e^{-\alpha L}}{\alpha L}\right) + \frac{1}{2}R \left(\frac{1 - e^{-\alpha L}}{\alpha L}\right) (1 - e^{-\alpha L}) \quad (4.11)$$

$$a_{refl,trap} = \frac{(1 - R)(1 - e^{-\alpha L})}{2} \frac{(1 + e^{-\alpha L})}{\alpha L (1 - Re^{-2\alpha L})} \quad (4.12)$$

where R is the reflectivity, $L = W/\cos(\theta)$, and we average over all angles within and outside the escape cone. For an external radiative efficiency of 22.5%, as calculated by Green, we find an internal radiative efficiency of 92.6%, very similar to the 90% IFY assumed in figure 2 [37]. Thus, a thin, light trapping cell with material quality similar to current GaAs technology should show significant benefit with an angle restriction scheme, illustrating its immediate feasibility.

4.7 Broadband Angle Restrictor Designs

Throughout the previous analysis, we have assumed a device which facilitates light in-coupling within the specified angle without loss, while excluding all other light spanning wavelengths from the blue edge of the solar spectrum to the band edge of GaAs at 870 nm. While there has been some discussion in the literature about

possible strategies for designing such an angle restricting coupler, we are not aware of designs whose performance has been optically analyzed [30, 59]. Other than the design of an emission angle limiting coupler, our scheme relies largely on existing technologies, such as tracking and high quality GaAs cells. Thus, to complete the feasibility argument, two broadband angle restrictor designs are presented and their performance analyzed, with experimental work showing the early fabrication of one design.

Figure 4.5a,b illustrates a coupler that utilizes total internal reflection within dielectric cone-type structures based on a modified compound parabolic concentrator (CPC) shape [60]. The cone-like structures have the side curvature of a CPC, but the curvature of each portion of the side, as defined by the CPC acceptance angle, is adjusted so that the top of the cone-type object has a hexagonal cross-section, allowing for close-packing. The small bottom openings are circular, even though the tops are hexagonal. A double close-packed array of cones, separated by a perfect, broadband reflector with small holes at the cone bottoms, completes the coupler design. The broadband reflector is important for reflecting light entering at large angles back into the solar cell. Unlike a single array of these cone type structures, the double array gives uniform, near normal illumination of the cell, minimizing reflection losses and avoiding the deleterious effects of non-uniform illumination on solar cell performance. Because this coupler functions on ray optics principles, it is naturally broadband.

A thinner coupler allows for easier integration with existing systems and lower materials cost. Since this coupler is based on ray optics, it can be built on any scale much larger than the wavelength. To minimize the coupler height, we set the scale so that the reflector openings are in the ray optic limit ($4\mu\text{m}$ diameter). As the maximum CPC acceptance angle decreases, narrowing the allowed emission angles, the optimal height of the cone structure increases [60]. Thus, to more strictly limit the emission angle, we must either tolerate a thicker coupler structure or truncate from the optimal CPC height.

In Figure 4.5c, we compare three designs limited to 1mm in height by using ray tracing to determine the reflectivity. For the design marked 3.7° , with the least

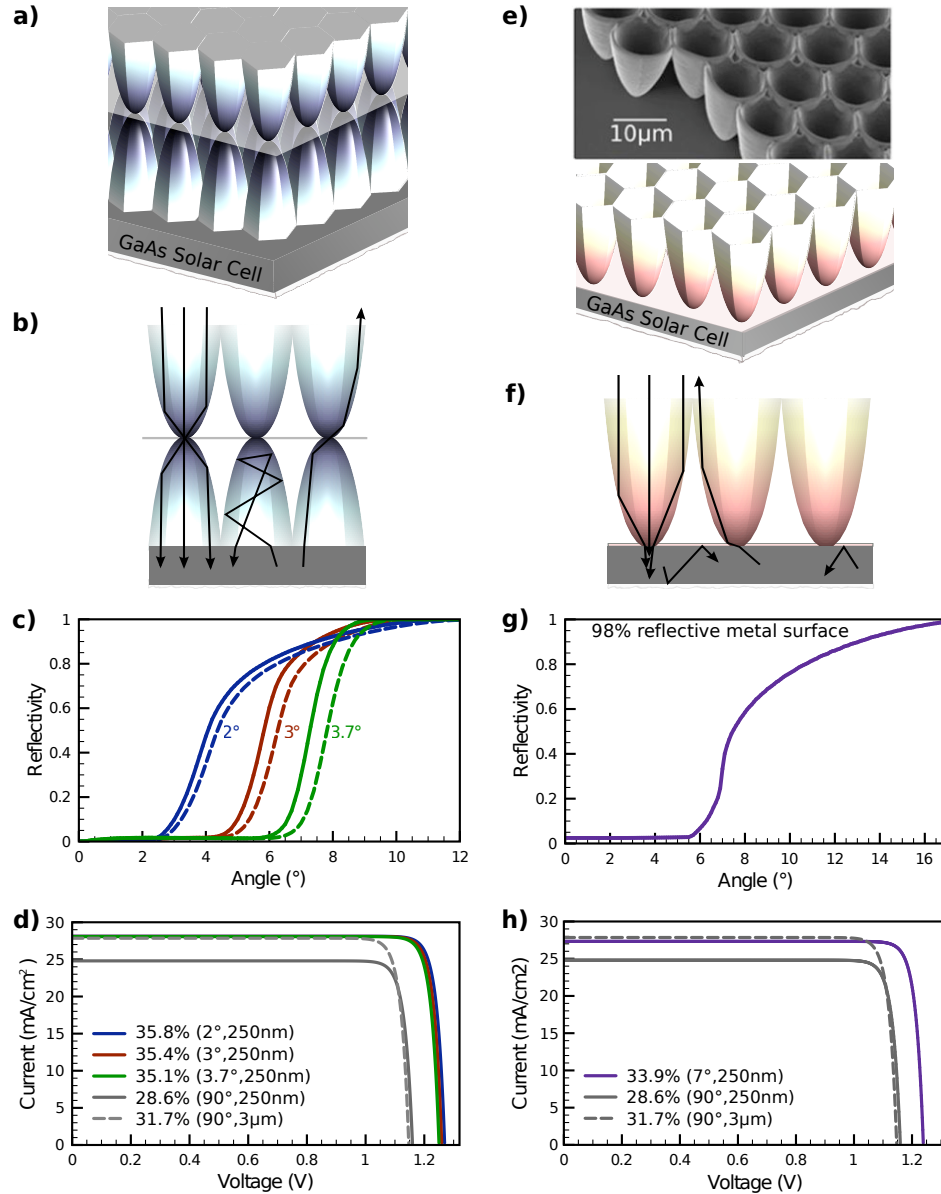


Figure 4.5. a,b) Dielectric coupler schematic. c) Calculated dielectric structure reflectivity for 300 nm (dashed) and 870 nm (solid) light. Labels indicate maximum emission angle that defines the sides. Observed angles are larger due to refraction in the dielectric. d,h) Detailed balance I-V curves for light trapping cells with Auger recombination and an ideal back reflector with and without (90°) angle restrictors. Legends give efficiency, cell thickness, and design angle. e,f) Schematic of metal array coupler and SEM of fabricated structure. g) Calculated reflectivity for a 98% reflective metal surface.

angular restriction, there is no truncation, while for design with maximal restriction, marked 2° , the shape is truncated to approximately 30% of its optimal height. Because of the large size of the coupler relative to the wavelengths of interest, we analyze the coupler performance using ray tracing, with silicon nitride dielectric structures. The ray tracing was performed using a home-built Matlab code that traces rays at each in-plane and out-of-plane angle, and averages rays starting at different points on the cone top and over the in-plane angles, to find the results in Figure 4.5c. The ray traces also assume ideal anti-reflection coatings and the angle restrictor-cell and angle-restrictor air interfaces. We see excellent angular cutoff, and a broadband response, as illustrated by the curves for 300 and 870 nm. For the more truncated designs, the angular cut-off is less abrupt, but begins at smaller angles.

The ray tracing results can then be incorporated into the detailed balance calculation by replacing the factors of $\sin^2(\theta)$ in the previous calculations with angular transmission averages. Figure 4.5d shows current-voltage curves for the three different coupler designs on a 250 nm thick cell with Auger recombination and an ideal back reflector, as well as results for cells with no angularly restricting coupler. We see that the most severely truncated design performs the best, with a four absolute percent efficiency increase over a thicker cell with no coupler, and a seven absolute percent increase over a no-coupler cell of the same thickness. While there is an approximately 100 mV increase in open circuit voltage, the short circuit current only increases by about 3 mA/cm², so there should be no significant heating or series resistance effects, as in concentrator systems. Thus, this coupler design could be used to experimentally demonstrate significantly improved performance due to limited emission angle.

In Figure 4.5e-h, we analyze a similar coupler that is easier to fabricate, and show an initial fabrication of the structure over a small area using two-photon lithography. This coupler has a single, rather than double, array and uses metal coated cups, rather than total internal reflection in a dielectric. To limit degradation in device performance, the illuminating holes at the bottoms of the cups should be within the carrier diffusion length, so the coupler must be relatively small (micron) scale while remaining ray optical. With 98% metal reflectivity and neglecting the gaps between

cups, ray tracing results coupled to the detailed balance model suggest a significant performance increase.

The fabricated structures shown in Figure 4.5 were written into IP-L resist using the Nanoscribe Photonic Professional two-photon lithography system. To prepare the sample for writing, optical coupling fluid was placed on one side of a glass slide, and IP-L placed on the other. After writing, development in 2-propanol for 20 minutes, which removes all unwritten IP-L and the optical coupling fluid, was followed by drying of the glass slide. The structures written in resist remained on the glass slide, and were then coated with about 20 nm of sputtered chromium to aid conductivity for imaging. While these devices show the feasibility of creating such a structure, two-photon lithography is not suitable for large area fabrication, and some sort of stamping procedure would be desirable. In addition, further work would be required to deposit high reflectivity metallic coatings in such high aspect ratio structures [61].

4.8 Narrowband Angle Restrictor Design

While it is clear that light trapping GaAs cells are preferable for angle restriction, world-record quality cells made currently are planar [39, 43]. This is due to the difficulty of texturing an epitaxially grown film while maintaining high material and surface quality. In fact, to make a light trapping GaAs cell adding a transparent high index light randomizing surface, such as a textured layer of titanium dioxide, silicon nitride, or gallium phosphide,³ seems the most likely approach. In a planar cell, only photon recycling may be enhanced with angle restriction, as there is no mechanism to randomize incoming light, limiting the cell to dual pass absorption. Since the emitted light of interest for photon recycling occurs over a narrow wavelength range corresponding to the cell photoluminescence (approximately 800-870 nm in GaAs),

³While gallium phosphide is not transparent over the entire range of interest, light above the gallium phosphide bandgap may be largely absorbed on the first pass through the cell, depending on the cell thickness. Thus, gallium phosphide, with its higher refractive index, may be an attractive option for backside scattering.

only a narrowband angle restricting structure is required. Furthermore, a narrowband structure allows much of the diffuse solar

As shown in Figure 4.6b, the narrowband angle restrictor design consists of alternating high and low index with large refractive index contrast to increase the angular range of reflection [7, 62, 63]. While the design is not strictly periodic, the angular properties can be understood from the Bragg condition

$$\cos \theta = \frac{m\lambda}{2\Gamma} \quad (4.13)$$

where θ is the angle of maximum reflectivity, λ is the wavelength, Γ is the period of the multilayer, and m is an integer [64]. For shorter wavelengths maximum reflectivity occurs away from normal incidence, providing angle restriction for emitted light and excellent transmission at normal incidence in both the designed and fabricated structures. In a standard Bragg stack with discrete high and low index layers, the Bragg condition is applicable and angle restriction occurs. However, such simple structures also suffer from undesirable reflections at normal incidence owing to second order ($m = 2$) reflecting bands, as well as ripple-type reflections (see Figure 5.2 in the next chapter). Modifying these structures to include gradual index variation, as shown in Figure 4.6, known as a rugate or graded index structure, eliminates these undesirable reflections, allowing J_{sc} to be maintained with angle restriction.

Figure 4.6 illustrates a rugate design for angle restriction in GaAs, based on reference [65], which eliminates both the second-order reflecting band and the smaller ripple-type reflections near normal incidence [66-68]. Unlike the simple Bragg stacks discussed in the next chapter, this angle restrictor is designed to perform under glass, as in an installed solar array. Our concept is that the angle restrictor would be deposited directly on the cell, with the glass covering attached with an index matched polymer to avoid any air gaps between the glass and angle restrictor. For a comparison case without angle restriction we consider a quintic-type graded index anti-reflection (AR) coating with the same index range and thickness as our angle restrictor deposited at the same glass/cell interface [69]. Thus, the performance of the graded

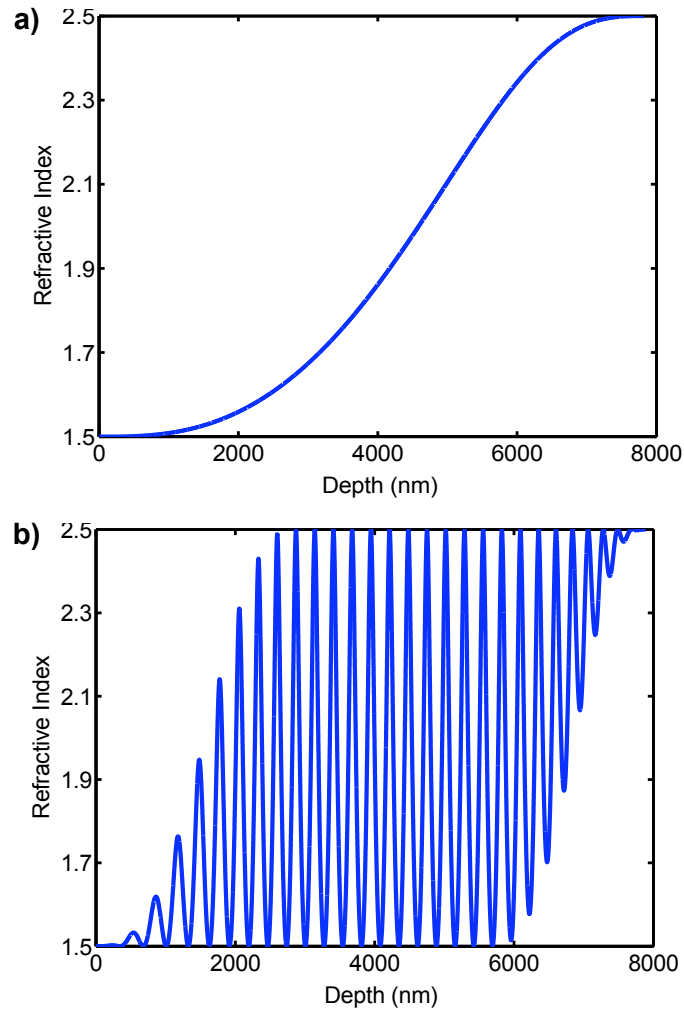


Figure 4.6. a) Refractive index profile of the graded-index AR coating used as a comparison case. Index range and optical thickness are matched to rugate angle restrictor. 0 represents the interface with the covering glass. b) Refractive index profile of rugate angle restrictor. 0 represents the interface with the covering glass.

index angle restrictor is compared to a graded index AR coating, assuming both are under glass.

For this point design we assume the minimum refractive index in the rugate angle restrictor and graded index AR control is 1.5 and assume a $\text{TiO}_2/\text{SiO}_2$ co-deposition process with a maximum index of 2.5 [70-72]. (We note that if high index TiO_2 cannot be achieved with co-deposition, similar increases in performance can be achieved with lower index TiO_2 films, though the currents and overall efficiencies are somewhat reduced for both the graded index AR control and the rugate angle restrictor due to increased reflection.) Figure 4.7 gives the calculated reflectivity for both the graded index AR control and the rugate angle restrictor design [43, 55]. The rugate angle restrictor design has normal incidence transmission very similar to the graded index AR control and nearly complete suppression of the second-order reflecting band [65, 69]. Angle restriction to about 20° is achieved near the peak in the emission spectrum, and, away from the angle restricting region, transmission is very similar for both the graded index AR control and the rugate angle restrictor across all angles. Thus, for most of the spectrum, diffuse light should be utilized equally well for the angle restrictor and graded index AR coating.

To quantify this further, in Figure 4.8 we estimate the short-circuit current in the cell as a function of the light incidence angle based on the cell internal quantum efficiency (IQE) spectrum and the transmission spectrum, including reflections from the top surface of the glass. The predicted current with the rugate angle restrictor is 99.98% of the graded-index AR comparison value at normal incidence, and remains above 99% up to 25 degrees. Furthermore, the minimum current with the rugate angle restrictor at any angle is 77% of the graded index AR control value, so we expect a very large portion of the diffuse light to be captured with this design.

Next, we evaluate the efficiencies of cells with the graded index AR control and rugate angle restrictor using the modified detailed balance model with short-circuit current values from Figure 4.8. We use a multipass model to account for reflections between the cell/glass interface, where the rugate angle restrictor or graded index AR is deposited, and the glass/air interface. Unlike previous cell models considered

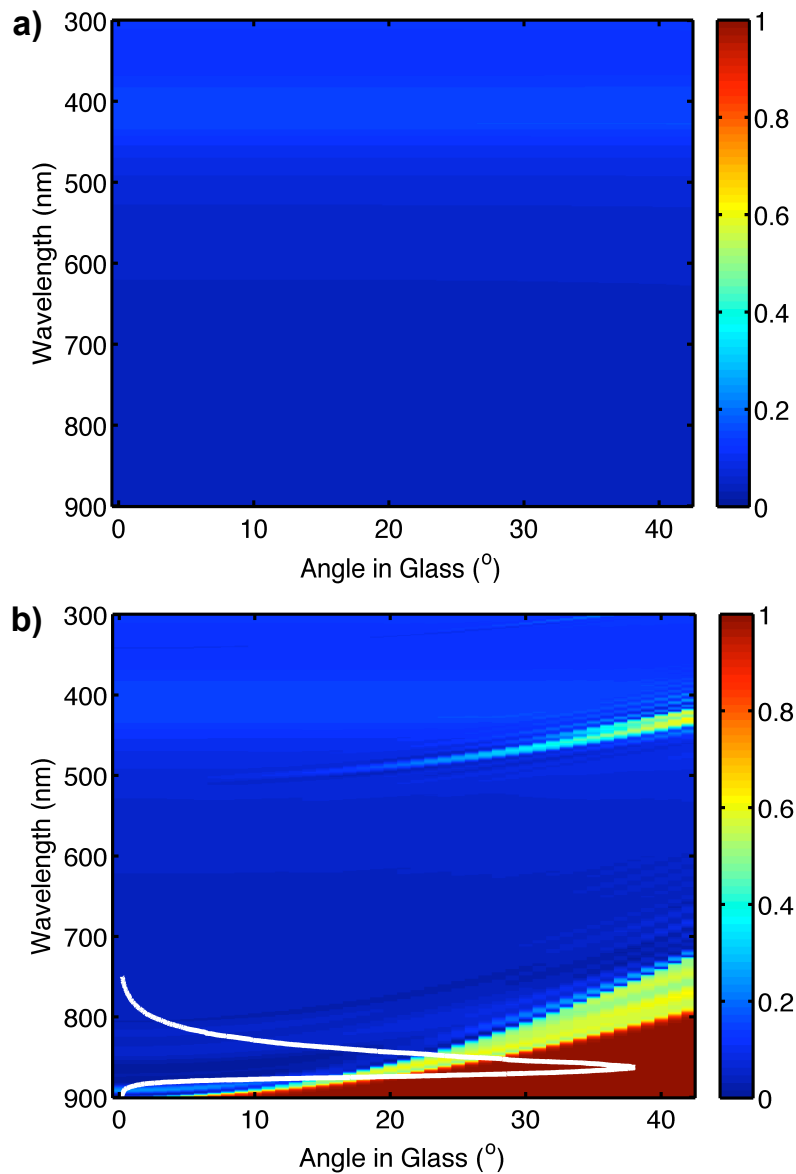


Figure 4.7. a) Calculated reflectivity values for the graded index AR coating comparison structure. Structure is assumed to be under glass and immediately above a GaAs cell with 20 nm AlInP window layer. b) Calculated reflectivity values for the rugate angle restrictor design. Structure is assumed to be under glass and immediately above a GaAs cell with 20 nm AlInP window layer. All calculations use the transfer matrix method with the rugate profile divided into 1 nm thick layers.

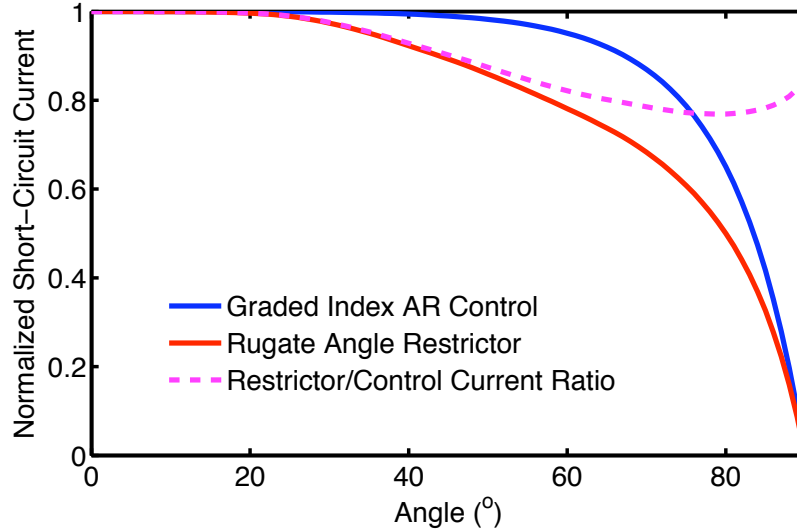


Figure 4.8. Predicted J_{sc} as a function of light incidence angle for the rugate angle restrictor (red line) and graded index AR control (blue line) structures under glass. Values are normalized to the graded index AR structure at normal incidence. The ratio of the J_{sc} values is also plotted (dotted purple line).

in this chapter, to facilitate comparison with experimental cells, a surface recombination velocity is included, as in Equation 3.4. As in Figure 4.9, we vary the surface recombination velocity S , assuming an ideal back reflector, thereby varying the ERE up to the Auger limit. However, as the Auger limit is dependent on cell thickness and doping, we also perform the calculation at 100% ERE. As we expect, for higher ERE cells there is a larger improvement in efficiency with angle restriction. As shown in 4.9, for this point design we expect a 1% relative efficiency increase for cells with ERE values corresponding to the current GaAs world record [38], and a 2.5% relative efficiency increase for Auger limited cells with a 27mV V_{oc} enhancement.

Because of this design's wide acceptance angle, it can also be used under a conventional concentrator, rather than to collect diffuse light. Because currents are maintained out to 25° , we assume a conventional concentrator with an input angle of 2 degrees, and an output angle of 25 degrees, operating at the thermodynamic concentration limit of 146.6 suns [60]. We further assume that light output from

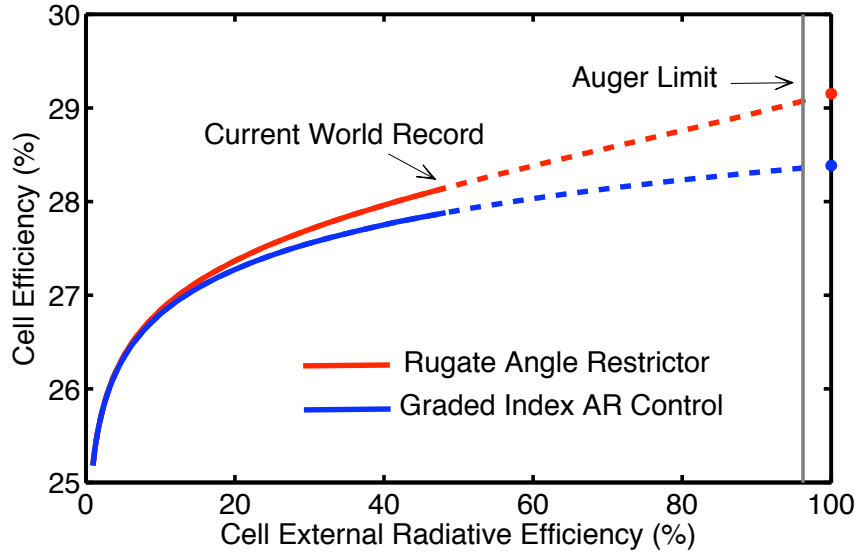


Figure 4.9. Predicted efficiency as a function of external radiative efficiency for the rugate angle restrictor (red) and the graded-index AR control (blue). The solid line indicates the range ERE values attainable with current GaAs cells. The end of the solid line corresponds approximately to ERE values for current world record cells [38]. The dotted line indicates ERE values beyond current world record cells and terminates at the Auger limit (grey line). Finally, the dots indicate efficiency values at the radiative limit (ERE=100%). Note that in the ERE range considered experimentally (3-16%) the angle restrictor and control lines are nearly overlaid, indicating a small voltage enhancement with angle restriction in this region, similar to the voltage enhancement we observed experimentally.

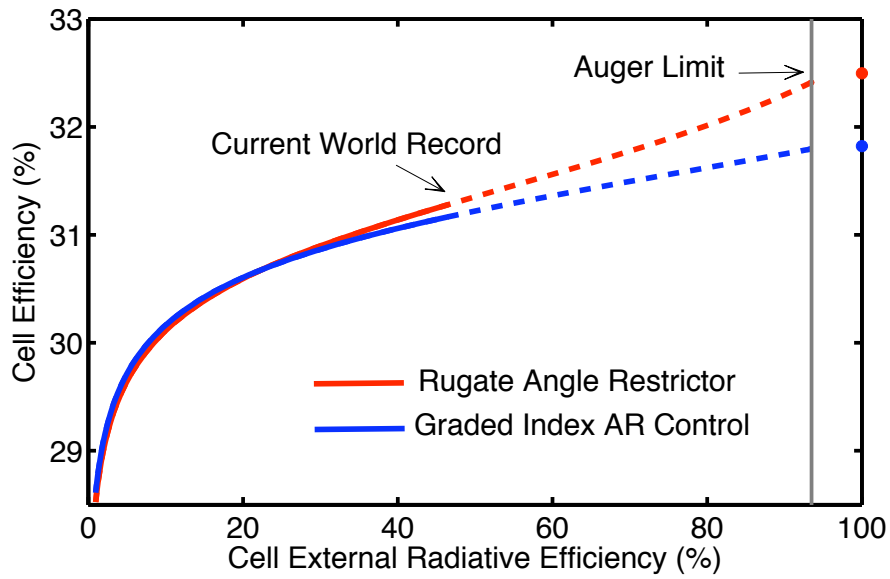


Figure 4.10. Predicted efficiency as a function of external radiative efficiency for the rugate angle restrictor (red) and the graded index AR control (blue) under a 146.6x concentrator with 25 degree output angle. The solid line indicates the range ERE values attainable with current GaAs cells. The end of the solid line corresponds approximately to ERE values for current world record cells at one sun [38]. The dotted line indicates ERE values beyond current world record cells and terminates at the Auger limit (grey line). Finally, the dots indicate efficiency values at the radiative limit (ERE=100%).

the concentrator is evenly distributed over the angular range from 0 to 25° , and determine the predicted current and efficiency for the cell. As in figure 4, at low ERE values current losses from the wide range of input angles outweigh voltage gains, and efficiencies are slightly reduced with angle restriction. However, with a high ERE cell, efficiency gains with angle restriction are possible under fairly high concentrations.

4.9 Conclusions

Developing a detailed balance model for a thin, light trapping GaAs solar cell with limited emission angle, we have found efficiencies above 38% may be achievable with a single junction solar cell. We identify a regime of efficiencies significantly higher than those previously predicted for realistic cells with limited emission angle, by maximizing both light trapping and photon recycling effects. A light trapping geometry, high quality material, an excellent back reflector, and a very thin cell are critical to reaching the highest single junction efficiencies. A metallic back reflector allows for the use of very thin cells while maintaining, and slightly improving, efficiency relative to a thick non-angle restricted cell. However, much larger efficiency benefits are possible with an ideal back reflector, which can be closely approximated by a dielectric mirror. These results suggest that limiting emission angle with a light trapping GaAs cell and an excellent back reflector could provide a new route to achieving high efficiencies without a tandem or third generation cell.

Encouragingly, this scheme relies largely on existing technology, with the exception of a low-loss, broadband, angularly restricting coupler. We therefore analyzed two broadband angle restrictor designs, found that these couplers could produce significant performance increases, and demonstrated initial fabrication of one design. Finally, while broadband couplers may be preferable for light trapping cells, there is little benefit for planar cells where photon recycling is the only benefit. For current planar cells, we presented a rugate structure point design, and illustrated that a 1% efficiency benefit could be realized with existing cells. Thus, we have identified a new regime of very high single-junction efficiencies achievable by limiting emission angle,

laid out the critical factors necessary to realizing these efficiencies, and considered both broadband and narrowband angle restrictor designs.

Chapter 5

Experimental Demonstration of Enhanced Photon Recycling in GaAs Solar Cells

5.1 Motivation

For ideal solar cells where all recombination is radiative, photons emitted from the cell are the sole source of carrier loss, as in the detailed balance limit introduced in Chapter 3 [29]. Cells approaching this radiative limit have significantly higher efficiencies, as evidenced by recent world record GaAs cells, and can also exhibit new effects owing to the significant number of radiatively emitted photons [39, 43, 73]. As we have shown previously, optically limiting the angles of emitted light causes emitted photons to be recycled back to the cell, leading to enhancement in voltage and efficiency. Despite this theoretical prediction, until recently even the highest efficiency solar cells were not close enough to the radiative limit for such an effect to be observed [32, 74].

However, with the introduction of cells lifted off the growth substrate, GaAs cells have shown significant gains in efficiency due to V_{oc} increases, indicating an increase in the external radiative efficiency (ERE) of the cell [39, 43, 73]. In these lifted-off GaAs cells radiatively emitted photons are reflected from a metallized back surface instead of being absorbed in the substrate, resulting in a large increase in ERE and V_{oc} [40, 73]. As radiative recombination is dominant in high quality GaAs, these lifted-off cells perform near the radiative limit and are therefore suitable for experimentally demonstrating enhanced photon recycling and V_{oc} via angle restriction of emitted light. In fact, it was recently demonstrated that a voltage increase could be observed

in such cells by placing a reflecting dome above the cell to recycle emitted photons [75].

Here, as proof of concept, we demonstrate enhanced photon recycling and V_{oc} experimentally using an optical element with angle restriction only over the narrow wavelength range of emitted light in GaAs that is placed on a high quality GaAs cell. We have designed a dielectric multilayer angle restrictor with excellent normal incidence transmission and high reflectivity at oblique angles for radiatively emitted wavelengths. Using this narrowband angle restrictor with a high quality GaAs cell, we observe enhanced photon recycling and a resulting voltage increase. In other words, simply placing an angle restrictor on the cell causes a voltage increase of 3.6 mV without a change in current. In addition, we observe a 12% decrease in the radiative component of the dark current, which is consistent with the observed V_{oc} increase. Considering a variety of cells, the largest V_{oc} enhancements occur in cells that are closest to the radiative limit, with maximum ERE values of 15.7%. Finally, we see that more closely coupling the angle restrictor to the cell leads to greater V_{oc} gains, emphasizing the optical nature of the enhancement.

As was shown in Chapter 3, assuming the V_{oc} does not closely approach the bandgap, we may approximate the V_{oc} under illumination in the radiative limit as:

$$V_{oc} \approx kT \ln \left(\frac{\int_{E_g}^{\infty} S(E)a(E)dE}{\int_{\Omega_c} \int_{E_g}^{\infty} a(E) \frac{2}{h^3 c^2} \frac{E^2}{e^{(E-qV_{oc})/kT} - 1} dE \cos(\theta) d\Omega} \right) = kT \ln(J_{sc}/J_0) \quad (5.1)$$

where J_{sc} is the short-circuit current and J_0 is the dark current, which is solely due to radiatively emitted light. Restricting the emission angle causes photons generated by radiative recombination to be recycled and reabsorbed within the cell rather than emitted. Thus, enhanced photon recycling via angle restriction reduces J_0 and increases V_{oc} . For realistic cells, emitted light forms a larger fraction of J_0 in cells closer to the radiative limit. Thus, high ERE cells, like the GaAs cells in these experiments, are required for J_0 to be reduced sufficiently with angle restriction that a voltage increase may be observed. Furthermore, higher ERE cells should show larger voltage increases. For this reason, though the voltage increases in this proof-of-concept

experiment are modest, further improvements in GaAs cell technology, including the introduction of light trapping cells as discussed in Chapter 4, could significantly increase the performance benefits from angle restriction.

For terrestrial applications, we envision a flat plate, one sun, angle restricting system with high quality GaAs cells. While tracking may be beneficial, high accuracy tracking is not required as dielectric angle restrictors have a relatively large acceptance angle. Furthermore, for cells in the ERE range considered here, narrow angle restriction has limited benefit, as non-radiative recombination limits the possible voltage increase. Additionally, recent work has demonstrated the fabrication of high ERE cells in other III-V materials, notably GaInP, suggesting that this approach will become more broadly applicable with continued cell development, and could easily be incorporated with multijunctions [76]. Use with these cell technologies also suggests early applications in military and space solar, where efficiency and weight are paramount.

5.2 Narrowband Multilayer Angle Restrictor

While the previous chapter focused on broadband ray optical angle restrictors with light trapping cells, the cells in this experiment are planar with high reflectivity specular back reflectors that are metallic, with reflectivity of 75.5%, or metallodielectric, with reflectivity of 99.7%. The calculated reflectivity values refer to band edge (873 nm) emission angle-averaged within the GaAs. As the solar cells are planar and do not incorporate light trapping, only the photon recycling enhancement will be observed, as shown in Figure 5.1, and absorption will be dual pass. As enhanced photon recycling is the only angle restriction effect, we utilize a dielectric multilayer that provides angle restriction only over the narrow range of wavelengths at the semiconductor band edge where the GaAs cells emit light (see Figure 5.2). This narrowband angle restriction allows diffuse, non-normal incidence light to enter over most of the spectral range, as with the rugate structures shown in Section 4.8. Capturing this diffuse light gives significant current enhancements relative to a broadband concentra-

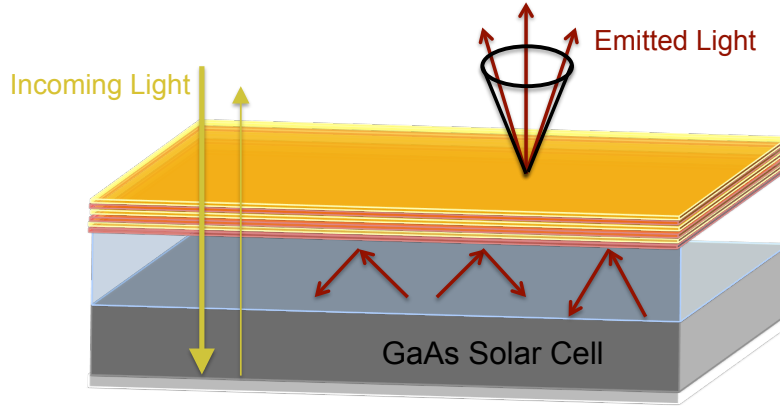


Figure 5.1. With a planar cell, absorption of incoming light is dual pass, regardless of angle restriction. In fact, slight reductions in current are observed owing to losses in the angle restrictor. However, enhanced photon recycling of emitted light and resulting voltage increase will still occur, as emitted light is randomized. As light is emitted only over a narrow wavelength range, only narrowband angle restriction is required.

tor or angle restrictor. In addition, potential losses due to tracking errors are greatly reduced, and simpler, cheaper trackers may be utilized. As was shown in Section 4.8, we envision depositing such an angle restrictor in place of a traditional AR coat, so the cost derives only from the added layers relative to a traditional AR coat.

As shown in Figure 5.2b, the angle restrictor design consists of alternating high and low index layers with large refractive index contrast to increase the angular range of reflection [7, 62, 63]. While the design is not strictly periodic, just as in Section 4.8, the performance can be understood with reference to the Bragg condition (Equation 4.13). As shown in Figure 5.2, for shorter wavelengths maximum reflectivity occurs away from normal incidence, providing angle restriction for emitted light and excellent transmission at normal incidence in both the designed and fabricated structures. We note that total internal reflection owing to the high index of GaAs already provides significant photon recycling within the cell, and despite this, there is still a substantial loss due to emitted light, as ERE estimates indicate [73]. As the measured reflectivity in air (Figure 5.2d) demonstrates, the dielectric structure provides photon recycling

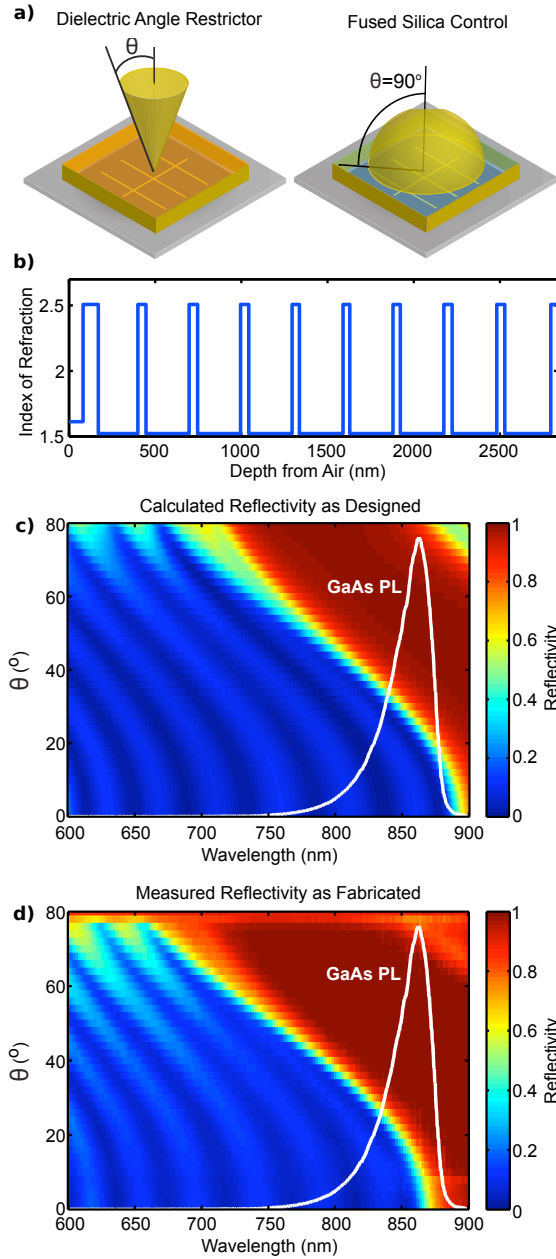


Figure 5.2. a) Experimental set-up: high quality GaAs cell placed in optical contact with either a dielectric angle restrictor deposited on fused silica (left) or a bare fused silica control (right). Emission angles shown schematically in yellow. b) The refractive index profile at 800 nm for dielectric multilayer angle restrictor design. (0 is the air interface.) c,d) Calculated (c) and measured (d) reflectivity for the dielectric multilayer as a function of angle in air and wavelength. Photoluminescence spectrum (white line) indicates the wavelengths where angle restriction is desired.

of light that would otherwise be emitted. This enhanced photon recycling occurs in addition to the photon recycling via total internal reflection, which is unaffected by the dielectric structure.

5.3 Dark Current Measurements

Theory clearly indicates that enhanced photon recycling via angle restriction will result in a reduction of the radiative dark current. We therefore measured the dark current characteristics of a single cell under both the angle restrictor and a bare fused silica control optic, as in Figure 5.2a. Fused silica index matching fluid was applied at the interface of the cell and the fused silica substrate to avoid extraneous reflections, and the edges of both optics were coated with a gold reflector to avoid light escape from the sides. (See Section 5.8 for further details.) In the high voltage region near V_{oc} , where radiative emission contributes most significantly to the dark current, we see a clear decrease in dark current with angle restriction, as in figure 2a.

To quantify this we fit the dark current, J_0 , over the high voltage 0.6 to 1.1 V region, to the double diode equation

$$J_0 = J_{01} \left(e^{\frac{q[V - J_{dark} R_s]}{kT}} - 1 \right) + J_{02} \left(e^{\frac{q[V - J_{dark} R_s]}{nkT}} - 1 \right) \quad (5.2)$$

where J_{01} is the high voltage dark current component, J_{02} is the low voltage component, R_s is the series resistance, and n is the diode ideality factor [77, 78]. For both the control and angle restriction curves, the fit is excellent over several orders of magnitude. The fit deviates somewhat at very low currents, which we attribute to shunt resistance and has been previously observed in similar cells [39]. As figure 2b shows, J_{02} , R_s , and n are unchanged with angle restriction and n is very close to two, indicating that the double diode model is valid [77, 78]. In contrast, the J_{01} term, which has the same voltage dependence as radiative recombination, shows a 12% decrease with angle restriction, well beyond the error of the fit. Thus, by simply changing the optic above the cell to an angle restrictor, we observe a definite reduc-

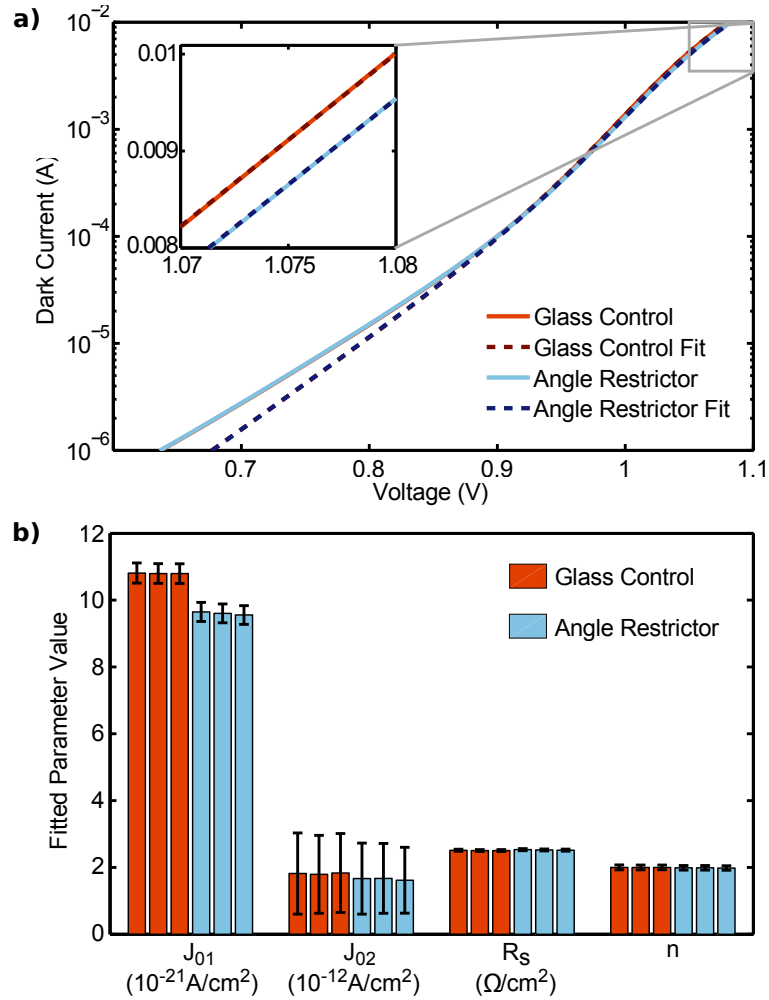


Figure 5.3. a) Representative dark current curves and double diode fits for both the angle restrictor and control cases. Inset: a clear reduction in dark current is evident near V_{oc} for the angle restrictor case. b) Double diode fitted parameter results with each bar representing one of three trials on the same 15.7% ERE cell for both the angle restrictor and fused silica control. The error bars represent 95% confidence intervals derived from the fit. Consistent with reduced radiative loss, J_{01} shows a marked decrease with angle restriction while all other parameters remain unchanged.

tion in the dark current. Specifically, the reduction occurs in the high voltage dark current component attributable to radiative loss, indicating that angle restriction is enhancing photon recycling within the cell.

5.4 Voltage Enhancements Under Illumination

In addition to a reduction in dark current, we also expect a direct V_{oc} enhancement under illumination. Furthermore, this voltage enhancement should be larger for cells with higher ERE, as more photons are available to be recycled via angle restriction. We therefore measured light current-voltage curves for a set of four cells with differing back reflector and material quality leading to significant variations in ERE across the cells, as determined from the J_{sc} and V_{oc} characteristics under the control optic. (See SI for further model details.) Owing to a reflecting band in the optical coupler around 550 nm, we limited the spectrum in this proof-of-concept experiment to wavelengths longer than 605 nm. (As in Section 4.8, this reflecting band can be eliminated with a rugate filter optical design, but for the initial coupler we did not pursue these structures as they are more difficult to fabricate [65, 66].) As shown in Figure 5.4, when we directly compare the control and angle restrictor on the same cell, current losses of 3.5% to 5.3% are observed with angle restriction, consistent with the measured normal incidence reflectivity of the angle restrictor. Without a change in the dark current, a reduction in J_{sc} would normally produce a corresponding reduction in V_{oc} , as in equation (1). However, V_{oc} increases of up to 2.5 mV are observed under angle restriction for the highest ERE cells, as dark current reduction is the dominant effect. Thus, angle restriction increases cell voltage without any change in the illumination, despite a reduction in J_{sc} . Furthermore, as we expect for photon recycling, the voltage change tracks the cell ERE.

Fortunately, these current losses are not intrinsic, and result from the simplicity of our initial angle restrictor design, as illustrated in Section 4.8 [65, 66]. To isolate the photon recycling effect, we adjust the solar simulator to equalize the currents between the control and angle restrictor, as in figure 3b. Once J_{sc} values are matched for the

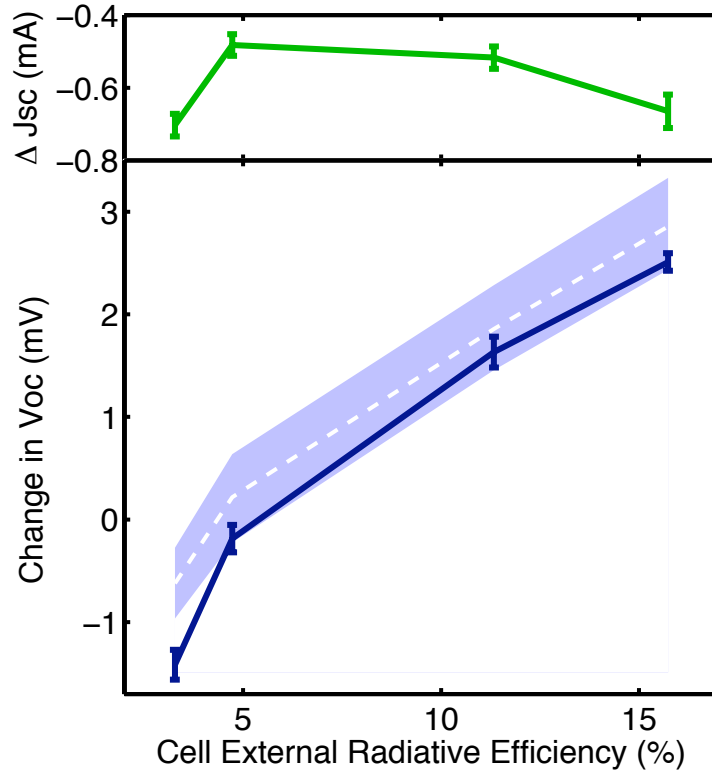


Figure 5.4. Measured changes in open-circuit voltage (dark blue line) and short-circuit current (green line) with angle restriction. The set of four cells is plotted as a function of external radiative efficiency (ERE) determined from J_{sc} and V_{oc} under the control optic. Variations in ERE occur between cells owing to differences in back reflectors and material quality. The error bars are calculated from standard deviation of five measured trials. The dotted white line indicates the expected voltage increase based on a modified detailed balance calculation. The light blue area shows the expected range of the model based on uncertainty in J_{sc} , V_{oc} , and temperature. As the solar simulator flux is held constant, there are current reductions (top) owing to normal incidence reflections in the multilayer angle restrictor, and thus V_{oc} increases are only seen in high ERE cells, where the reduction in J_0 outweighs the loss in J_{sc} , as in Equation 5.1.

angle restrictor and control, voltage increases ranging from 1.2 mV to 3.6 mV are seen for all cells, with higher ERE cells showing larger voltage increases. As the 15.7% ERE cell was also used for dark current measurements, we can compare the change in J_{01} to the observed change in V_{oc} . Since $V_{oc} = kT \ln(J_{sc}/J_0)$ and the J_{01} term is dominant near V_{oc} , the change in V_{oc} should be approximately $kT \ln(J_{01}/J'_{01})$, where J'_{01} indicates the average fitted value with the angle restrictor. Using this approach, we predict from the dark current fits that the V_{oc} increase should be 3.0 mV, which is reasonably consistent with the measured value of 3.6 mV for this cell. Thus, we observe a clear V_{oc} increase with angle restriction that is consistent with our dark current measurements, and an ERE trend that indicates enhanced photon recycling as the mechanism.

5.5 Modified Detailed Balance Model

We also develop a model that directly relates the voltage increase to the optical characteristics of the angle restrictor. While detailed balance is traditionally considered an idealized model, as shown in Chapter 3, we have developed a more realistic detailed balance model that includes the cell thickness, anti-reflective coating, back reflectors, and Auger and surface recombination. Including these non-radiative processes allows our model to be much more realistic than a traditional idealized detailed balance, where non-radiative losses are neglected. In addition, we simply input the measured short-circuit current, to avoid issues with the variability of the solar simulator lamp spectrum. Thus, the current at a given voltage, $J(V)$, in the modified model for these cells is expressed as:

$$J(V) = J_{sc} - \int_0^\infty [a(E) + n_r^2 a'(E)] \frac{2\pi q}{h^3 c^2} \frac{E^2}{e^{(E-qV)/kT} - 1} dE - qW(C_n n^2 p + C_p p^2 n) - 2qSp \quad (5.3)$$

where J_{sc} is the measured short-circuit current, and the rest of the terms give the various sources of loss from the cell. The first loss term includes radiative light emitted from the cell or absorbed in the back reflector, where $a(E)$ is the angle-

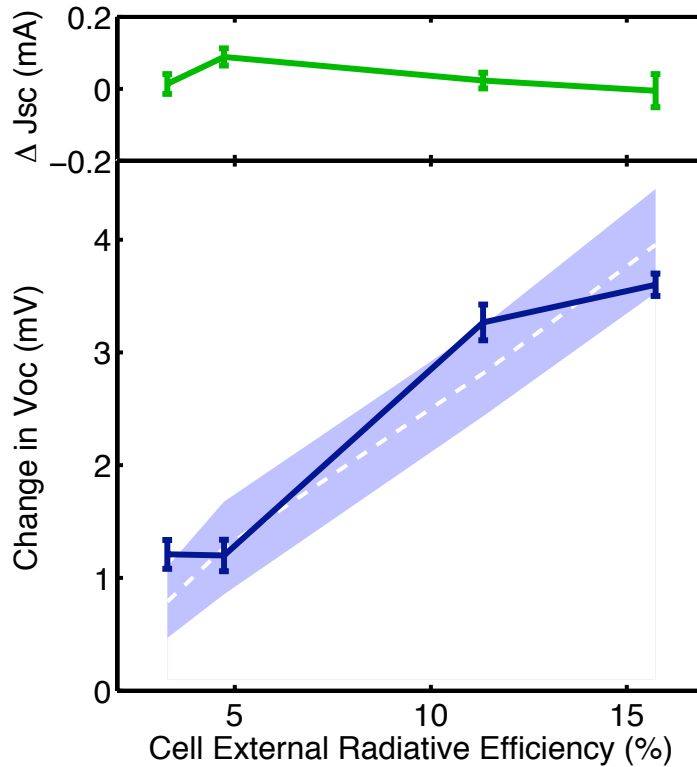


Figure 5.5. Measured changes in open-circuit voltage (dark blue line) and short-circuit current (green line) with angle restriction. The set of four cells is plotted as a function of external radiative efficiency (ERE) determined from J_{sc} and V_{oc} under the control optic. Variations in ERE occur between cells owing to differences in back reflectors and material quality. The error bars are calculated from standard deviation of five measured trials. The dotted white line indicates the expected voltage increase based on a modified detailed balance calculation. The light blue area shows the expected range of the model based on uncertainty in J_{sc} , V_{oc} , and temperature. The solar simulator was adjusted so that currents were equalized with the angle restrictor and control. With this current equalization, all cells see a voltage increase, with high ERE cells seeing a larger voltage increase.

averaged emissivity of the cell, and $a'(E)$ is the angle averaged absorption in the back reflector, with the expression given in Section 3.4.4. n_r is the index of refraction in GaAs, and is included because light only needs to be emitted into the cell, rather than air, to be absorbed in the back reflector [32, 40]. The next terms account for Auger recombination and surface recombination where C_n and C_p are the Auger coefficients [41], W is the cell thickness, and S is the surface recombination velocity, which we treat as an adjustable parameter. n and p , the electron and hole concentrations, are assumed to be constant across the cell and are determined from the assumed base doping, the neutrality condition, the cell voltage, and the law of mass action [43, 44].

To account for the optical environment, we calculate the angle-averaged emissivity for both the control and the angle restrictor based on measured reflectivity data as in figure 1d. Since there are multiple reflections in the glass substrate and the angular cutoff is gradual and varies with wavelength, we must use a slightly more complicated approach than that given in Section 3.4.4. To calculate the emissivity of the cell, $a(E)$, we use a multipass approach for light within the fused silica control or substrate. First, we find the fraction of light returned to the cell as a function of angle in the fused silica, ϕ , and the energy:

$$F_r(E, \phi) = \frac{R_t T_c}{1 - R_c R_t} \quad (5.4)$$

where R_t is the reflectivity at the top of the fused silica. For most angles, R_t is larger for the angle restrictor than the control, so more light will be returned and less light will ultimately escape the cell. Since light that is not recycled is ultimately emitted,

$$a(E, \theta) = (1 - F_r) a_c T_c n_g^2 \quad (5.5)$$

where we include the dual pass absorption of the cell, a_c , the transmissivity of the cell surface, and the fact that emission occurs into fused silica, with refractive index, n_g , rather than into air. Note that if the fused silica had an ideal AR coating, F_r would be zero and the emissivity would simply be a function of the cell absorption and surface reflectivity, as we expect. Finally, we average the above expression over the angles in fused silica to find $a(E)$. Note that we could also do this calculation

considering the angles in air rather than fused silica. While the result is the same with appropriate accounting of total internal reflection, we present the equations for fused silica as it is straightforward to generalize when accounting for light lost from the sides, as discussed below.

When considering the side loss, as in the next section, our simple multipass expression for F_r is insufficient, as it neglects the cell edges. Therefore, we move to a ray-tracing model, where we incorporate the cell edges, cell mount, measurement stage, and the substrate geometry, as detailed in Section 5.8. In this ray tracing model, we place a source and receiver on the cell area, and find the fraction of rays returned to the cell as a function of wavelength and angle to determine F_r . We then proceed with the standard evaluation of $a(E)$ as above. Thus, for Figure 5.7, we simply include a separate set of ray trace derived $a(E)$ values for each optical setup.

Once $a(E)$ is evaluated for each optical case, we use the measured J_{sc} and V_{oc} values for the gold-edged control glass case to fit a surface recombination velocity (SRV) that describes the cell performance. With this SRV value, we can determine the cell ERE, by simply taking the ratio of radiatively emitted light to other sources of loss. Then, we use the fitted SRV value along with the measured J_{sc} value and $a(E)$ determined for the optical environment to predict the cell V_{oc} with that optical environment, as in figures 5.4, 5.4, and 5.7. Finally, the observed temperature fluctuations of 0.1 °C and uncertainty estimates for J_{sc} and V_{oc} are used to determine the range of the prediction, as shown in the figures. These calculations agree quite well with the experimental results, indicating that the reduction in emissivity with angle restriction and the resulting photon recycling enhancement fully explain the observed differences in V_{oc} .

5.6 Variable Angle Restrictor Coupling

Lastly, we perform a series of experiments where we gradually increase the photon recycling and V_{oc} by coupling the angle restrictor more closely to the cell. As shown in Figure 5.7, we begin by placing a large, uncoated fused silica cylinder above the cell

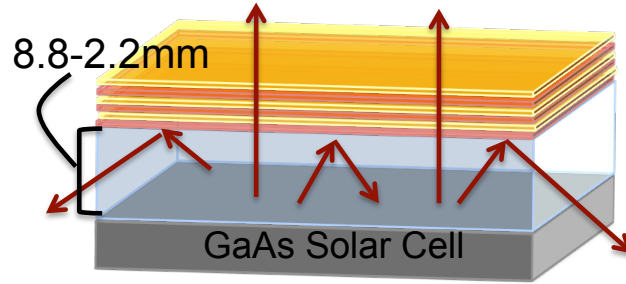


Figure 5.6. With uncoated sides, emitted light will escape from the sides, reducing the photon recycling effect. With a thicker spacer, more light will escape from the sides, further reducing the photon recycling effect.

which allows light to escape unimpeded from both the sides and top of the cylinder. In essence, this fused silica spacer facilitates the outcoupling of light emitted from the solar cell to free space, similar to the glass sphere often used with light-emitting diodes. As before, index matching fluid is used at the fused silica-GaAs cell interface. Then, the angle restrictor is placed on a series of fused silica spacers with non-reflecting, uncoated sides that allow light to escape, as shown in Figure 5.6, with index matching fluid between the spacer and the angle restrictor substrate. As the height of the spacer is reduced, less light escapes through the transparent sides of the spacers and more light is recycled back to the cell by the dielectric angle restrictor. Finally, we use an angle restrictor with reflecting sides to prevent light escape from the sides of the fused silica substrate and maximize the photon recycling. As Figure 5.7 illustrates, more closely coupling the angle restrictor to the solar cell increases the observed V_{oc} , demonstrating that more effective angle restriction leads to enhanced photon recycling and V_{oc} . We also find close agreement between the experiment and realistic detailed balance calculations, indicating that the coupling of the angle restrictor explains the observed changes in V_{oc} .

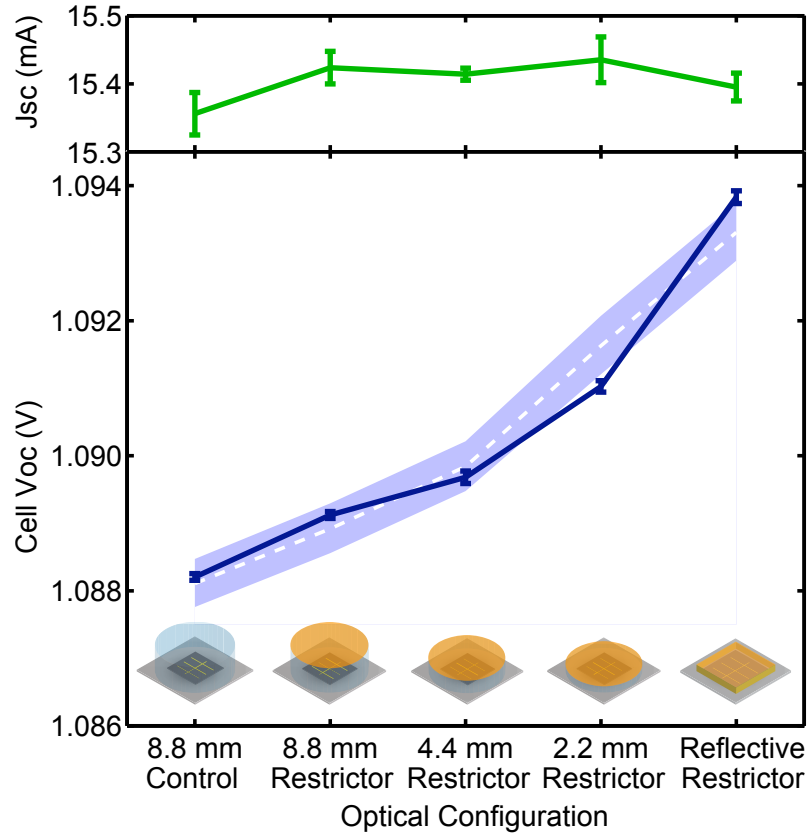


Figure 5.7. Measured open-circuit voltage (dark blue line) and short-circuit current (green line) as angle restriction is increased by coupling the angle restrictor more closely to the 15.7% ERE cell. The x-axis labels indicate the height of the fused silica spacer below the dielectric angle restrictor, or bare fused silica control, as on the far left. For all but the rightmost optical configuration, the sides of the fused silica spacers are uncoated so emitted light may escape. Thus, a taller spacer allows more light to escape from the sides, reducing photon recycling to the 1 cm^2 cell. In the rightmost configuration, the sides of the fused silica substrate are coated with a reflector to avoid side loss. Error bars are calculated from the standard deviation of five measured trials. The dotted white line indicates the expected V_{oc} based on a modified detailed balance calculation and the light blue area shows the range of the prediction. The solar simulator was adjusted to equalize the currents across the various optical configurations.

5.7 Bandgap Raising and Angle Restriction Effects

For a cell with suitably high ERE, placing an omnidirectionally reflecting structure on the cell to completely block emitted light can lead to an effective “photonic” increase in the cell bandgap [74, 79]. While we intentionally designed our angle restricting structure to not block normal incidence light above the cell bandgap, the angle restrictor as-deposited had an approximately 25 nm blue shift in the normal incidence transmission cut-off. Thus, some of the voltage increase observed may be due to this band-gap raising effect rather than a pure angle restriction effect. To quantify this, we calculated the expected voltage increase for the highest ERE cell for both the as-deposited angle restrictor and the angle restrictor as it was originally designed, using the calculated reflectivity values. For the designed angle restrictor, we predict a current-normalized V_{oc} increase of 3.3 mV, as opposed to the 4.0 mV prediction for the measured reflectivity values. Thus, angle restriction is clearly the dominant effect. In addition, we modeled the effect of an ideal bandgap-raising reflector for cells of similar ERE to those used in these experiments. We found that V_{oc} actually decreased with the bandgap-raising reflector, as the losses in J_{sc} from the reflector were not offset by the reduction dark current with enhanced photon recycling. While the departures from the original design have some impact on the voltage increase we observed, bandgap raising alone could not produce the V_{oc} effect we observed in cells of this radiative quality, and angle restriction is the primary effect.

5.8 Materials and Methods

5.8.1 Cell Contacting and Characterization

High efficiency 1 cm² GaAs solar cells were provided by Alta Devices. To eliminate variability associated with probe based contacting, permanent silver ribbon (E. Jordan Brooks Solar) based contacts were installed on the cells using a silver epoxy

(Epotek H20F) with a surrounding dielectric epoxy to prevent shorting (Creative Materials 119-48). Photoluminescence (PL) spectra were taken at room temperature in a Zeiss Axio Observer inverted microscope with a 10x objective with illumination from a 630nm pulsed diode laser. The photoluminescence emission was spectrally resolved with a Roper Scientific CCD (Model 7346-0001) and a Princeton Instruments Acton SP2150 monochromator. The PL curves shown in Figure 5.2c and d weight the raw photoluminescence spectra with external quantum efficiency data provided by Alta Devices to eliminate sub-band defect mediated photoluminescence, which cannot be usefully recycled.

5.8.2 Optical Coupler Fabrication and Characterization

The angle restricting dielectric multilayer was designed and modeled with a transfer matrix method approach using the OpenFilters program [80]. The dielectric multilayer design was deposited on 2.2 mm thick fused silica substrates by Reynard Corp., who also provided refractive index information for their materials. The angle dependent reflectivity spectra were taken in a home-built integrating sphere setup utilizing a Fianium white light laser source with a monochromator. In order to measure the dielectric coated interface most directly, the measurements were taken from air. Owing to errors in the measurement, a few data points gave reflectivity values slightly greater than one. These points were set to one and the reflections on the back surface of the substrate were subtracted. To subtract the back surface reflections, a multipass approach was utilized, with reflections at the back surface of the fused silica determined from the Fresnel equations and the refractive index of fused silica. The measured reflectivity in the integrating sphere includes both the reflectivity of the dielectric on the first pass and the reflection of transmitted light from the back surface that is subsequently transmitted through the dielectric. Accounting for the multiple passes of transmitted light in the fused silica we find that the measured reflectivity, R_m , is:

$$R_m = R_d + \frac{T_d^2 R_b}{1 - R_b R_d} \quad (5.6)$$

where R_d and T_d are the reflection and transmission at the dielectric coated surface, and R_b is the reflection at fused silica-air interface at the back of the substrate. All reflection and transmission values refer to a given angle in air and the corresponding angle in fused silica, as determined by Snell's law. Re-arranging the above expression gives:

$$R_d = \frac{R_m - R_b}{1 - 2R_b + R_m R_b} \quad (5.7)$$

The resulting values of R_d are plotted in figure 1d and were used to calculate the angle restrictor emissivity for the detailed balance model. For the purposes of calculating emissivity, reciprocity allows us to equate R_d at a given angle in air with R_d at the corresponding angle in fused silica, as determined from Snell's law. Fused silica substrates for use as controls were obtained from Reynard Corp. To eliminate side loss, the substrates were scribed and broken to approximately 13 mm x 12 mm. Side reflectors consisting of an 2 nm Cr adhesion layer and 400 nm of gold were deposited in an AJA magnetron sputtering system under DC power.

5.8.3 Current-Voltage Measurements

Angle restrictor and control optics were coupled to the cells using Cargille Fused Silica Index Matching Liquid (50350) at the interface of the cell and the fused silica substrate. Dark current measurements were performed using a Keithley 238 high current source measure unit. Dark current fits assumed a temperature of 24 °C, and were performed in Matlab using least-squares curve fitting with the Levenberg-Marquardt algorithm.

All light IV measurements were performed under an ABET Technologies solar simulator with 1° angular spread calibrated to 100 mW/cm². The spectrum was filtered using a Chroma Technologies (ET605LP) long pass filter with a 605 nm cutoff. The cells were measured on a temperature controlled stage, and were allowed to cool for three minutes between each IV sweep. However, peak stage temperature variations of approximately 0.1 °C were observed. IV sweeps were taken with a Keithley 2440 5A SourceMeter. Five sweeps were taken for each configuration with the standard

deviation defining the error in V_{oc} and J_{sc} . For the solar simulator adjustments necessary to equalize the currents, the precise concentrations are not known, but currents to the solar simulator lamp were increased by 1-1.5 A depending on the cell, over a base value of 48.1 A.

5.8.4 Implementation of the Modified Detailed Balance Model

To model the voltage increase, we used the modified detailed balance model implemented in Matlab. Based on observed peak stage temperatures, all simulations assumed 299 K. To determine ERE for each cell, we fit the surface recombination velocity to match the measured V_{oc} under the control optic with the measured J_{sc} under the control. Taking the ratio of the radiative emission relative to all recombination at V_{oc} gave the ERE value reported in figure 3. Fitted SRV values ranged from 591 to 2410 cm/sec. Differences in back reflector type and material quality, as reflected in the effective SRV values, led to the variations in ERE across the four cells in figure 3. The experiments in figures 2 and 4 utilized the 15.7% ERE cell reported in figure 3. Auger recombination assumed 1×10^{17} n-type GaAs [43]. Back reflector losses were calculated using the Fresnel equations. To find the emissivity at each wavelength and angle, we used a multipass model assuming the light bounces between the cell and the fused silica/air top interface with no other sources of loss. The reflectivity of the top surface with the angle restrictor was derived from integrating sphere measurements as described above, and was calculated using the Fresnel equations for the fused silica control. The reflectivity at the cell surface was found using the transfer matrix method, assuming a 20 nm AlInP window layer, based on NREL designs [43]. For the AR coated (15.7% ERE) cell, we assumed 50 nm of TiO_2 and 100 nm of SiO_2 above the window layer.

To determine the range for the detailed balance model calculation, we used the uncertainties in the J_{sc} and V_{oc} , as determined from the multiple trials to determine a range for these values in the control case. We then used values for J_{sc} and V_{oc} at the edges of the range to determine maximum and minimum fitted SRV values. Finally, we used these SRV values along with the observed temperature uncertainty

and uncertainty in the measured J_{sc} to determine a range of values for the predicted V_{oc} under angle restriction.

5.8.5 Gradual Coupling Measurements

For the gradual coupling experiments in figure 4, cylinders of the varying heights were assembled from 25 mm diameter fused silica substrates of 2.2 mm and 6 mm thickness, provided by Reynard corporation. Cargille fused silica index matching liquid was used between the cell-fused silica and fused silica-fused silica interfaces. All substrates had ground glass edges, and currents were equalized across all configurations by adjusting the solar simulator as necessary. While the precise solar concentrations of this adjustment are not known, the currents to the simulator lamp ranged from 47.0 A for the control case to 48.7 A for the tallest restrictor structure. The modified detailed balance model was used with a ray trace to find the emissivity. The ray trace was performed in LightTools, a commercial software. The ground glass edges were assumed to be Lambertian surfaces, with reflectivity based on total internal reflection and Fresnel losses. For the ray trace, the reflectivity spectrum of the material surrounding the cell was measured in the Zeiss Axio Observer setup utilized for PL measurements, but with a lamp source. The gold edge reflectivity was modeled for the ray trace using the transfer matrix method assuming a 2 nm Cr layer with an optically thick Au layer.

5.9 Conclusions

We have performed a series of experiments that clearly demonstrate enhanced photon recycling and resulting V_{oc} increases of up to 3.6 mV via angle restriction with a narrowband dielectric multilayer angle restrictor. Dark current measurements show a 12% decrease in the radiative component of the dark current consistent with the observed voltage enhancement. In addition, measurements of the voltage increase on several cells illustrate that cells closer to the radiative limit show larger voltage enhancements, as we expect for photon recycling. These measurements also show

good agreement with calculations based on the measured reflectivity of the angle restrictor. Finally, we have shown that more closely coupling the angle restrictor to the cell leads to predictable increases in voltage for several configurations, emphasizing that this voltage increase is due to a purely optical photon recycling effect.

Thus, we have demonstrated as a proof of concept that angle restriction with a narrowband dielectric multilayer leads to enhanced photon recycling and a corresponding voltage increase in high quality GaAs cells. The narrowband angle restrictor approach has significant advantages in admitting diffuse light and in the relatively simple design that can replace an existing anti-reflective coating. While the voltage enhancements shown here are relatively small, the effect becomes much larger as ERE increases and cells approach the radiative limit. High ERE cells are already being developed for III-V materials to achieve the highest possible voltage and efficiency, and these cells are ideal candidates for a broader applicability of the angle restriction approach [76]. As further improvements are made in III-V cell technology and other materials reach the high ERE regime, this approach holds promise for significantly increasing cell efficiencies in a flat plate geometry.

Chapter 6

Angle Restriction in Silicon Solar Cells

6.1 Motivation

Silicon solar cells are currently the dominant terrestrial photovoltaic technology due to material abundance and relatively low-cost manufacturing processes. While the world record had remained static for more than a decade, recently a new performance record of 25.6% was achieved [81, 82]. One alternative approach to increasing efficiency is restricting the angles at which light may escape the cells with an external optic. As discussed in Chapter 3, restricting the escape angle reduces the escape cone inside the cell, leading to increased light trapping and increased photon recycling in materials with high radiative recombination [7, 30, 32]. While recent experiments in GaAs, as in Chapter 5 and other work, have focused on the photon recycling effect, in low radiative efficiency materials, like silicon, the light trapping effect is more significant, as in Figure 6.1 [75, 83]. Limiting the light escape angle significantly enhances the light trapping effect already utilized in current silicon cells, allowing for excellent light absorption in a very thin cell and reducing materials usage. Enhanced light trapping also gives a small increase in current, as light near the band edge is more completely absorbed [7, 30]. Finally, the thinner cell leads to voltage enhancement, as the losses due to bulk recombination processes like Auger and Shockley-Read-Hall (SRH) are reduced.

While the limiting efficiencies for silicon cells under angle restriction were initially calculated by Campbell and Green in 1986 [30], we re-calculate these efficiencies to include models for free carrier absorption and band gap narrowing as well as improved Auger parameterizations that have been developed in the intervening decades. This

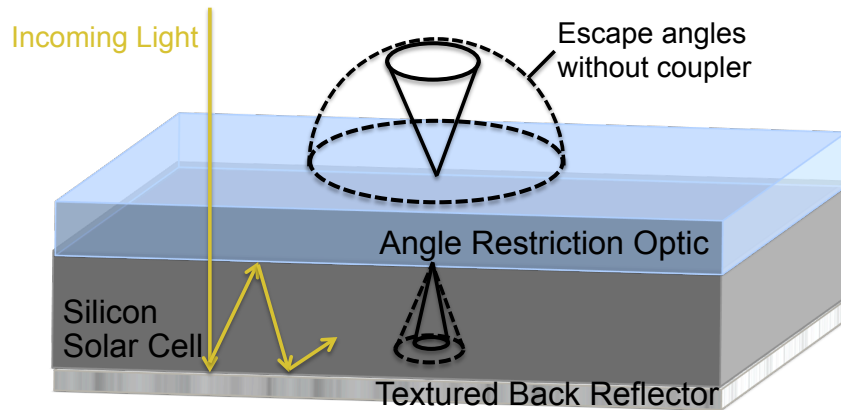


Figure 6.1. In silicon, radiative efficiency is low due to the indirect bandgap and significant Auger recombination loss. Thus, light trapping, rather than photon recycling, is the major effect of angle restriction. With angle restriction, the escape cone within the cell is reduced (solid line) relative to the escape cone without angle restriction (dotted line). This enhances the path length for a light-trapping geometry, where incoming light is scattered, as by the textured back reflector shown here. As absorption is weak owing to the indirect band gap, essentially all current production silicon cells have a light trapping geometry to allow for good absorption in a cell of reasonable thickness.

leads to an estimate of 3% absolute efficiency increase in an Auger-limited cell under angle restriction [30, 84, 85]. We further develop this model to include surface and bulk SRH recombination, allowing us to simulate the performance of current champion amorphous silicon heterojunction with intrinsic thin layer (HIT) and homojunction interdigitated back contact (IBC) solar cells [6, 58, 86]. We find that HIT cells perform significantly better under angle restriction, with efficiency gains of approximately 1% absolute achievable with moderate angle restriction in parallel with a 50% reduction in cell thickness. We also find that excellent surface recombination and back reflectivity are crucial for significant efficiency improvements with angle restriction, as we expect with thinner cells, while bulk lifetimes have little effect.

When we limit the escape angles for a cell, the angles at which light can enter are limited as well, as a consequence of optical reciprocity. As discussed in Chapter 3, limiting the escape angle will therefore likely necessitate some degree of solar tracking, in order to keep the direct solar flux within the angles at which light can enter the cell over the course of the day. While this system is similar to a concentrator system in that tracking is required, the angle restricting optics considered here are quite thin (several mm or thinner) and may be easily incorporated into a traditional flat plate module. However, depending on the degree of angle restriction and the accuracy of the tracking system, this approach may also be used in concert with low to moderate external concentration, for additional efficiency enhancements of 1% absolute or more for 10x concentration. In either a flat plate or low to moderate concentration geometry, the heating and series resistance effects which degrade performance at high concentrations are mitigated [33, 34, 35]. Thus, this approach allows for many of the efficiency benefits of concentration while avoiding the deleterious effects seen at high concentrations and allowing for a wider range of module geometries.

There has been significant previous work on various designs for achieving angle restriction in silicon cells [30, 59, 65, 66, 87]. However, most of these have focused on increasing short circuit currents in very thin idealized cells. In contrast, we explore the effects of both narrowband rugate structures and broadband ray optical structures for angle restriction over a wide range of cell thicknesses and for both ideal and realistic

cells. We find that broadband ray optical angle restrictors allow for much larger efficiency enhancements than their narrowband counterparts, owing to the narrower angle restriction provided over a broader range of wavelengths. With a broadband structure, efficiency increases up to 0.8% absolute for HIT cells and 1.5% absolute for idealized cells are predicted for optimal cell thicknesses.

6.2 Effects of Angle Restriction in Ideal and Realistic Silicon Cells

6.2.1 Angle Restriction in Ideal Cells

To find the limiting efficiency under angle restriction in ideal cells, we use a detailed balance approach with the recent Auger parameterization determined by Richter et al. [29, 84, 85]. This parameterization is more sophisticated than the simple parameterization used for GaAs, and accounts for Coloumb interactions of the carriers. However, we replace the derived radiative recombination coefficient given in this parameterization with a black-body type emission term, as in Chapter 3, which allows us to include angle restriction. Neglecting series and shunt resistance effects, the net current at a given voltage, $J(V)$, is:

$$J(V) = J_L(V) - R_A(n, p, n_0, p_0)W - \int_0^\infty \left[\int_{\Omega_c} a(E) \cos(\theta) d\Omega + \pi n_r^2 a'(E) \right] \frac{2}{h^3 c^2} \frac{E^2}{e^{(E-qV)/kT} - 1} dE \quad (6.1)$$

where J_L is the light generated current, which has a slight voltage dependence owing to free carrier absorption, as parameterized by Rüdiger [88]. The quantity $R_A(n, p, n_0, p_0)$ gives the Auger recombination as a function of the electron and hole concentrations under illumination and at equilibrium, respectively [84]. As before, this term scales with the cell thickness, W , as Auger recombination is a bulk process. The electron and hole concentrations are determined from the assumed doping, the neutrality condition, the cell voltage, and the law of mass action [44, 85]. Bandgap narrowing

occurs due to impurity bands from highly doped regions and from modification of the band structure owing to the carrier plasma, and also affects the carrier populations within the cell [89, 90]. Unlike GaAs, well-developed models for bandgap narrowing exist for silicon, and we include band gap narrowing effects using Schenk's model with intrinsic carrier concentration, $n_{i,0}$ of 8.28×10^9 [85, 89, 91, 92]. However, the effect of bandgap narrowing is quite small for silicon at one-sun illuminations [85]. The right-most term gives the losses due to radiative emission within the cell, with Ω_c the solid angle of light emission, $a(E)$ the band to band absorptivity, and $a'(E)$ the parasitic absorptivity, which in the ideal case is due solely to free carrier absorption. This term is multiplied by the square of the silicon refractive index n_r , to account for the relative concentration of light within the solar cell [29, 32, 36, 40, 93]. Finally, E gives the energy of the emitted light, h is Planck's constant, c the speed of light, q the electron charge, and kT the temperature (25° C) in units of energy.

The light generated current, J_L is given by:

$$J_L = C_f \int_0^\infty a(E) S(E) dE \quad (6.2)$$

where $S(E)$ is the AM 1.5 direct solar spectrum and C_f is the external concentration factor. For the moment, we assume no external concentration, so $C_f = 1$. The band to band absorptivity, $a(E)$, is:

$$a(E) = \frac{\alpha(E)}{\alpha(E) + \alpha'(E) + \frac{\sin^2(\theta)}{4n_r^2 W}} \quad (6.3)$$

where $\alpha(E)$ and $\alpha'(E)$ are the band to band and parasitic absorption coefficients, respectively, and θ is the maximum angle of light emission. [7, 30, 93]. Thus, as the escape angle, θ , is reduced, $a(E)$ increases as the escape cone for light within the solar cell narrows. Finally, the parasitic absorptivity, $a'(E)$, which is due solely to free carriers in the ideal case, is:

$$a'(E) = 4W \alpha'(E) \frac{\alpha(E)}{\alpha(E) + \alpha'(E) + \frac{\sin^2(\theta)}{4n_r^2 W}} \quad (6.4)$$

where the amount of parasitic absorption is proportional to both the band-to-band emission and the parasitic absorption coefficient [32, 40, 46].

Using these relations, we calculate the maximum power under angle restriction using the AM 1.5 direct spectrum, as well as short circuit current, J_{sc} , and open circuit voltage, V_{oc} . Efficiency is calculated with respect to the direct spectrum and 90 W cm^{-2} incoming power. Figure 6.2 shows the results for an n-type, lowly-doped ($1 \times 10^{11} \text{ cm}^{-3}$) silicon substrate with unity reflection from the back surface and neglecting all recombination other than Auger. Highest efficiency, up to a 3% absolute increase, is achieved for thinner cells with narrow angle restriction. While thinner cells show improved performance, we limit the minimum cell thickness to $3 \mu\text{m}$, as the absorptivity expressions above apply only in the ray optical limit. Additionally, thinner cells are not optimal when more realistic losses are considered, as in the next section. Most of the enhancement at a given thickness is due to increased light trapping as seen as increased J_{sc} (Figure 6.2b) with much less impact from V_{oc} (Figure 6.2c). In fact, we achieve more than 2 mA improvement in J_{sc} over a $200 \mu\text{m}$ thick non-angle restricted cell, owing to the very long absorption lengths in silicon. The V_{oc} is mostly improved by thinning the cell as Auger recombination is reduced.

From the efficiency, Figure 6.2a, we can discern the optimum thickness at a given angle restriction. With no angle restriction (90°), the optimal thickness is approximately $119 \mu\text{m}$ (in good agreement with previous calculations under AM 1.5 global [84]). As the angle restriction narrows, the optimal thickness decreases as well. While narrow angle restriction and very thin cells lead to the highest efficiencies, for cells thicker than about $50 \mu\text{m}$, angle restriction narrower than 10° has very little impact on cell performance, suggesting that improvement for wafer-based silicon cells may be achievable with lower cost technologies.

6.2.2 Angle Restriction in Realistic Cells

While the limiting efficiency case is of theoretical interest, it is also important to consider the effects of angle restriction on current production-scale silicon solar cell technologies. To account for non-idealities, we include additional losses due to bulk

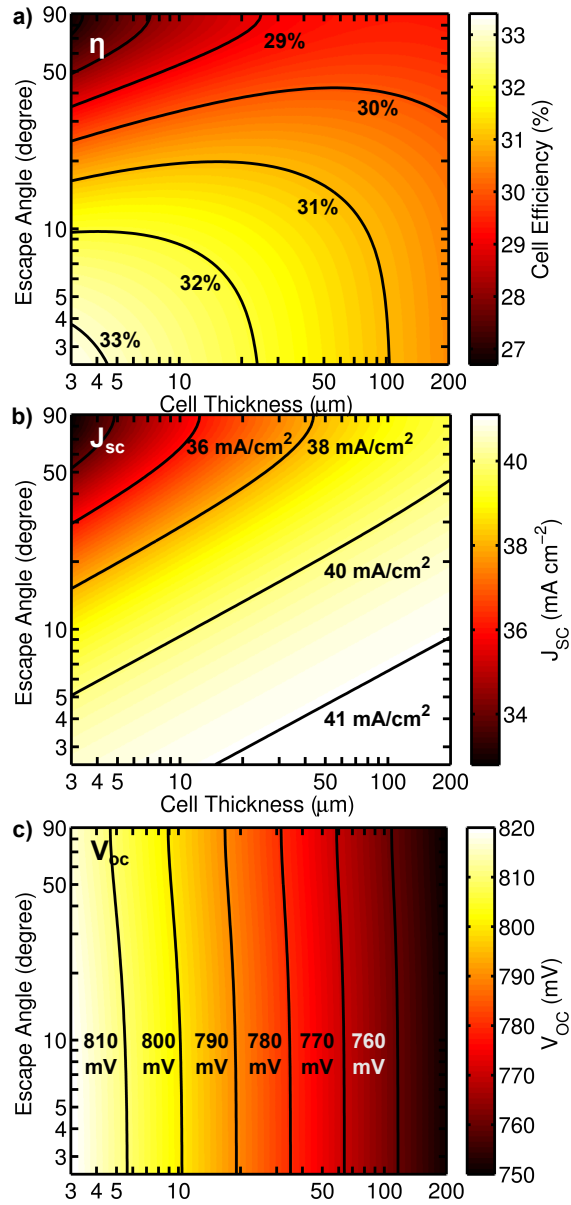


Figure 6.2. Efficiency η , short circuit current, J_{sc} , and open circuit voltage, V_{oc} , for an ideal, Auger-limited silicon solar cell. Narrow angle restriction and a very thin cell lead to the highest efficiencies. Increases in both J_{sc} and V_{oc} are observed.

SRH and surface recombination in Equation 6.1.

$$\begin{aligned}
J(V) = & J_L(V) - R_A(n, p, n_0, p_0)W \\
& - \int_0^\infty \left[\int_{\Omega_c} a(E) \cos(\theta) d\Omega + \pi n_r^2 a'(E) \right] \frac{2}{h^3 c^2} \frac{E^2}{e^{(E-qV)/kT} - 1} dE - J_{SRH} - J_{SRV}
\end{aligned} \tag{6.5}$$

where

$$J_{SRH} = qW \frac{np - n_{ieff}^2}{\tau_{SRH}p + \tau_{SRH}n} \tag{6.6}$$

$$J_{SRV} = 2q \frac{np - n_{ieff}^2}{p/S + n/S} \tag{6.7}$$

where τ_{SRH} is the bulk lifetime associated with SRH processes, and S is the surface recombination velocity (SRV) [42]. For both of these expressions, we assume a single SRV and SRH lifetime averaged over both carrier types, and, in the case of the SRV, both surfaces. (The factor of two in the surface recombination expression accounts for the top and bottom surfaces of the cell.) We also include non-ideal back reflectors, as part of the parasitic absorption, along with free carrier processes according to the following relation:

$$\alpha'(E) = \alpha_{FCA} + \frac{1 - R_b}{4W} \tag{6.8}$$

where $\alpha_{FCA}(E)$ is the absorption coefficient for free carrier absorption and R_b is the back reflectivity [46].

We estimate the SRV and SRH lifetimes for IBC and HIT cells by matching the V_{oc} of the modeled cell to experimental values for a given optimal cell thickness. While our model neglects series and shunt resistance, this should have little effect on V_{oc} , as series resistance largely impacts fill factor and in these high quality cells shunt resistance should be sufficient to avoid any significant effects on V_{oc} . Our estimates also rely on assumptions about cell doping, back reflectivity, and optimal thickness without angle restriction. For the HIT cell, we assume a 98% reflective back surface, as well as losses from 6 nm of amorphous silicon on the top surface of the cell and 9 nm on the bottom surface [94]. We then vary the SRH lifetime and SRV to fit the

reported champion HIT cell voltage (750 mV) with an optimal cell thickness of 100 microns, finding an SRV of 2.87 cm/sec and a SRH lifetime of 2.2 msec [6]. For the IBC cell, we use a similar procedure, but assume a 180 micron optimal cell thickness and a 95% back reflector to find an SRV of 11.64 cm/sec and a lifetime of 1.2 msec [58, 86]. Thus, using the reported cell voltages, we can estimate the surface and bulk recombination for each of these champion cells. Table 6.1 summarizes the full set of parameters for each of the cell models considered here.

Table 6.1. Cell Parameters for Ideal and Realistic Cell Models

	Ideal	HIT	IBC
Dopant Type	n	n	n
Dopant Density (cm ⁻³)	1x10 ¹¹	1.6x10 ¹⁵	1.6x10 ¹⁵
Back Reflectivity (%)	100	98	95
SRV (cm/sec)	0	2.87	11.64
SRH Lifetime (msec)	Infinite	2.2	1.2

To explore the sensitivity of our model to the optimal cell thickness assumption, we vary the optimal thickness, and determine a range of possible SRV and SRH lifetime values, as shown in the lower panels of figures 6.4 and 6.3. For this range of possible SRV values we then calculate the efficiency with no angle restriction (90°) and with an emission angle of 10°. We also calculate the optimal thickness with no angle restriction and with 10° emission angle, as shown in the top panels of figures 6.4 and 6.3. The optimal thickness at 90° is slightly different than that plotted on the x-axis. This is because we use AM 1.5 G for the SRV and lifetime estimation, as the experimental open-circuit voltages we match to were taken under the global spectrum. In contrast, the efficiencies and optimal thicknesses plotted in figures 1a and 2a use an AM 1.5 D spectrum, as angle restriction utilizes only the direct portion of the solar spectrum.

For the IBC cell, shown in Figure 6.3, increasing the optimal thickness leads to longer SRH lifetimes and increased SRV values, as we expect. However, for very

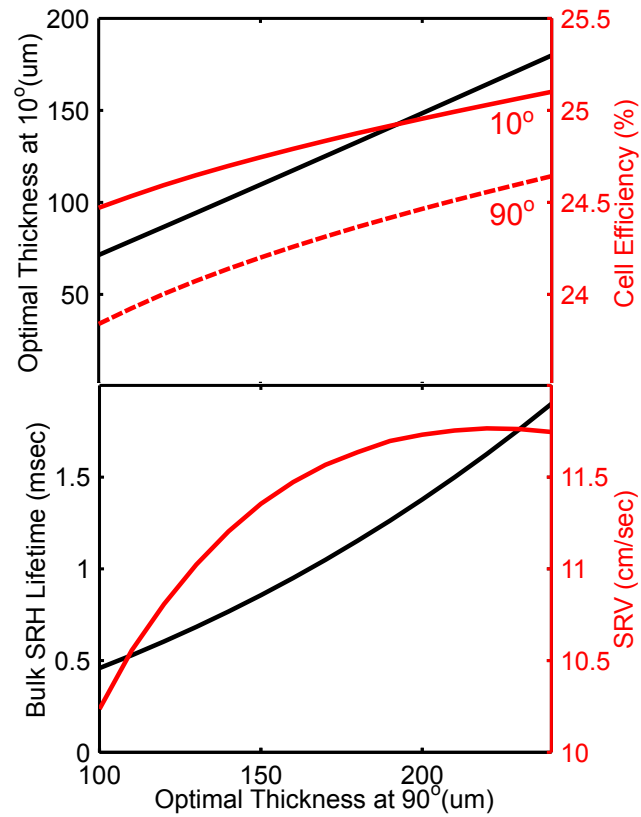


Figure 6.3. As the optimal thickness is varied for the IBC cell, the estimated values for SRV and SRH lifetime change, as plotted in the lower panel, to match the experimental V_{oc} of 721 mV. However, the efficiency increase with angle restriction is not very sensitive to these changes, and the proportional reduction in thickness is fairly constant.

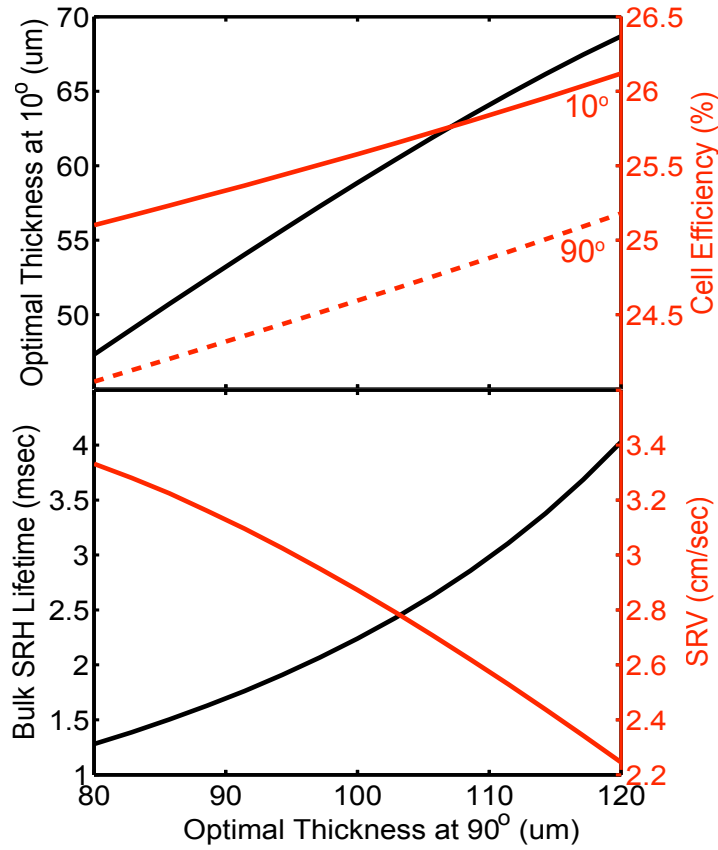


Figure 6.4. As the optimal thickness is varied for the HIT cell, the estimated values for SRV and SRH lifetime change, as plotted in the lower panel, to match the experimental V_{oc} of 750 mV. However, the efficiency increase with angle restriction is not very sensitive to these changes, and the proportional reduction in thickness is fairly constant.

thick cells the SRV begins to plateau and even decrease, as all recombination must be reduced to achieve the experimental V_{oc} in a very thick cell with its increased bulk recombination. Similarly, for the HIT cell, achieving the very high experimental V_{oc} in a thicker cell requires reductions in both surface and SRH recombination, while in a thinner cell increased levels of both types of recombination may be tolerated. For both the HIT and IBC cells, the proportional reduction in cell thickness and the efficiency increase with angle restriction are not very sensitive to changes in the SRV and SRH lifetime estimates as the optimal thickness without angle restriction is varied. However, the values of efficiency and optimal thickness at 10° emission do vary more significantly.

Using the SRV and SRH lifetime values estimated above, we calculated the impact of angle restriction on both HIT and IBC cells. As is shown in Figure 6.5, there is a clear contrast in the effects of angle restriction for the HIT and IBC cells, despite similar reported efficiencies for these two cells [58]. In fact, for the IBC cell, only about 0.5% absolute efficiency improvement is expected relative to a non-angle restricted cell. However, narrow angle restriction is not required to achieve these relatively meagre benefits, with an escape angle of about 40° sufficient for a 100 micron thick cell. For the HIT cell, in contrast, efficiency increases of up to 1% absolute are achievable with angle restriction. To achieve this, cells in the 40-90 micron thickness range with angle restriction to at least 10° are required. Thus, while significant materials savings are possible if desired, cells need not be thinned appreciably relative to current technology to realize significantly improved efficiencies with angle restriction [6].

For these two high efficiency current technologies, there is a significant difference in the impact of angle restriction, with HIT cells showing twice the benefit under angle restriction relative to IBC cells. To understand this more clearly, we need only consider the J_{sc} and V_{oc} values plotted in Figure 6.5. While the shape of the J_{sc} contours are similar, currents are maintained better in thinner cells for the HIT structure, owing to the improved back reflector. Additionally, while HIT cells show consistent V_{oc} improvements down to 10 micron thick cells for the HIT structure, V_{oc} improvements plateau in the IBC structure, as the higher SRV begins to limit the

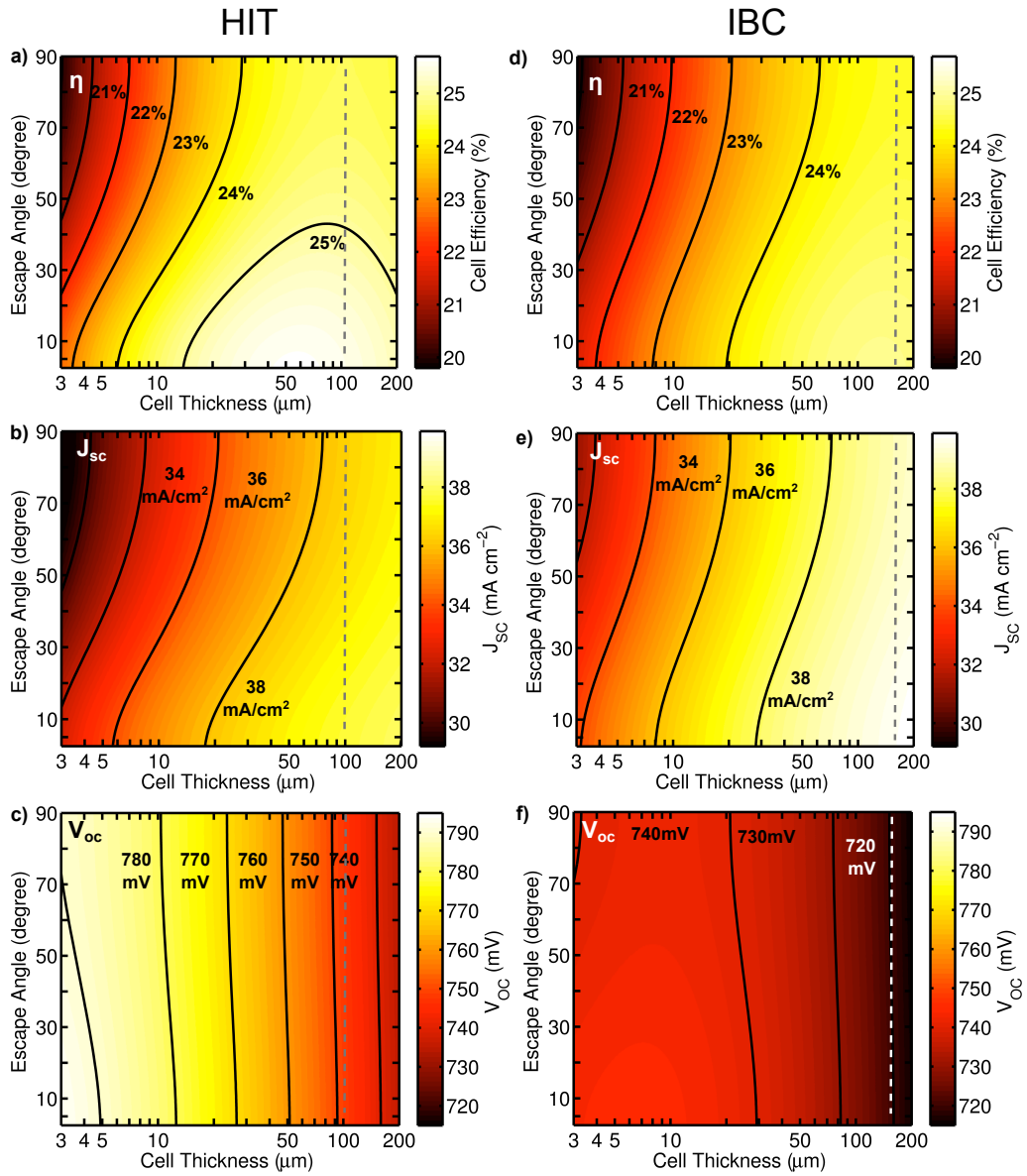


Figure 6.5. Efficiency, η , short circuit current, J_{sc} , and open circuit voltage, V_{oc} , for cells with surface recombination and SRH lifetimes that approximate HIT (left) and IBC (right) type silicon cells. HIT cells show much greater efficiency improvements with angle restriction.

voltage. These larger V_{oc} enhancements offset any reductions in current for thinner HIT cells, so much thinner cells are optimal under angle restriction for HIT cells, and much larger efficiency improvements are seen.

While we have argued above that the improved SRV and back reflectivity are crucial to the improved performance under angle restriction seen with the HIT cell, the HIT cell also has a longer SRH lifetime. To explore the relative importance of these factors, in Figure 6.6 we plot the efficiency and efficiency increase under angle restriction as a function of back reflectivity, and also examine the effect of a factor of two improvement in either SRV or SRH lifetime. While improvements in either back reflectivity, SRV, or lifetime lead to an overall efficiency enhancement, only improved SRV and back reflectivity lead to greater efficiency increase with angle restriction. In fact, the efficiency enhancements with angle restriction are slightly lower with an improved bulk lifetime. This is consistent with efficiency increases due to enhanced light trapping allowing for a thinner cell, and a resulting decrease in bulk recombination processes, like SRH. The significantly larger optimal cell thicknesses shown in Figure 6.6 for longer lifetimes support this explanation. Thus, the results in Figure 6.6 suggest that with angle restriction, there is less benefit to utilizing high lifetime silicon, particularly for a cell with an excellent back reflector. These results also emphasize the importance of an excellent back reflector and low SRV for achieving maximal benefits with angle restriction in a thin cell.

6.2.3 Angle Restriction with External Concentration

So far, we have considered the effect of escape angle restriction for enhanced light trapping in the solar cell. Next we consider how external concentration can further enhance the performance of a Si device when used in combination with the same angle restriction geometry. An external concentrator will also limit the optical acceptance angle: light is collected from a limited range of incoming angles and concentrated onto a smaller area with a broader angular spread. At the thermodynamic limit [60] of concentration by the factor C_f , the relationship between the angular spread of

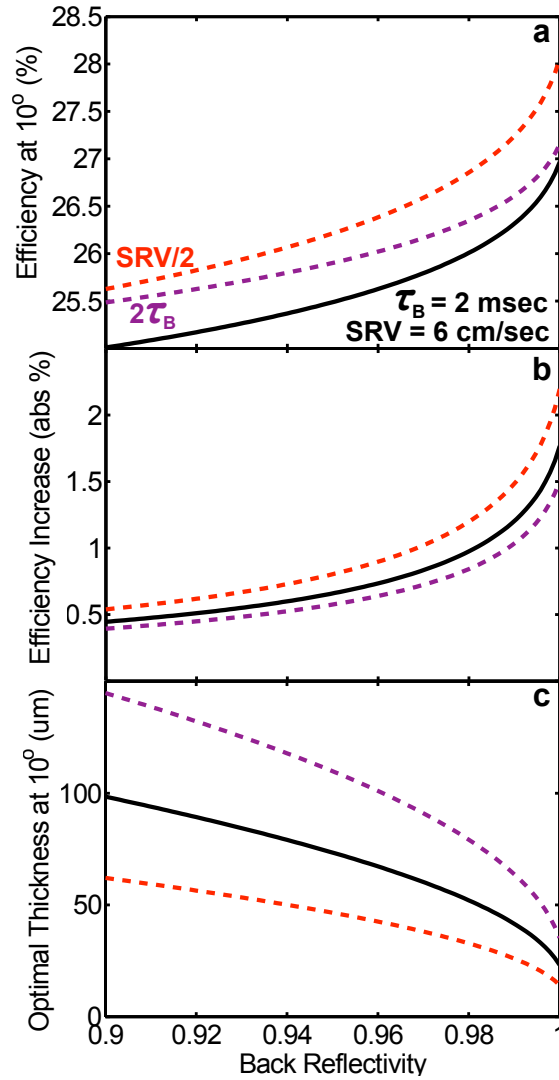


Figure 6.6. a) Improved SRV, SRH lifetime, and back reflectivity all lead to increases in efficiency with 10° escape angle. b) Efficiency increases relative to non-angle restricted cell are greater with improved SRV and back reflectivity, and slightly smaller with improved SRH lifetime. c) Improved SRH lifetime leads to much larger optimal cell thicknesses, while improved SRV and back reflectivity lead to reduced optimal cell thicknesses.

incoming light, θ_{in} , and the angular spread of light after concentration, θ_{out} is

$$\sin(\theta_{out}) = \sqrt{C_f} \sin(\theta_{in}). \quad (6.9)$$

For this calculation, we assume this spread is $0.267^\circ \pm 2.5^\circ$ in accordance with the measurement conditions of the direct solar spectrum [95]. However, this is fairly conservative relative to the acceptance angles of current high concentration systems. Due to reciprocity, the angular spread of light after concentration sets the narrowest possible solar cell escape angle where all incoming light is collected.

In Figures 4a and 4b, we plot the efficiency and optimal thickness respectively of a HIT-type cell with angle restriction combined with various levels of concentration, neglecting heating or increased series resistance losses in the cells. Efficiency can be improved up to 0.8% absolute by narrowing the escape angle to 20° . For higher concentration ratios, the optimal thickness increases due to the increased carrier density and increased recombination rates. Conversely and similar to the case with no concentration, we see that the optimal thickness decreases with increased angle restriction. Thus for a given concentration, higher efficiency could be reached with a thinner device.

As mentioned previously, an angle restriction scheme would likely require tracking to ensure the sun's image falls within the allowed angles for light to enter the cell. A typical low-precision tracking system for solar is on the order of 5° ; performance limitations for such a tracker are also indicated in Figure 4. With such a tracking system, using 50x concentration in combination with moderate angle restriction of 40° a HIT device could achieve greater than 30% efficiency (with respect to the direct spectrum) with a $100 \mu\text{m}$ thick substrate. To achieve similar efficiencies without angle restriction approximately 100x external concentration and a significantly thicker cell would be required. Thus, using angle restriction in concert with external concentration allows for higher efficiencies with lower external concentrations, reducing the requirements for heat-sinking and allows for a greater choice of module geometry. The tradeoff between cell thickness, concentration, and angle restriction offers a variety of options

for attaining higher efficiency with a variety of module geometries.

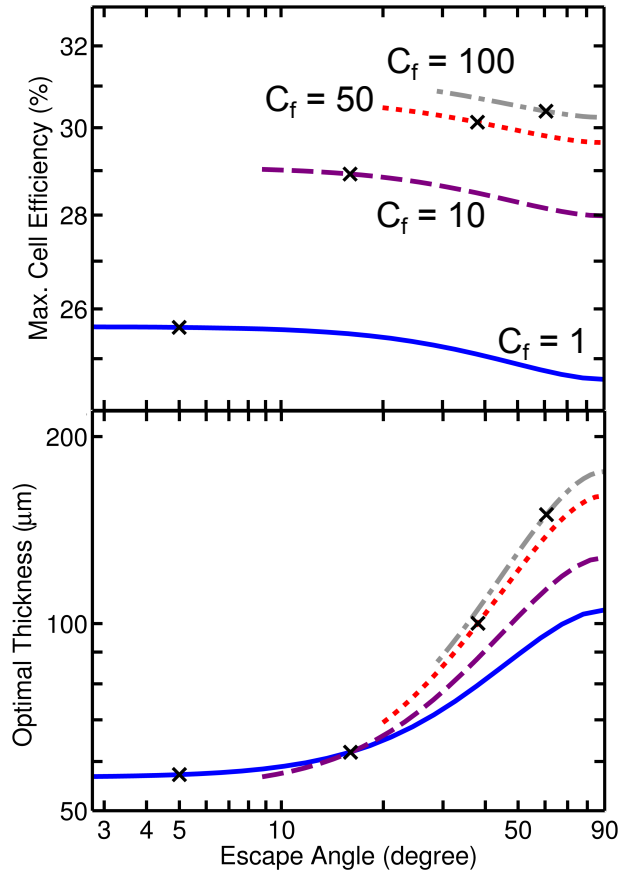


Figure 6.7. Impact of external concentration applied to an escape angle restricted HIT type cell for various concentrations, assuming ideal tracking precision. Numbers for 5° tracking precision indicated by 'x'. Maximum cell efficiency (a) is achieved for an optimal thickness (b) of substrate.

6.3 Angle Restrictor Designs

In all the preceding calculations, we have assumed a lossless angle restrictor which only allows light to enter and leave the cell within the cone described by the escape angle. Furthermore, we assumed that the escape angle cutoff was the same across all wavelengths. In this section, we explore the performance of various structures that limit the escape angle either over all wavelengths or over a narrow range of wavelengths

near the silicon band edge. There has been significant prior work focused on designing such structures for both crystalline and amorphous silicon cells [30, 59, 65, 66, 87]. However, most of this work has focused on structures that limit the escape angle only over a narrow wavelength range for very thin, idealized solar cells or has been more conceptual. Here we consider both narrowband and broadband angle restrictors and analyze the effects of these structures on the performance of both the idealized and HIT silicon cells over a range of thicknesses.

6.3.1 Narrowband Angle Restrictor

To achieve narrowband angle restriction, we consider a multilayer structure with alternating high and low refractive index. Similar to the narrowband structure presented in Chapter 4, the angle restriction effect may be understood by considering the Bragg condition (Equation 4.13) for reflection from a periodic stack, though the design presented here is more sophisticated.

As shown in figure 6.8 for shorter wavelengths, maximum reflection occurs away from normal incidence, giving the angle restriction effect we desire. To avoid undesirable second-order reflecting bands, and other normal incidence reflections, we utilize a rugate structure, with a gradual variation of refractive index [65-68]. As in Chapter 4, we assume the cell is placed under glass ($n=1.5$), as is common in deployed systems, and that gradual index variation between 1.5 and 2.5 may be achieved with $\text{SiO}_2/\text{TiO}_2$ codeposition [70-72]. We also assume that the rugate structure is deposited in place of an anti-reflective (AR) coating between the glass and the solar cell. As a comparison case, we consider a quintic-type graded index AR coating deposited at the same interface and with the same range of refractive index [69]. Figure 6.8a illustrates the refractive index profiles of the optimized rugate angle restricting structure and the graded index AR coat comparison. As shown in figures 6.8b,c, the calculated normal incidence transmission is very similar for both the angle restrictor and AR comparison. Thus, the rugate structure avoids additional optical losses. As the angle restriction is narrowband, the angle restrictor will capture diffuse light over most of the solar spectrum, and may also allow for simpler, cheaper tracking.

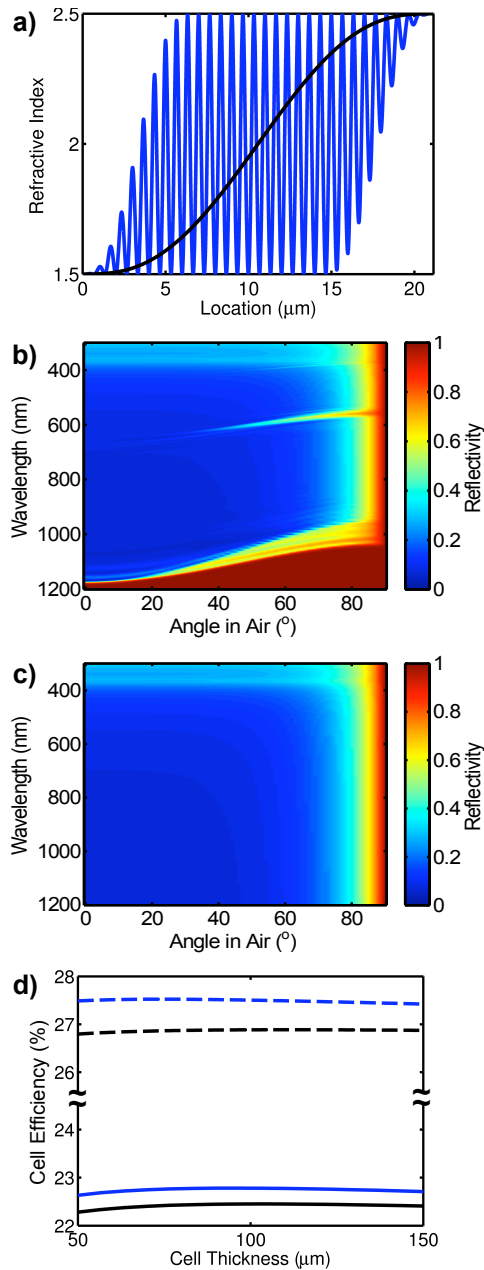


Figure 6.8. a) Refractive index profile for rugate angle restrictor design (blue), and quintic graded index AR coat comparison (black). b,c) Calculated reflectivity for rugate angle restrictor design (b) and graded index AR (c). The transfer matrix method was used to calculate the performance of the thin film structures, and reflections off the overlying glass ($n=1.5$) were included with a multipass model. d) Efficiency with rugate angle restrictor (blue) and graded index AR (black) for the HIT cell model (solid), and the ideal cell model (dashed).

However, this also means that significant enhanced light trapping will only occur for light at wavelengths longer than 1 micron, which limits the possibilities for thinning the cell. The angle restriction also has a fairly wide escape angle over much of the spectral range, which is not ideal for maximizing the enhancement.

Due to the relatively wide escape angles and narrow wavelength range, we expect that the rugate angle restrictor will not give the full performance benefits predicted in figures 6.2 and 6.5. To calculate the performance under angle restriction, we replace the factors of $\sin^2(\theta)$ in the absorptivity expressions and the angular integral in Equation 6.1 with a wavelength dependent angle-averaged transmission, determined from the reflectivity results in Figure 6.8b,c. As shown in Figure 6.8d, for an ideal cell, the optimal thickness decreases from 110 microns to 80 microns with a 0.6 percentage point efficiency increase. For the HIT cell, the effect is even smaller, with only a 0.3 percentage point efficiency increase and 7 micron reduction in the optimal cell thickness. Thus, while the narrowband design allows for the utilization of diffuse light, the efficiency gains are rather small, and a significant reduction in cell thickness is not preferable.

6.3.2 Broadband Angle Restrictor

The results above suggest that narrower angle restriction over a broader wavelength range will be required to achieve the substantial efficiency increases suggested by figures 6.2 and 6.5. To explore this further, we examined a broadband ray optical angle restrictor, which utilizes an array of hexagonal solid compound parabolic concentrator (CPC) structures [60]. In this design, similar to that proposed by Green, the CPC structure utilizes total internal reflection to direct light near normal incidence to the output aperture where it enters the cell [30, 59]. Except for the area under the output apertures of the CPCs, the top surface of the cell is coated with a metallic reflector, such that light inside the cell can only escape through the output apertures and light trapping is enhanced.

As in the previous section, we assume that the top of the CPC array is in optical contact with a covering glass of index 1.5. We also assume that the solid CPC struc-

tures have index 1.5, that the reflector above the cell has 98% reflectivity, and that the graded index AR coat presented in Figure 6.8 is deposited at the output apertures of the CPC structures between the index 1.5 CPC material and the underlying silicon cell. Ray trace results, as in Figure 6.9b, show that quite narrow angle restriction, to about 10° , is possible, with normal incidence transmission similar to the AR coat alone. We note that achieving this narrow angle restriction requires including a conical section at the bottom of the CPC to narrow the range of output angles from the structure and avoid skew rays, increasing the height of the structure. While this structure is ray optical and may be fabricated at any scale significantly larger than the wavelengths of interest, ideally the spacing between the reflector holes would be no larger than the carrier diffusion length, so the CPC structure would be no taller than several millimeters.

Similar to the previous section, we incorporate the ray trace results into detailed balance model. However, in this case we must also include the losses in the non-ideal back reflector above the solar cell. Thus, the escape value used in place of $\sin^2(\theta)$, P_{esc} , is now expressed as:

$$P_{esc} = \bar{T} + A_r(1 - R_t)n_g^2 \quad (6.10)$$

where \bar{T} is the angle-averaged transmission determined from the ray trace, A_r is the fraction of the top surface area covered by the reflector, and R_t is the reflectivity of the top reflector, assumed to be 98% in this case. n_g is the refractive index of the material between the solar cell and the reflector, which is assumed to be 1.5 in this case.

Using the above expression, we calculated the efficiency as a function of thickness for both the ideal and HIT cell models for the two different CPC designs presented in Figure 6.9b. As shown in Figure 6.9c, with the broadband angle restriction and smaller escape angles, the efficiency improvements suggested by figures 6.2 and 6.5 are, in fact, realizable. For the HIT structure, 0.8% absolute efficiency improvement is found, with the optimal thickness decreasing substantially to 62 microns. In line with Figure 6.5a, much of the efficiency benefit (0.6% absolute) is achieved with the

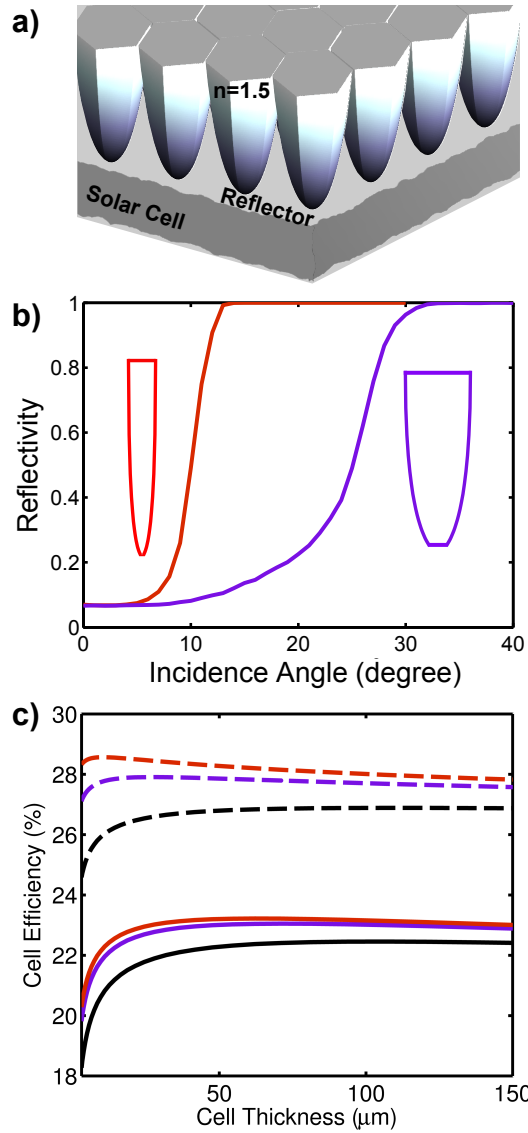


Figure 6.9. a) CPC based ray optical angle restrictor schematic. b) Ray trace results at 1 micron wavelength and scale CPC profiles for CPC array with 5° acceptance angle and 57° output angle (red), and 15° acceptance angle and 83° output angle (purple) [60]. The CPC output aperture for the 15° CPC is six times wider than for the 5° CPC. Note that the effective angle restriction is less narrow than the design acceptance angle, owing to refraction at the air-glass interface as light enters the CPC. c) Efficiency results for both CPC arrays and graded index AR (black) with the HIT cell model (solid) and the ideal cell model (dashed).

larger escape angle CPC structure, which would also allow for cheaper, less accurate tracking and more utilization of diffuse light. For the ideal cell, the effects are even larger, with optimal thicknesses as low as ten microns and efficiency increases of 1.5 absolute percent. Thus, significant efficiency benefits are possible with realistic angle-restricting optical structures.

6.4 Conclusions

Restricting the light escape angle with an external optic has significant potential to further improve the performance of silicon solar cells by improving light trapping, allowing for thinner, more efficient cells in a flat plate geometry. Using a detailed balance approach, we have re-evaluated the ideal, Auger-limited case and found that efficiency increases of up to 3% absolute may be expected with very thin cells and narrow angle restriction. Considering the performance characteristics of champion HIT and IBC cells, we have found that the efficiency benefits of angle restriction are much more significant in the HIT case, with 1% absolute efficiency increases expected with cells that are half as thick as current cells. Unlike the idealized case, for current technologies we find that limiting the escape angle more narrowly than 10° has minimal additional benefit. Low surface recombination velocity and excellent back reflectivity, as found in HIT cells, are crucial to achieving the maximal efficiency benefits with angle restriction. Angle restriction may also be used in concert with low to moderate external concentration, for addition efficiency enhancements. Finally, we have considered both narrowband rugate-based and broadband ray-optical angle restrictor designs. With the rugate structure, escape angles are wide, and efficiency benefits are modest for both the HIT and ideal structures, with small changes in the optical thickness. In contrast, broadband angle restrictors can achieve quite narrow escape angles, and show significant efficiency benefits and reductions in the optimal cell thickness. Thus, we envision broadband angle restriction with a CPC-based ray optical structure used in either a flat plate geometry or with low to moderate external concentration for silicon solar cells. With current HIT cell technology, this approach

allows for cells that are half as thick as current cells, with significant efficiency improvements.

Chapter 7

Light-Trapping Filtered Concentrator For Spectral Splitting

7.1 Motivation

While the previous few chapters have focused on efficiency improvements with angle restriction, photon entropy increase due to isotropic emission is not the largest source of loss in ideal solar cells. In fact, while 10% absolute efficiency increase may be gained with full photon entropy management in an ideal cell, thermalization and lack of absorption losses owing to a single bandgap, as discussed in Chapter 1, are a much larger source of loss [31, 96]. One way to address this loss is to utilize additional bandgaps, so that higher energy photons are absorbed by larger bandgap materials and lower energy photons are absorbed by lower bandgap materials. In this way, higher energy photons are absorbed by materials more closely matched to their bandgaps, reducing thermalization loss. Additionally, lower energy photons that would not have been absorbed by an optimal single bandgap may now be absorbed and converted by the lower bandgap materials. Thus, 46% absolute efficiency gain may be realized with infinite bandgaps, as opposed to the conventional single bandgap [96].

Multijunction solar cells are the most advanced and heavily studied approach to incorporating additional bandgaps in a solar cell. In these cells, several materials with different band gaps are grown in a monolithic structure, with tunnel junctions to allow current to flow between each junction [97-100]. The materials are arranged vertically from highest to lowest band gap, with the highest bandgap cell grown on top, so that

the highest energy photons are absorbed in materials with the largest bandgap. Lower energy photons that are not absorbed continue through the monolithic stack until they are absorbed in lower energy bandgaps. While very high efficiencies have been recorded with multijunction cells, including a recent record exceeding 44% efficiency, there are some fundamental issues limiting the efficiencies that can be achieved with this technology [58].

The monolithic nature of a multijunction solar cell limits its efficiency because of both a lattice-matching and current-matching constraint. To obtain the highest quality photovoltaic material with a minimum of defects, the different materials in the structure must have similar lattice constants. With this lattice-matching constraint, the limited choice of materials may lead to non-optimal band gap selection or the material quality may suffer, either of which reduces the efficiency [101]. Additionally, as all the cells are connected in series, the current produced by each cell in the monolithic stack must match, or power will be lost. This affects the choice of bandgaps, leading to bandgap selections that would be non-optimal in the independently connected case, where the currents need not match [97, 98]. Furthermore, over the course of the day and the year the spectrum will shift so that the cell is no longer current matched, leading to significant losses in annual power production [102, 103]. Both the current matching and lattice matching constraint limit the number of bandgaps, with the current world record for triple junction cells [58]. This in turn limits ultimate efficiency and power that may be achieved with multijunctions. Thus, if very high efficiencies are desired, new approaches must be considered. While there has been significant work on hot carrier, intermediate band, and other “third generation” technologies in an attempt to provide alternatives to multijunctions, many fundamental materials science issues must be overcome before these can be practically realized with high efficiency [96, 104-107].

Spectrum splitting represents an alternative approach to either multijunction or third generation technologies. In this approach external optics are used to split the light into different spectral bands. These different spectral bands are then directed onto solar cells with bandgaps tuned to convert each spectral band with maximal

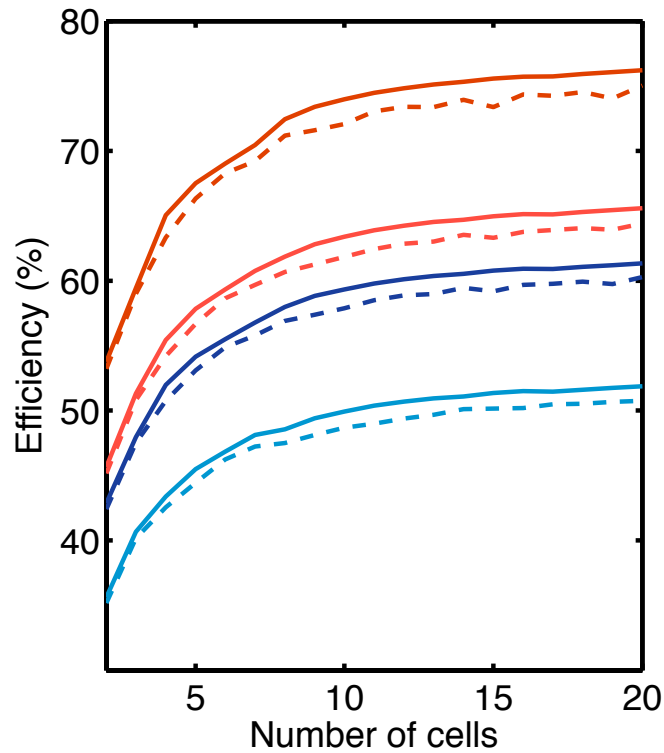


Figure 7.1. As the number of junctions in the system is increased efficiency increases significantly, as losses due to thermalization or lack of absorption are reduced. Detailed balance efficiency calculations for optimized bandgaps show a clear plateau around 6-10 junctions. Independently connected cells (solid line), as in spectral splitting, give higher efficiencies than series connected cells (dashed lines), as in multijunctions. Furthermore, higher concentrations lead to higher efficiencies, as discussed in Chapter 3. Darker shades indicate 500x concentration; lighter shades indicate 1x concentration. Dark and light blue lines indicate realistic cell performance, with 90% of the ideal current absorbed and collected, and reductions in voltage due to non-radiative loss, with external radiative efficiency (ERE) of 1% [73]. Dark and light red lines indicate the ideal case with 100% of ideal current collected with ERE of 100%. Figure courtesy of Emily Warmann [103].

efficiency [108]. As each cell may be independently electrically connected, there is no current matching constraint, allowing for a more optimal choice of bandgaps, and higher efficiency. This gives approximately 1-2% absolute efficiency increase, as shown in Figure 7.1, as well as up to 20% enhancements in annual power production [103]. In addition, many more bandgaps may be utilized with higher material quality, as each cell can be grown on its own lattice matched substrate. As in Figure 7.1, there are significant possible efficiency gains in incorporating more than three junctions, as in current world monolithic multijunctions. However, the spectrum splitting optics must split the spectrum accurately and with low loss to access these gains. As with concentrator multijunction cells, we anticipate that the spectrum splitting module will include significant concentration and will require high accuracy, two-axis solar tracking.

The goal of this project was to design optical structures that could achieve significantly higher efficiencies than the best concentrating multijunction modules, where the world record efficiency currently stands at 36% [58]. As shown in Figure 7.1, the benefits to additional junctions plateau in the 6-10 junction range, and there are significant efficiency benefits to high concentration (500x or greater). In fact, with independent connection and 500x concentration, efficiencies over 50% may be achieved for six junctions, with high quality, but realistic, cell performance. Many optical approaches to spectrum splitting are possible, including holographic, parallel-piped, prism, or grating based approaches [108]. Here we analyze a light trapping filtered concentrator approach, where incident light is trapped within a dielectric slab and passes into the appropriate cell through filters. While the light trapping filtered concentrator approach to spectrum splitting was initially suggested by Goetzberger and is similar in operation to the cavity concentrator proposed by Ortabasi, here we focus on optimizing the design for very high efficiencies [109, 110]. Considering the results in Figure 7.1, it is clear that 6-10 junctions, along with fairly high concentrations, should be included in our final design to achieve efficiencies significantly higher than the current module world record. Furthermore, while previous work has been largely conceptual, we propose an initial, optimized design of the spectrum splitting

submodule, including filter elements, that allows for high efficiencies.

7.2 The Light Trapping Filtered Concentrator

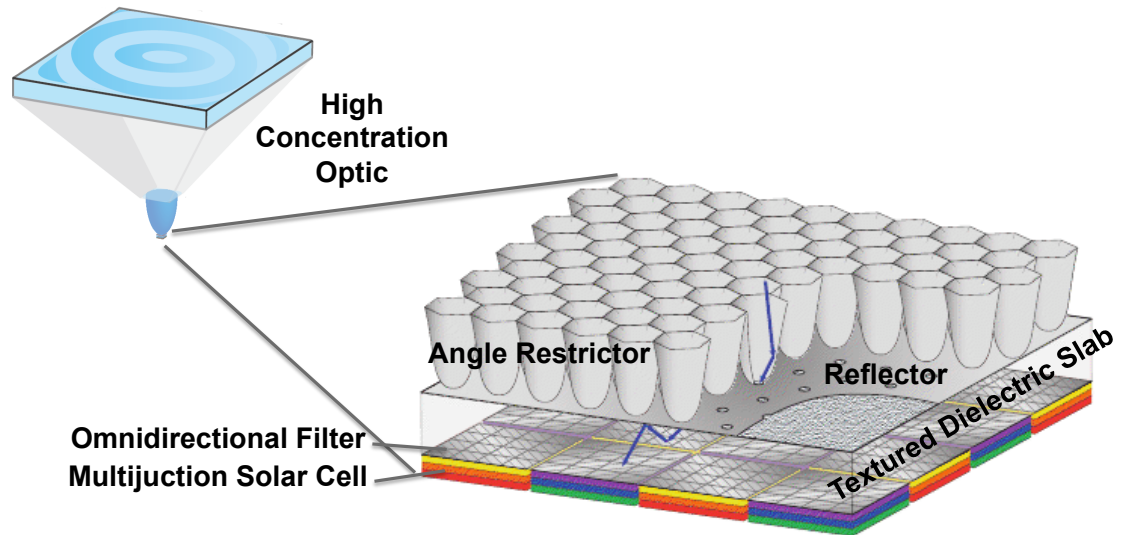


Figure 7.2. Schematic of the light-trapping filtered concentrator spectrum splitting module. We envision the splitting submodule being placed under a traditional high concentration optic. Light enters through the high concentration optic and the angle restrictor on top of the splitting submodule. Upon entering the dielectric textured slab, it is scattered, and trapped by total internal reflection in the slab and the reflector associated with the angle restrictor. As the light travels randomly through the slab, it encounters the various underlying subcells, which have omnidirectional filtering elements that only allow light in the correct spectral band to enter the cell. Figure courtesy of John Lloyd.

Figure 7.2 shows the basic design and operation of the light-trapping filtered concentrator. Light enters via a high concentration optic, allowing for the additional efficiency gains with concentration illustrated in Figure 7.1. Light then travels through the angle restrictor on top of the spectrum splitting submodule. While the high

concentration optic may be fairly standard, it must be designed so that the output angles of light fall within the acceptance angle of the spectrum splitting submodule. Upon entering the textured dielectric slab that lies beneath the angle restrictor, the light is scattered. It is then trapped within the slab by the reflector associated with the angle restrictor, and by total internal reflection at the surface of the dielectric slab. Thus, either a higher slab refractive index or a narrower acceptance angle for the angle restrictor lead to improved light trapping within the slab. Light trapped within the dielectric slab then encounters the subcells underlying the slab. Ideally, each subcell is filtered by an omnidirectional filter, which only allows light of the appropriate wavelengths to enter. Thus, light bounces around the slab until it encounters the appropriate subcell, passes through the filter element, and is absorbed. In this schematic, each subcell is a multijunction cell. As will be discussed in the next section, this allows us to achieve the larger number of bandgaps desired, while reducing loss from light escaping the slab.

7.3 Basic Design Considerations: The Multipass Model

7.3.1 The Thick Slab Assumption

To narrow the design space, we first developed a simple, multipass ray optical model for light propagation within the dielectric slab. We assume ideal filters and slab thickness comparable to the subcell width. According to Monte Carlo simulations, shown in Figure 7.3, a slab of at least this thickness maximizes the probability that light reflected from a filter at a given subcell will next impinge on the appropriate subcell. Conversely, if the slab is too thin, the light ray is likely to impinge on the same non-ideal subcell twice. Under the thick slab assumption, Monte Carlo simulations indicate that the probability for light to impinge on the correct subcell with each pass is f , the fraction of slab area covered by the correct subcell. Assuming all subcells are of the same size, f is $1/\text{subcell number}$. Thus, for idealized filters, a fraction

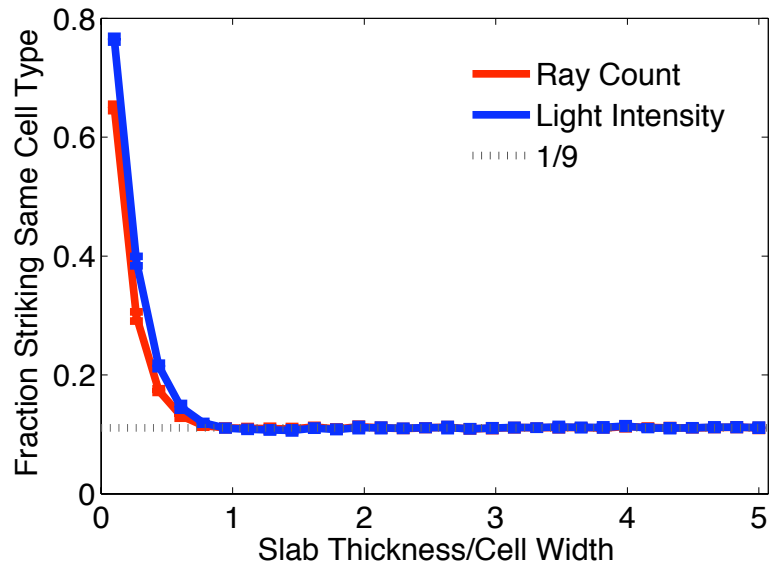


Figure 7.3. Based on ray geometry, the probability of returned light striking the same cell type twice was determined for a nine subcell geometry. A Monte-Carlo approach was used to determine the direction of the light when it was scattered at the top of the slab, assuming equal brightness in all directions. Once the slab thickness is similar to the subcell width, the light is fully randomized and the probability of returned light striking the same type of subcell twice is minimized.

of light f is absorbed on the first pass through the cell. Then, on the second pass, $(1 - f)(1 - p)f$ is absorbed, where p is the probability of escape at the top of the slab. Performing the summation for infinite passes, we find the overall fraction of light absorbed, or the optical efficiency, η_{opt} , is:

$$\eta_{opt} = \frac{f}{1 - (1 - f)(1 - p)} \quad (7.1)$$

The results of the multipass model are plotted in Figure 7.4, illustrating that a low escape probability combined with a small number of cells gives the highest optical efficiency.

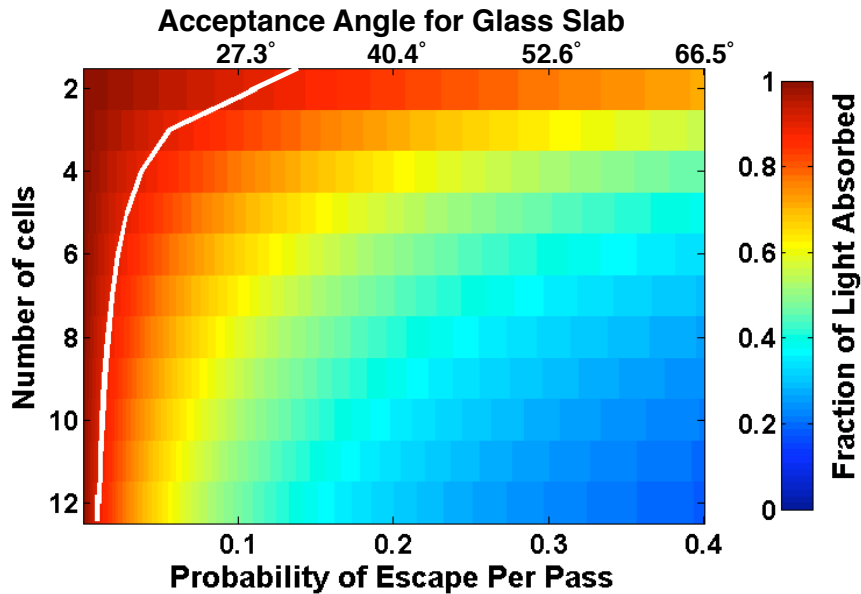


Figure 7.4. Optical efficiency as a function of the number of subcells and probability of slab escape. The white line indicates where optical efficiency is over 90%. The top axis shows the angle restrictor acceptance angle in a glass slab that corresponds to the probability of slab escape on the bottom axis.

Table 7.1. Sets of Subcells Optimized for AM 1.5D

	Overall Optimum	Limited Top Bandgap	Dual Junction Bottom Cell
	2.57 eV	2.20 eV	2.20 eV
Top Cell	2.23 eV	1.78 eV	1.78 eV
	1.99 eV	1.48 eV	1.48 eV
	1.63 eV	1.36 eV	1.37 eV
Middle Cell	1.36 eV	1.22 eV	1.23 eV
	1.12 eV	1.13 eV	1.15 eV
	0.93 eV	0.94 eV	0.93 eV
Bottom Cell	0.72 eV	0.73 eV	0.70 eV
	0.39 eV	0.52 eV	—
Efficiency	55.7%	54.1%	53.5%

The table above gives three sets of multijunction subcells optimized for AM 1.5 D, with current matching imposed within each subcell. While the overall optimum is ideal, the top bandgap is too high to be achieved with current high quality materials. We therefore limited the top band gap to 2.2 eV in the second column. It is also difficult to find current high quality materials with bandgaps as low as 0.52 eV. Therefore, we restricted the bottom cell to two bandgaps, which has only a small effect on the efficiency. The efficiency values assume ERE of 1% and 500 suns concentration.

7.3.2 Initial Subcell Optimization

As shown in Figure 7.4, to maintain a high optical efficiency in combination with a large number of bandgaps for optimal spectrum utilization, two to four multijunction subcells are optimal. For this initial design, we consider three underlying multijunction subcells, which have been optimized for AM 1.5 D. While further optimization will be performed to maximize performance under our optics, these bandgaps give a starting point for designing filter elements. As shown in Table 7.1, when we limit the bandgap based range based on materials considerations, we find a set of two triple junction cells and one dual junction. While current matching will be required within each of these multijunction subcells, this will have a smaller effect on efficiency and annualized energy production than if all eight junctions required current matching. This is because all the bandgaps within a given subcell address nearby portions of the solar spectrum, which tend to change together over the course of the day, as there is more red light near dawn and dusk and more blue light at midday.

7.3.3 Reducing Probability of Slab Escape: Design Tradeoffs

As in Figure 7.4, optical efficiency for the light trapping filtered concentrator is maximized when the probability of light escaping the slab is low. This escape probability can be reduced by mounting an angle-restricting device such as an array of compound parabolic concentrators (CPCs) on top of the slab. With such angle restrictors the slab can only receive light from within the acceptance angle of the CPCs, but light also only enters the slab through small holes at the bottom of each CPC. Since most of the slab is covered with a reflector, the light escape probability from the slab is reduced by a factor of $1/\sin^2(\theta)$, where θ is the acceptance angle of the angle restrictor, and we assume for the moment that the output angle of the CPC is 90° [60]. As we expect, the probability of escape is lowest for a high index slab and a slab with narrow angle restriction, as shown in Figure 7.5.

While the multipass model suggests maximizing the slab index of refraction and/or minimizing the acceptance angle of the CPCs to maximize optical efficiency, both

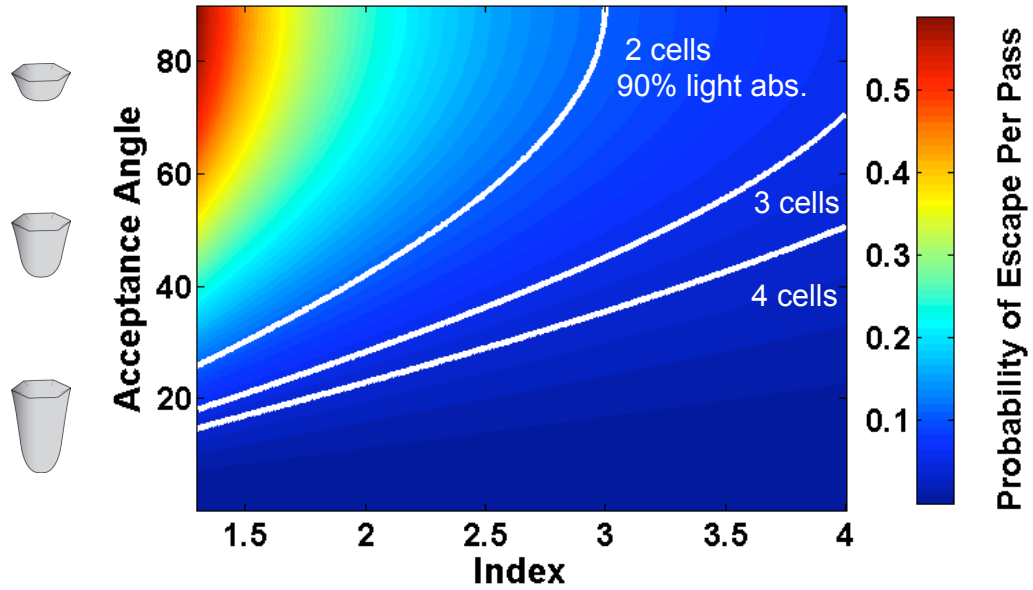


Figure 7.5. Probability of slab escape as a function of the slab refractive index and the acceptance angle of the angle restrictor. Schematics on the left indicate the effect of narrower acceptance angle on the angle restrictor shape. The white lines indicate the minimum angle restrictor acceptance angle and refractive index pairs that give 90% optical efficiency for a given subcell number. Even with only two subcells, very high refractive indices (greater than 3) are necessary if no angle restrictor is desired.

approaches involve tradeoffs. Restricting the acceptance angle of the CPCs reduces the maximum external concentration obtainable or equivalently increases the required tracking angular resolution at a given concentration factor. While slab materials with high index of refraction give higher optical efficiency for a wider acceptance angle, they generally have lower bandgaps, such that absorption in the slab may occur. For example, if the slab were composed of a high index semiconductor material such as GaP, a significant portion of the solar spectrum would be lost to parasitic absorption in the slab. Furthermore, a high index slab complicates the design of the omnidirectional filters. While multilayer films can have omnidirectional reflectivity, this omnidirectionality is dependent on the light line for the incoming light. Thus, for light entering a filter from a high index medium, where the light line encloses a wider region of momentum space, omnidirectionality is much more difficult to achieve [63, 111]. In addition, when filters are composed of high index materials total internal reflection within the dielectric slab becomes a serious issue, as a lower index filter would be required to achieve index contrast between the filter stack and the slab.

7.4 Designing Omnidirectional Filters

To avoid the issues associated with designing omnidirectional filter for use under a high index slab, we focused on the use of a lower index fused silica slab that utilizes an angle restricting front surface layer to improve the optical efficiency. We then designed a range of possible filter options for each of the three underlying subcells. The first consideration is achieving omnidirectional reflectivity. We therefore consider stacks made of SiO_2 and rutile TiO_2 to maximize the index contrast [63, 111, 112]. To design the filters, we used the OpenFilters program, and assumed each filter to have a top interface adjoining the fused silica slab and a bottom interface adjoining subcell with index similar to GaAs [80]. The filters were designed by first creating a chirped stack consisting of alternating layers of rutile TiO_2 and SiO_2 , which provided high reflectivity in the region to the red of the transmission band. Next, we set the desired reflection and transmission at each wavelength and a variety of angles based on the

bandgaps given in Table 7.1. The tolerances of each of these reflection and transmission targets were based on the power in the solar spectrum at that wavelength, the power at a given angle, and an overall reflection to transmission weighting which was varied over the design process. With these targets and tolerances, optimization of all layer thicknesses was performed using the least squares minimization included in OpenFilters [80]. While OpenFilters also includes a needle-based optimization approach, we found that adding needles to the optimized chirped stack had little effect on the filter performance, and thus we did not include needle optimization steps in the final filter designs [113]. As shown in Figure 7.6, with such an approach long pass filters that are nearly omnidirectional may be designed. While there is some wavelength dependence of the cutoff with angle, and a mode allowing transmission at one polarization for a narrow range of angles, overall transmission and reflection are quite omnidirectional.

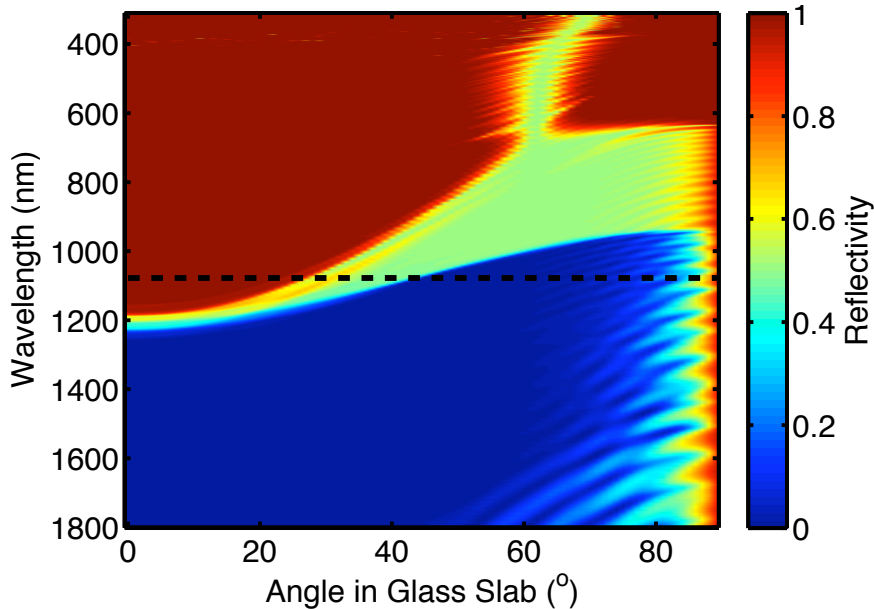


Figure 7.6. Reflectivity as a function of wavelength and angle for an $\text{SiO}_2/\text{TiO}_2$ long pass filter optimized for omnidirectional performance. The final design is 29.6 microns thick, and the black dotted line indicates the wavelength where transmission should begin according to the cell bandgaps given in Table 7.1

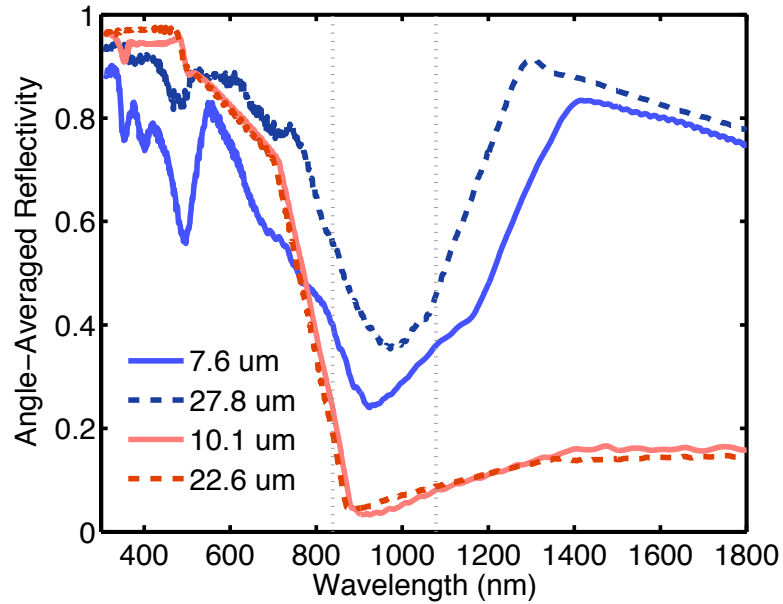


Figure 7.7. Angle averaged reflectivity for $\text{SiO}_2/\text{TiO}_2$ filters optimized for omnidirectional performance. The band pass filters reduce parasitic absorption of lower energy light, but also reduce transmission. The legend gives the thicknesses for each of the filters represented. With thinner filters, greater in band transmission but reduced out of band reflectivity are observed in both band pass and long pass designs. The region between the grey dotted lines indicates where transmission is desired, according to the cell bandgaps given in Table 7.1.

Owing to second order reflections, it is much more difficult to design short or band pass filters that provide omnidirectional reflection and good transmission. In an ideal case, lower energy light will not be absorbed in the higher energy subcells, and thus it is not necessary to use short or band pass filters to keep lower energy light out of these cells. However, in a realistic cell, lower energy light passing through the cell will suffer losses from parasitic free carrier absorption and imperfect back reflection. We estimated these losses at 10-20% for a dual pass through the cell by considering a nominal device design and extrapolating from published free carrier absorption data for similar III-V materials [114-119]. Thus, for the top and middle bandgap subcells, there is a tradeoff between maximizing transmission of in band light to these cells and avoiding losses for lower energy light. If we wish to maximize absorption, a simple anti-reflection coating should be used for the highest energy subcell and a long pass filter for the middle subcell. However, if we wish to minimize parasitic losses, a short pass filter should be used for the top subcell and a bandpass for the middle subcell, with a cost to transmission in the band. Figure 7.7 illustrates this tradeoff for the middle subcell.

As is also evident from Figure 7.7, the thickness of the filter is directly related to the reflection and transmission characteristics. For thinner filters, in-band transmission is improved, but out-of-band reflection is reduced relative to thicker filters. As these filters have fewer layers and fewer interfaces to provide reflection, this result is expected. To further explore these tradeoffs using the ray trace model considered in the next section, a variety of possible filters were designed for each of the three subcells. For the top cell, two different single layer anti-reflection coatings made of TiO_2 and Ta_2O_5 , as well as three short pass filters of different thicknesses were considered. For the middle cell, bandpass filters of several thicknesses were considered, as well as long pass filters. For the bottom cell, only long pass filters were considered. For the long pass filters, as shown in Figure 7.8, filters of two different thicknesses were designed for several cutoff wavelengths, allowing for further optimization.

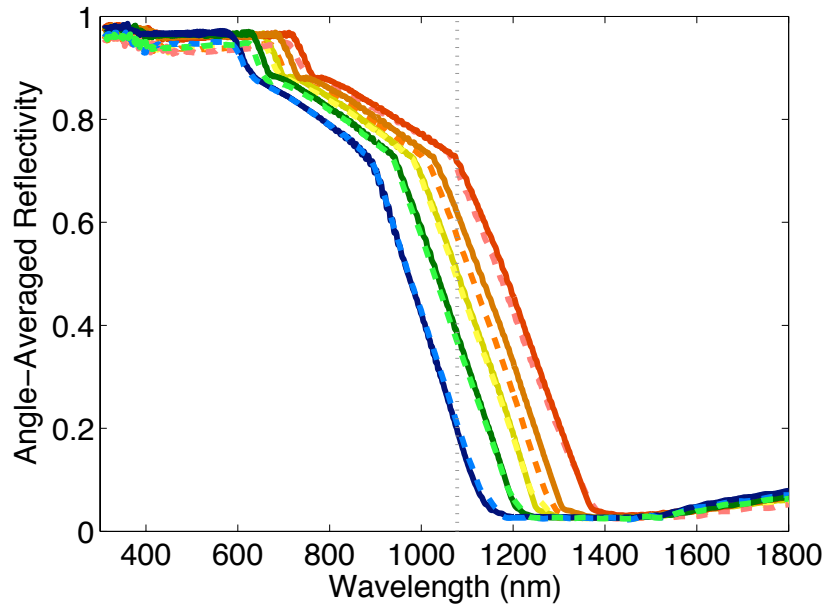


Figure 7.8. Angle averaged reflectivity for $\text{SiO}_2/\text{TiO}_2$ long filters optimized for omnidirectional performance on the lowest energy subcell with a variety of cutoff wavelengths. The dotted lines indicate thinner cells, with thicknesses ranging from 11.1 to 13.2 microns. The solid lines indicate thicker cells, from 25.8 to 33.6 microns thick. Within these ranges, the filters with cutoff at longer wavelengths are thicker. The grey dotted line indicates the start of the desired transmission region, according to the cell bandgaps given in Table 7.1.

7.5 Optimizing Geometry and Filter Selection: Ray Trace Results

7.5.1 Filter Selection

To select the optimal filter set, a ray trace model was developed using LightTools, a commercial ray trace software. For each set of three filter elements for the top, middle, and bottom cells, we then optimize the geometry of the angle restrictor. Based on assumptions about the tracking accuracy and external concentration, the incoming angular spread of the output light can be determined. Assuming the external concentrator is operating at the thermodynamic concentration limit:

$$C_{ext} = \frac{\sin^2 \theta_{out}}{\sin^2 \theta_t} \quad (7.2)$$

where C_{ext} is the external concentration factor, θ_t is the angular accuracy of the tracker, which corresponds to the spread of angles entering the concentrator, and θ_{out} is the angular spread of the light exiting the concentrator [60]. For a given θ_{out} both the input and output angles of the compound parabolic concentrator (CPC) structures must be optimized. In addition, an angular offset expressing the difference between the angle restrictor input acceptance angle and θ_{out} is optimized. Increasing the input acceptance angle of the angle restrictor slightly relative to θ_{out} reduces the effectiveness of the angle restrictor for trapping light within the slab, but can also improve transmission through the angle restrictor.

For each geometry, the band gaps are re-optimized to achieve current matching for the incoming photon flux, as is discussed further in the next section. For the ray trace, we assume 20% parasitic loss for dual pass of below band gap light through the cell. This is at the upper end of our previous estimates. We also assume 98% reflectivity at reflecting surfaces within the angle restrictor and on the top and sides of the slab, as for a silver-based mirror. In addition, unless otherwise noted, we assume a tracking accuracy angle θ_t , of 0.5° , as has been reported for deployed systems. We also neglect Fresnel reflections at the output of the angle restrictor, as we assume

an as yet unspecified anti-reflective coating will be deposited at this interface. With idealized reflectors and filters, the ray trace results accord well with the results of the multipass model.

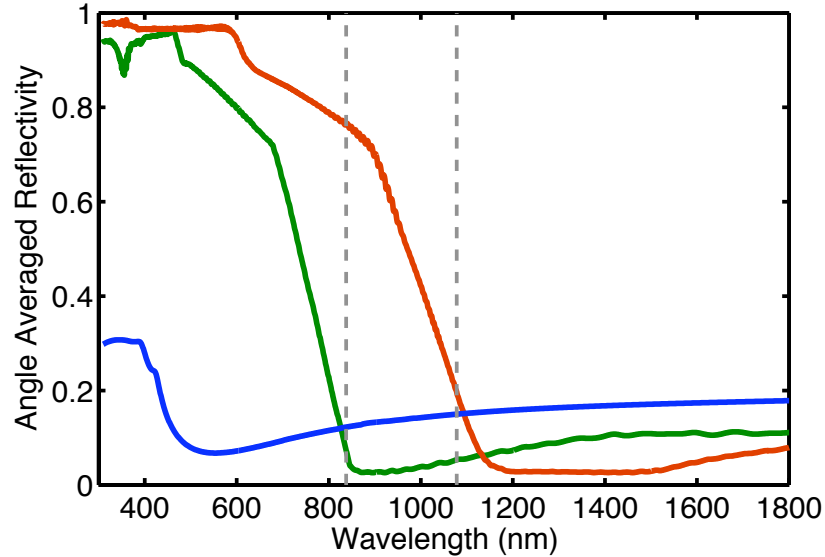


Figure 7.9. Angle averaged reflectivity for the filter selected based on ray trace results. Top cell tantalate based AR coat (blue line), middle cell long pass filter which is 9.8 microns thick (green line), and bottom cell long pass filter which is 25.8 microns thick (red line) are plotted. The dashed gray lines indicate the spectral regions for each subcell given in Table 7.1.

Owing to the computational intensity of the ray tracing angle restrictor optimization, and the large number of filter combinations, we did not examine every possible filter combination. Instead, we observed trends to arrive at a final filter set. We found that transmission into the top and middle cells was more important than avoiding parasitic loss of below bandgap light. Therefore, a tantalate based anti-reflective coating was preferable for the top cell, and a long pass filter was preferable for the middle cell, as shown in Figure 7.9. For the long pass filters, the cutoff was shifted maximally to shorter wavelengths within the initial filter set. As shown in Figure 7.9, this leads to maximal transmission for in-band light. For the middle cell filter, a smaller number of layers is preferable, to maximize in-band transmission. In contrast,

for the bottom cell filter, increasing reflection of higher energy light is more important, and a thicker filter with many more layers is preferable. In future, it would be interesting to investigate filters with cutoffs at even shorter wavelengths, as well as even smaller numbers of layers for the middle cell filter.

7.5.2 Subcell Re-Optimization

With the ideal filter set chosen, the bandgaps of each subcell must be re-optimized to achieve closer current matching with the resulting photon flux. However, due to parasitic losses, the photon flux for each cell is dependent on the bandgaps of all the subcells. To achieve a self-consistent set of bandgaps and efficiency, we first perform the ray trace, then re-optimize the bandgaps to achieve current matching with the resulting photon flux. Then, we ray trace again with the re-optimized bandgaps, and impose current matching with the resulting photon flux. Thus, while the final result is self-consistent, it is not completely current matched, imposing a small loss.

Table 7.2 gives the optimized cell bandgaps for the resulting photon flux. Compared to the original bandgaps on which the filter designs were based, the bandgaps increase, particularly the highest energy bandgap in each subcell. This occurs because the filters are not ideal, and light of higher energy is admitted into the subcells, as is shown in Figure 7.10. As in Table 7.2, the highest bandgap under the resulting photon flux with current matching rises above the 2.2 eV limit we set previously owing to materials considerations. Current matching cannot be achieved with the resulting photon fluxes and the 2.2 eV limitation in a triple junction cell. Thus, we consider a dual junction instead for the highest bandgap cell, which allows for a reasonable highest bandgap and current matching. As shown in Table 7.2, this leads to a slight reduction in overall efficiency. In future, we could also lower the nominal cutoff in the ray trace for the highest energy spectral region, so that current matching could be achieved with a triple junction cell and a reasonable top bandgap.

Table 7.2. Subcells Optimized for Resulting Photon Flux

	Original Set	Overall Optimum	Limited Top Bandgap
	2.20 eV	2.31 eV	2.08 eV
Top Cell	1.78 eV	1.87 eV	1.49 eV
	1.48	1.49 eV	—
	1.37 eV	1.58 eV	1.58 eV
Middle Cell	1.23 eV	1.37 eV	1.37 eV
	1.15	1.16 eV	1.16 eV
	0.93 eV	1.02 eV	1.02 eV
Bottom Cell	0.70 eV	0.70 eV	0.70 eV
	—	—	—
Efficiency	—	36.8%	35.5%

The table above gives bandgaps for the subcells re-optimized for the incoming photon flux with the final filter set shown in Figure 7.9. The leftmost column gives the original cell bandgaps on which the filter design and initial ray trace were based, as a point of comparison. To achieve self-consistency, current matching is not ideal. With a top triple junction cell achieving near current-matching leads to a very high top bandgap. To limit the top bandgap, we consider a dual junction for the highest energy cell. Efficiency values assume 1% ERE and 90% of ideal current to model realistic cell performance.

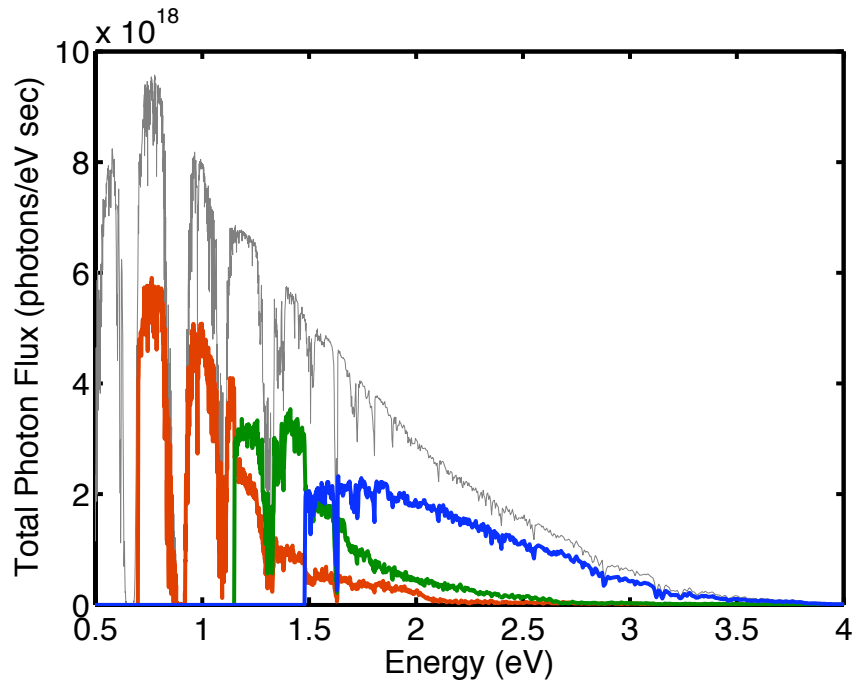


Figure 7.10. Photon flux entering top (blue line), middle (green line), and bottom (red line) subcells for optimized geometry, filter and band gaps, with dual junction top and bottom cells, as in Table 7.2. The input aperture for the ray trace structure is 23.2 mm^2 , and the photon fluxes are averaged over each subcell type. The grey line shows the incident photon flux for the AM 1.5 direct spectrum as a comparison. There is some misallocation of photons to lower energy cells, as well as some photons that escape the slab before they are absorbed.

7.5.3 Angle Restrictor Geometry Optimization

To arrive at the re-optimized bandgap sets introduced in Table 7.2, we optimized the input angle, output angle, and angular offset for the angle restrictor. For both sets of bandgaps the optimal angle restrictor parameters are the same, with an input angle of 11° , output angle of 50° , and no angular offset. The narrower output angle reduces losses from skew rays in the corners of the hexagonal CPC, and no angular offset is necessary to maintain transmission with these parameters. Figure 7.11 illustrates the optimal input and output angles for the optimal case of zero angular offset, showing the optimal efficiency given in Table 7.2.

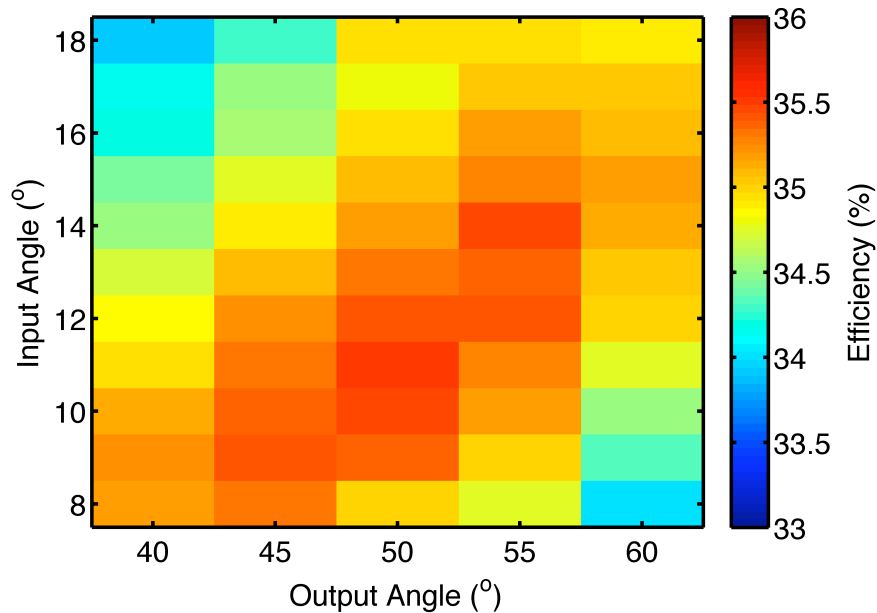


Figure 7.11. Efficiency for two dual junction subcell set given in Table 7.2 as a function of angle restrictor input and output angle. 1% ERE and 90% of ideal current are assumed to model realistic cells.

For this optimal design with an assumed tracking accuracy angle of 0.5° , the external concentration corresponds to 478 suns. However, it may be desirable to decrease the external concentration to avoid heating and series resistance losses or to increase the concentration to reduce the cost of the module. Therefore, as in Figure 7.12, we vary the external concentration for several values of the tracking

accuracy angle. While the angle restrictor input angle is optimized for each case, the output angle and angular offset are not, to reduce the computational intensity. We see that there is a fairly broad range of external concentration where efficiency is well maintained, particularly for improved tracking accuracy. In addition, improved tracking accuracy significantly increases the optimal external concentration value, and maximum achievable efficiency.

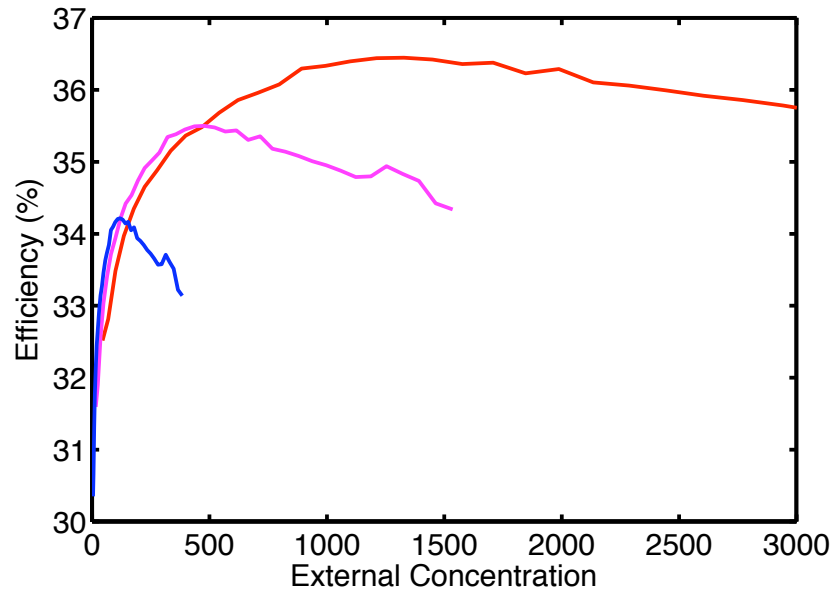


Figure 7.12. Efficiency as a function of external concentration for two dual junction subcells and tracking accuracies of 1° (blue), 0.5° (purple) and 0.3° (red). 1% ERE and 90% of ideal current are assumed to model realistic cells. The kinks in the data are likely due to the fact that the angle restrictor is not fully optimized for each case.

7.6 Conclusions

The light trapping filtered concentrator is an interesting approach to spectrum splitting, as it relies on scattered, trapped light, rather than a deterministic light path. Here we have presented an initial optimized design with greater than 35% predicted

efficiency for realistic cells and filters with seven junctions in three underlying multijunction subcells. We find that nearly omnidirectional reflectivity can be obtained with simple $\text{TiO}_2/\text{SiO}_2$ multilayer stacks placed under a glass slab. However, to improve optical efficiency in such a low index slab, an angle restrictor is necessary on top of the slab. With a ray trace, we found several trends in selecting the highest performance filter set. For the top and middle subcells, transmission is more important than reflection of below bandgap light, so an anti-reflective coating is optimal for the top subcell, with long pass filters for the other two subcells. We also found that cutoffs for the long pass filters should be shifted to shorter wavelengths to allow further transmission. Finally, we found that region of high efficiencies is quite broad relative to the external concentration, allowing for some design flexibility.

Despite these conclusions, significant further work remains in optimizing this structure. Based on the conclusions from this first round of optimization, further filter design is necessary, with a focus on improving transmission and designing filters with slight variations from the highest performing designs identified here. In particular, the optimal number of layers and the filter cutoff should be varied, so that the filter set may be further refined. In addition, the ray trace spectral region assumptions should be carefully explored to determine if a triple junction top subcell could produce a noticeable increase in efficiency with a reasonable highest bandgap. Finally, alternative geometries should be considered, including varying number of subcells, and placing subcells on the upper surface of the slab between the angle restrictor output apertures to improve optical efficiency and reduce reflector losses.

Chapter 8

Conclusions and Outlook

In this thesis several approaches to improving solar efficiency with careful optical design have been proposed. These approaches attempt to improve both the solar cell current, as with light trapping, and the solar cell voltage, as with photon recycling. Finally, the spectrum splitting approach addresses thermalization and lack of absorption losses for improved efficiency. Here, each approach will be briefly reviewed, and opportunities for future work in each area will be identified.

We first considered a ray optical model for understanding light trapping in silicon microwires. While the agreement with experiment was reasonable for large wires, for thinner wires absorption was significantly stronger than that predicted by the model, which we attributed to ray optical effects. An interesting tradeoff arises where thinner wires allow for improved optical absorption, but may also introduce issues with carrier collection, as it can be difficult to define an efficient junction in a thin wire. Coupled electrical and optical simulations, as developed by other members of the group, could be useful for addressing this question. Additionally, we briefly considered a model that attempted to use the optical cross sections from Mie theory to capture the wave optical effects without the computational intensity of finite difference methods, and this could be an interesting avenue for further work.

From the angle restriction calculations, we identified that light trapping GaAs cells produced the highest efficiencies, as they took full advantage of both enhanced light trapping and photon recycling effects. However, current GaAs cells are made in a planar geometry, as epitaxially grown films are smooth and planar. A light trapping geometry would allow for a thinner cell, and also make the photon recycling effect more robust to bulk non-radiative recombination. There are several possible

approaches to achieving a light trapping GaAs cell, including some that are being pursued in the group. Owing to the necessity of maintaining high quality material, directly texturing the cell, as is currently done with silicon, is probably not an option. However, one could imagine introducing individual scatterers or scattering surfaces made of high index materials such as TiO_2 or GaP at either the top or back surface of the cell. For angle restriction cells, the back surface is likely preferable, so that angle restriction optics may be placed on the front surface. Design of such a scattering surface, likely using finite difference optical modeling, is a necessary next step in achieving a light trapping GaAs cell for angle restriction. In addition, such a structure would need to be incorporated into a thin, high radiative efficiency GaAs cell which has been lifted off the growth substrate. Over large areas, nanoimprint lithography could prove to be a scalable technique for patterning such a scattering structure.

With planar cells, enhanced photon recycling may be observed, as we demonstrated experimentally with a simple optical multilayer. However, despite the observed voltage increase, we could not demonstrate efficiency enhancements, as normal incidence reflections led to reductions in the current. As we showed computationally, a rugate type angle restrictor design could avoid these current losses so that efficiency increases could be observed. Thus, a natural next step is to fabricate a rugate structure in order to observe these effects experimentally. These experiments could be performed either with thick, planar cells as in our previous experiment, or with thinned light trapping cells, as described above. For light trapping cells, further modeling is required to examine the effects of the narrowband angle restriction provided by the rugate structure, as opposed to the broadband angle restriction considered in this thesis. With narrowband angle restriction, thicker light trapping cells may be required.

For very thin light trapping GaAs cells, fabrication and integration of broadband angle restrictors is another interesting area for future research. As was shown in this work, two-photon lithography can allow for patterning of closely spaced cup-like structures at approximately the ten micron scale. These small scale structures are required so that the areas of illumination for each structure will be within a diffusion

length of each other. While two-photon lithography can produce structures on this scale, this technique is not scalable. A molding process from a master fabricated with two-photon lithography could allow for fabrication over large areas. One could imagine using PDMS or a silica sol-gel to infill the master and make a molded structure. The resulting solid cup structures would then transmit light by total internal reflection. Finally, the array of solid cup structures could be aligned over an array of holes patterned into a reflector which covered most of the top of the cell. The resulting structure would be similar to the broadband angle restrictor presented here for silicon solar cells, though it would need to be fabricated on a significantly smaller scale. While such a process requires an alignment step, it avoids coating the inside of high aspect ratio cup-like structures with high reflectivity metal, as with the fabricated structures presented here. Furthermore, the fabrication of the holes at the bottom of the structures is significantly simplified.

For silicon solar cells, experimental demonstration of enhanced efficiency with angle restriction is a clear next step. As our calculations indicate, HIT-type cells with high voltage show the strongest effects with angle restriction, with thicknesses around 50 microns giving the highest possible efficiencies. While rugate type-structures may be used for angle restriction in silicon, the angle restriction improvement is substantially reduced. Therefore, broadband angle restrictors seem preferable for experimental demonstration. To fabricate broadband angle restrictors similar to the design that we have proposed here for silicon, we can use an approach similar to that outlined above for GaAs cells. However, as diffusion lengths are significantly longer in silicon, the cup structure spacing can be on the order of 100 microns, rather than 10 microns for GaAs. At these size scales, write times for fabricating a mold master via two-photon lithography would be very long, and some sort of micro-machining process would likely be preferable.

While this thesis has focused primarily on narrowband angle restrictors with rugate or dielectric multilayer designs and broadband angle restrictors, future work need not be limited to these two approaches. While the narrowband approach allows for diffuse light, for silicon it does not provide angle restriction over all the weakly ab-

sorbing wavelengths. In addition, the angle restriction cannot be made very narrow with dielectric multilayer or rugate designs. Therefore, future work could focus on novel designs that are narrowband, but where the angle restriction is narrower and can occur over a wider wavelength band if desired.

Lastly, we considered an initial, optimized design for the light trapping filtered concentrator spectrum splitting approach. While this design is a promising start, the design space is still not fully explored. Two or four subcells could also be considered, with either dual or triple junction approaches. In addition, it could be interesting to replace the reflector between the angle restrictor apertures with additional cells. This would eliminate losses in the reflector, and should also improve the optical efficiency of the design. Finally, this spectrum splitting approach could also be utilized with lower cost solar cells, such as copper indium gallium selenide (CIGS) and polymer thin films. For these materials efficiency targets would be lower, and angle restrictors and external concentration would likely not be used, so that the module would be flat plate and no tracking would be required. With CIGS, multiple bandgaps may be grown, but it is difficult to make monolithic tandems, so this simple spectrum splitting approach could allow for higher efficiencies. For polymer solar cells, absorption is relatively weak for energies far from the bandgap, and thus filter elements need not necessarily be included.

While there has been significant work considering the optics of solar cells, most of this work has focused on absorption. Here, by considering the thermodynamic limits of solar cells, we have explored additional avenues for optics to enhance solar cell efficiency. The angle restriction approach addresses losses due to emitted light, while the spectrum splitting approach addresses losses due to thermalization and lack of absorption. Thus, optics can be used not only to increase the current by improving absorption, but also to enhance the voltage and address thermalization loss. While these possibilities are tantalizing, much work remains to fully explore these additional avenues for enhancing solar cell efficiency.

Appendix A

Detailed Balance Code for GaAs

Most of the code that was written for the calculations in this thesis simply uses the equations given here or in the references. However, these appendices provide commented versions of the central functions for the detailed balance calculations in GaAs and silicon so that any future users of the codes will know where to begin. While the principles of detailed balance are the same for both GaAs and silicon, for historical and technical reasons the codes were written separately and address the problem somewhat differently. For GaAs, the function shown below first finds the short circuit current by integrating the solar spectrum and the absorptivity. The absorptivity is found using the modified Stuart and Hall formalism presented in Chapter 3, and contained within the `findAbsModes` function. The current-voltage curve is then traced by varying the voltage and calculating the current losses due to emission and parasitic absorption of radiatively emitted light, as well as Auger recombination. Note that the energies at which the radiative emission is calculated are unevenly distributed to accurately describe the peak shape while minimizing computational overhead. Finally, the maximum power point and efficiency are found.

```
function [eff]= findEfficiency2(theta,W,Rrefl)

%This finds the cell efficiency for a given emission angle (theta), cell
%thickness, W, in nm, and back reflectivity for a light-trapping GaAs cell.
echg=1.60217646e-19;%in coloumbs so are we get amps

load Si3N4final.mat %for cladding layers
```

```

n3s=ns;
n1s=ns;
eVs3=eVs;
eVs1=eVs;
Cauger=7e-30;
nia=1.67e6;
load GaAsfinal.mat %GaAs Optical Constants

anevs=eVs;
clear eVs;
h=4.135e-15;
c=3e10;
bbconst=2/(h^3*c^2);
kT=.025852;%at 300K in eV
Eg=1.424;

abe=interp1(anevs,as,Eg);
nbe=interp1(anevs,ns,Eg);
n1be=interp1(eVs1,n1s,Eg);
n3be=interp1(eVs1,n1s,Eg);

%First we find the short circuit current by integrating absorptivity and
%the solar spectrum
load PhotonFluxvsE;
for m=1:length(eVs)
    if(eVs(m)<Eg)
        as1(m)=0;
        ns1(m)=interp1(anevs,ns,eVs(m));

        abs(m)=0;
        absp(m)=0;

    else
        as1(m)=interp1(anevs,as,eVs(m));
    end
    if(as1(m)~=0)

```

```

ns1(m)=interp1(anevs,ns,eVs(m));
n1=interp1(eVs1,n1s,eVs(m));
n3=interp1(eVs1,n1s,eVs(m));
alphap=(1-Rrefl)/(4*W);
alphapsave(m)=alphap;
[abs(m),absp(m)]=
    findAbsModes(theta,W,n1,ns1(m),n3,as1(m),1240/eVs(m),alphap);
if(abs== -1)
    error='Mode Solver Fail!'
end

toInt(m)=photonFlux(m)*abs(m)*echg;
else
    toInt(m)=0;
end

end

[eVints,reind]=sort(eVs(1:(m-1)));
intf=toInt(reind);
photonFlux1=photonFlux(1:(m-1));
fluxInt=photonFlux1(reind);
Jsc=trapz(eVints,intf); %This is in amps/cm^2

Estop=max(eVs);
if(Estop<kT*100)
    error='Estop too low. Saturation Current May be WRONG!!!!';
end
numReg=250;
Es=linspace(Eg,1.7,numReg);
Es(numReg+1:numReg+250)=linspace(1.71,Estop,250);

%Now we find current loss from radiatively emitted light across a range of
%voltages, as well as Auger recombination loss.

```

```

vs=linspace(0,Eg-.0001,500);
for v=1:length(vs)
    for p=1:length(Es)
        if(v==1)
            alphap=(1-Rrefl)/(4*W);
            n1=interp1(eVs1,n1s,Es(p));
            n3=interp1(eVs1,n1s,Es(p));
            ns1(p)=interp1(anevs,ns,Es(p));
            as1(p)=interp1(anevs,as,Es(p));
            [abs2(p),absp2(p)]=
                findAbsModes(theta,W,n1,ns1(p),n3,as1(p),1240/Es(p),alphap);
            %This is based on Stuart and Hall, and calculates the modal
            %strucutre assuming silicon nitride cladding
        end

        toInt2(p)=echg*(abs2(p))*bbconst*Es(p)^2/(exp((Es(p)-vs(v))/kT)-1);

        toInt2p(p)=echg*(absp2(p)*ns1(p)^2
            *bbconst*Es(p)^2/(exp((Es(p)-vs(v))/kT)-1);
        if(toInt2(p)<0)
            error=negJo
        end
    end
end

Auger(v)=echg*Cauger*(W*1e-7)*nia^3*exp(3*vs(v)/(2*kT));
Jo(v)=pi*sind(theta)^2*trapz(Es,toInt2);
Jop(v)=pi*trapz(Es,toInt2p);
Is(v)=Jsc-Jo(v)-Jop(v)-Auger(v);
Ps(v)=Is(v)*vs(v);
if(Is(v)<=0)
    break;
end
end
end

```

```
%Having traced the IV curve, we now find the max power point and efficiency
[maxP,maxInd]=max(Ps);
eff=maxP/totPower;
Josave=Jo(maxInd);
Jopsave=Jop(maxInd);
Augersave=Auger(maxInd);

save(['DataW',num2str(W),'theta',num2str(theta),'.mat'],'eff','Is','vs',
'Josave','Jopsave','Augersave','Auger','Jo',
'Jop','Jsc','Ps','abs','absp','eVs');
end
```

Appendix B

Detailed Balance Code for Silicon

For the silicon calculations, free carrier absorption is included, so the light generated current is voltage dependent. This is quite different from GaAs, where the light generated current has no voltage dependence and may be equated with the short circuit current. As the light generated current must be recalculated at every voltage, the central function here simply finds the net current and efficiency at a given voltage. The function may be modified to return either the net current, or the negative of the efficiency at the given voltage, also known as the efficiency figure of merit, as shown here. The open circuit voltage can be determined by minimizing the net current, while the short-circuit current is simply the net current at zero voltage. To determine the efficiency at the maximum power point, the efficiency figure of merit is minimized. Built-in Matlab functions are used to perform these minimizations. One other difference relative to the GaAs code is that Bonna Newman adapted this code to take advantage of the fast vector multiplication in Matlab. This avoids many of the for loops found in the code as originally implemented, and leads to significantly faster run times.

```
function [FOM]= findEffatV_fast (Va,theta,W,Refl,SRV,  
                                tauBulk,Nb,ptype,spectrum,HITtop,HITtot,Cf)  
% The goal of this function is to find the net current at a given voltage,  
% accounting for Auger, radiative emission, free carrier absorption,  
% surface, and bulk non-radiative recombination. Inputs: dopant density,  
% angle of emission, cell thickness (nm),SRV,bulk lifetime, voltage and  
% dopant type  
%HIT top is the thickness of the a-Si passivation layer for a HIT cell;
```

```

%this is used to calculate parasitic absorption of the incoming light
%HITtot is the total thickness of a-Si (top and bottom) this is used to
%modify the back reflectivity
%Cf is the external concentration
%Initial parameter loading
echg=1.60217646e-19;%in coloums so are we get amps
load SioptdataGreen.mat
ni=8.28e9; %per cm^3 at 25C from Richter
anevs=eVs;
clear eVs;
h=4.135e-15;
c=3e10;
bbconst=2/(h^3*c^2);
kT=.0256926;%at 25C in eV
Eg=1.050847; %This is where band to band absorption truly becomes zero...
load(spectrum); %using direct spectrum for now
load aSiPalik.mat
%first we turn the approximate voltage (Va) into dN
V0a=ni^2; %from Richter w/o BGN;
if(ptype)
    p0=Nb+ni;%p0a=(Nb+sqrt(Nb^2+4*V0a))/2;
    n0=V0a/p0; %n0a = V0a/p0a;
else
    n0=Nb+ni;%n0a=(Nb+sqrt(Nb^2+4*V0a))/2;
    p0 = V0a/n0;%p0a=V0a/n0a;
end

dNa=(-1*(n0+p0)+sqrt((n0+p0)^2-4*(n0*p0-V0a*exp(Va/kT))))/2;
%Now figuring out effective intrinsic carrier concentration based on
%Schenk's BGN parameterization
nieff=findBandgapNarrowing2(Nb,ptype,dNa);
nia = nieff;
dN = (-1*(n0+p0)+sqrt((n0+p0)^2-4*(n0*p0-nia^2*exp(Va/kT))))/2;
V = Va;
%Now we need to figure out the current, including FCA
ind1 = find(eVs<Eg); % indices less than Eg

```

```

ind2 = find(eVs>Eg); % indices greater than Eg

as1(ind1) = 0;
ns1(ind1) = interp1(anevs,ns,eVs(ind1));

as1(ind2) = interp1(anevs,as,eVs(ind2));

ind3 = find(as1); %indices of as1 not equal to 0

ns1(ind3) = interp1(anevs,ns,eVs(ind3));

indaSi = find(eVs > 1.4002);
aaSi = zeros(size(eVs));
aaSi(indaSi) = interp1(aSieVs,aSias,eVs(indaSi));

%Here we account for back reflector losses, incl. a-Si losses where
%applicable
Rreflval=exp(-2*HITtot*aaSi)*Refl;
alphap=(1-Rreflval)./(4*W);
lambdaum=1.24./eVs;

alphaFCap=1e-7*2.6e-18.*(p0+dN).*lambdaum.^2.4;
alphaFCAn=1e-7*1.8e-18.*(n0+dN).*lambdaum.^2.6;
alphap=alphap+alphaFCap+alphaFCAn;

%Light not lost in the top layer of a-Si before scattering
firstPass = exp(-HITtop.*aaSi);

[abs] = findAbsModes(theta,W,ns1,as1,alphap,0);

toInt = zeros(size(eVs));
toInt(ind3) = Cf.*photonFlux(ind3).*abs(ind3).*echg.*firstPass(ind3);

[eVints,reind]=sort(eVs(1:(length(eVs)-1)));
intf=toInt(reind);

```

```

JL=trapz(eVints,intf); %Absorbed photon flux expressed as a current

%Now that we know the incoming photon flux, all that's left to include is
%the various sources of recombination: radiative (including emitted photons
%absorbed by FCA and the back reflector), Auger (using Richter's model),
%and SRV and bulk recombination, and we'll have the net current
%First we deal with the radiative emission....
Estop=max(eVs);
if(Estop<kT*100)
    error='Estop too low. Saturation Current May be WRONG!!!!';
end
numReg=250;
Es=linspace(Eg,1.4,numReg);
Es(numReg+1:numReg+400)=linspace(1.4,Estop,400);

indEs = find(Es > 1.4002);
aaSi = zeros(size(Es));
aaSi(indEs) = interp1(aSieVs,aSias,Es(indEs));
    Rreflval=exp(-2*HITtot*aaSi)*Refl;
    alphap=(1-Rreflval)/(4*W);

    ns1=interp1(anevs,ns,Es);
    lambdaum=1.24./Es;

    alphaFCAp=1e-7.*2.6e-18.*(p0+dN).*lambdaum.^2.4;
    alphaFCAn=1e-7.*1.8e-18.*(n0+dN).*lambdaum.^2.6;
    alphap=alphap+alphaFCAp+alphaFCAn;
    as1=interp1(anevs,as,Es);
    [abs2,absp2]=findAbsModes(theta,W,ns1,as1,alphap,0);

    toInt2=echg.*(abs2).*bbconst.*Es.^2./(exp((Es-V)./kT)-1);

    toInt2p=echg.*(absp2.*ns1.^2).*bbconst.*Es.^2./(exp((Es-V)./kT)-1);

```

```

%This is the current lost due to radiative emission of
%emitted light from the cell
Jo=pi*sind(theta)^2*trapz(Es,toInt2);
%This is the current lost due to absorption of emitted light in the
%non-ideal back-reflector
Jop=pi*trapz(Es,toInt2p);

%Based on Nelson's expressions, assume mid gap traps and same
%lifetimes for electrons and holes (see Physics of Solar Cells p.
%108 and p. 110)
SR=echg*2*((n0+dN)*(p0+dN)-nia^2)/((p0+dN+nia)/SRV+(n0+dN+nia)/SRV);
if(tauBulk>0)
SRH=echg*W*1e-7*
((n0+dN)*(p0+dN)-nia^2)/(tauBulk*(p0+dN+nia)+tauBulk*(n0+dN+nia));
else
    SRH=0;
end
% From Richter's model (Phys. Rev. B 86, 165202 (2012)),
% using the inverse of his intrinsic expression for lifetime, to
% turn into a bulk rate and multiply by thickness and charge.
% Also, taking out radiative part, since we have accounted for that
% separately...

%Then we implement Richter's model
Noeeh=3.3e17;
Noehh=7.0e17;
geeh=1+13*(1-tanh((n0/Noeeh)^0.66));
gehh=1+7.5*(1-tanh((p0/Noehh)^0.63));
Auger=echg*W*1e-7*((n0+dN)*(p0+dN)-nia^2)*
(2.5e-31*geeh*n0+8.5e-32*gehh*p0+3e-29*dN^.92);

netJ=JL-Jo-Jop-SR-SRH-Auger;
power=netJ*V;
eff=power/(Cf*totPower);
FOM=-eff;
end

```

Bibliography

- [1] G.W. Crabtree and N.S. Lewis. Solar energy conversion. *Physics Today*, 60(3), 2007.
- [2] C. Kost, J. Mayer, J. Thomsen, N. Hartmann, C. Senkpiel, S. Philipps, S. Nold, S. Lude, N. Saad, and T. Schlegl. Levelized cost of electricity renewable energy technologies. Technical report, Fraunhofer Institute for Solar Energy Systems ISE, 2013.
- [3] \$1/W Photovoltaic Systems White Paper to Explore a Grand Challenge for Electricity from Solar. Technical report, U.S. Department of Energy Advanced Research Projects Agency-Energy, 2010.
- [4] R.A. Sinton, P.J. Verlinden, R.A. Crane, R.M. Swanson, C. Tilford, J. Perkins, and K. Garrison. Large-area 21% efficient si solar cells. In *Photovoltaic Specialists Conference, 1993., Conference Record of the Twenty Third IEEE*, pages 157–161, May 1993.
- [5] L.W. James. III-V compound heterojunction solar cells. In *Electron Devices Meeting, 1975 International*, volume 21, pages 87–90, 1975.
- [6] M. Taguchi, A. Yano, S. Tohoda, K. Matsuyama, Y. Nakamura, T. Nishiwaki, K. Fujita, and E. Maruyama. 24.7% record efficiency HIT solar cell on thin silicon wafer. *IEEE Journal of Photovoltaics*, 4(1):96–99, Jan 2014.
- [7] E. Yablonovitch. Statistical ray optics. *Journal of the Optical Society of America*, 72(7), 1982.

- [8] M.D. Kelzenberg, S.W. Boettcher, J.A. Petykiewicz, D.B. Turner-Evans, M.C. Putnam, E.L. Warren, J.M. Spurgeon, R.M. Briggs, N.S. Lewis, and H.A. Atwater. Enhanced absorption and carrier collection in si wire arrays for photovoltaic applications. *Nature Materials*, 9:239–244, 2010.
- [9] E. Garnett and P. Yang. Light trapping in silicon nanowire solar cells. *Nano Letters*, 10:1082–1087, 2010.
- [10] L. Tsakalacos, J. Balch, J. Fronheiser, M. Shih, S.F. LaBoeuf, M. Pietrzykowski, P.J. Codella, B.A. Korevaar, O. Sulima, J. Rand, A. Davuluru, and U. Ropol. Strong broadband absorption in silicon nanowire arrays with a large lattice constant for photovoltaic applications. *Journal of Nanophotonics*, 1:013552, 2007.
- [11] B. Tian, X. Zheng, T.J. Kempa, Y. Fang, J. Huang, and C.M. Lieber. Coaxial silicon nanowires as solar cells and nanoelectronic power sources. *Nature*, 449: 885–889, 2007.
- [12] E. Garnett and P. Yang. Silicon nanowire radial p-n junction solar cells. *Journal of the American Chemical Society*, 130:9224–9225, 2008.
- [13] B.M. Kayes, H.A. Atwater, and N.S. Lewis. Comparison of the device physics principles of planar and radial p-n junction nanorod solar cells. *Journal of Applied Physics*, 7:114302–114311, 2005.
- [14] M.C. Putnam, S.W. Boettcher, M.D. Kelzenberg, D.B. Turner-Evans, J.M. Spurgeon, E.L. Warren, R.M. Briggs, N.S. Lewis, and H.A. Atwater. Si microwire-array solar cells. *Energy & Environmental Science*, 3:1037–1041, 2010.
- [15] L. Hu and G. Chen. Analysis of optical absorption in silicon nanowire arrays for photovoltaic applications. *Nano Letters*, 7:3249–3252, 2007.
- [16] C.E. Kenrick, H.P. Yoon, Y.A. Yuwen, G.D. Barber, H. Shen, T.E. Mallouk, E.C. Dickey, T.S. Mayer, and J.M. Redwing. Radial junction silicon wire ar-

- ray solar cells fabricated by gold-catalyzed vapor-liquid-solid growth. *Applied Physics Letters*, 97:143108, 2010.
- [17] K. Peng and S. Lee. Silicon nanowires for photovoltaic solar energy conversion. *Advanced Materials*, 23:198–215, 2011.
- [18] O. Gunawan, K. Wang, B. Fallahazad, Y. Zhang, E. Tutuc, and S. Guha. High performance wire-array silicon solar cells. *Progress in Photovoltaics*, 10:1002, 2010.
- [19] J. Zhu, Z. Yu, G.F. Burkhard, C. Hsu, S.T. Connor, Y. Xu, Q. Wang, M. McGehee, S. Fan, and Y. Cui. Optical absorption enhancement in amorphous silicon nanowire and nanocone arrays. *Nano Letters*, 9(1):279–282, 2009.
- [20] C. Lin and M.L. Povinelli. Optical absorption enhancement in silicon nanowire arrays with a large lattice constant for photovoltaic applications. *Optics Express*, 17:19371–19381, 2009.
- [21] Lin C and M. L. Povinelli. Optimal design of aperiodic, vertical silicon nanowire structures for photovoltaics. *Optics Express*, 19(S5):A1148–A1154, Sep 2011.
- [22] B. C. P. Sturmberg, K. B. Dossou, L. C. Botten, A. A. Asatryan, C. G. Poulton, C. Martijn de Sterke, and R. C. McPhedran. Modal analysis of enhanced absorption in silicon nanowire arrays. *Optics Express*, 19(S5):A1067–A1081, Sep 2011.
- [23] B. C. P. Sturmberg, K. B. Dossou, L. C. Botten, A. A. Asatryan, C. G. Poulton, R. C. McPhedran, and C. Martijn de Sterke. Nanowire array photovoltaics: Radial disorder versus design for optimal efficiency. *Applied Physics Letters*, 101(17):173902, 2012.
- [24] H. Alaeian, A. C. Atre, and J. A. Dionne. Optimized light absorption in Si wire array solar cells. *Journal of Optics*, 14(2):024006, 2012.

- [25] M.C. Putnam, D.B. Turner-Evans, M.D. Kelzenberg, S.W. Boettcher, N.S. Lewis, and H.A. Atwater. 10 μm minority-carrier diffusion lengths in Si wire synthesized by Cu-catalyzed vapor-liquid-solid growth. *Applied Physics Letters*, 95:163116, 2009.
- [26] M. Born and E. Wolf. *Principles of Optics, 7th Ed.* Cambridge University Press, 1999.
- [27] K.E. Plass, M.A. Filler, J.M. Spurgeon, B.M. Kayes, S. Maldonado, B.S. Brunschwig, H.A. Atwater, and N.S. Lewis. Flexible polymer-embedded Si wire arrays. *Advanced Materials*, 21:325–328, 2009.
- [28] C.F. Bohren and D.R. Huffman. *Absorption and Scattering of Light by Small Particles.* Wiley-VCH, 2004.
- [29] W. Shockley and H.J. Queisser. Detailed balance limit of efficiency of p-n junction solar cells. *Journal of Applied Physics*, 32(3):510–519, 1961.
- [30] P. Campbell and M.A. Green. The limiting efficiency of silicon solar cells under concentrated sunlight. *IEEE Transactions on Electron Devices*, ED-33:234–239, 1986.
- [31] G.L. Araújo and A. Martí. Absolute limiting efficiencies for photovoltaic energy conversion. *Solar Energy Materials and Solar Cells*, 33:213–240, 1994.
- [32] A. Martí, J.L. Balenzategui, and R.F. Reyna. Photon recycling and Shockley’s diode equation. *Journal of Applied Physics*, 82(8):4067–4075, 1997.
- [33] M. A. Green. *Solar Cells: Operating Principles, Technology, and System Applications.* Prentice-Hall, 1982.
- [34] C. Algora, E. Ortiz, I. Rey-Stolle, V. Díaz, R. Peña, V.M. Adreev, V.P. Khvostikov, and V.D. Rumyanstev. A GaAs solar cell with an efficiency of 26.2% at 1000 suns and 25.0% at 2000 suns. *IEEE Transactions on Electron Devices*, 48(5):840–844, 2001.

- [35] R. M. Swanson. The promise of concentrators. *Progress in Photovoltaics*, 8: 93–111, 2000.
- [36] T. Tiedje, E. Yablonovitch, G.D. Cody, and B.G. Brooks. Limiting efficiency of silicon solar cells. *IEEE Transactions on Electron Devices*, ED-31:711–716, 1984.
- [37] M.A. Green. Radiative efficiency of state-of-the-art photovoltaic cells. *Progress in Photovoltaics*, 10.1002, 2011.
- [38] B.M. Kayes. personal communication, 2013.
- [39] B.M. Kayes, Nie H., R. Twist, S.G. Spruytte, F. Reinhardt, I.C. Kizilyalli, and G.S. Higashi. 27.6% conversion efficiency, a new record for single-junction solar cells under 1 sun illumination. *Proc. of 37th IEEE Photovoltaic Specialists Conference*, 2011.
- [40] O. D. Miller, E. Yablonovitch, and S. R. Kurtz. Strong internal and external luminescence as solar cells approach the Shockley-Queisser limit. *Photovoltaics, IEEE Journal of*, 2(3):303–311, July 2012.
- [41] U. Strauss, W. W. Ruhle, and K. Kohler. Auger recombination in intrinsic GaAs. *Applied Physics Letters*, 62(55), 1993.
- [42] J. Nelson. *The Physics of Solar Cells*. Imperial College Press, 2003.
- [43] M.A. Steiner, J.F. Geisz, I. García, D.J. Freidman, A. Duda, and S.R. Kurtz. Optical enhancement of the open-circuit voltage in high quality GaAs solar cells. *Journal of Applied Physics*, 113:123109, 2013.
- [44] S.M. Sze and K.K. Ng. *Physics of Semiconductor Devices*. Wiley-Interscience, 1998.
- [45] H.R. Stuart and D.G. Hall. Thermodynamic limit to light trapping in thin planar structures. *Journal of the Optical Society of America A*, 14(11):3001–3008, 1997.

- [46] I. Schnitzer, E. Yablonovitch, C. Caneau, and T.J. Gmitter. Ultrahigh spontaneous emission quantum efficiency, 99.7% internally and 72% eternally, from AlGaAs/GaAs/AlGaAs double heterostructures. *Applied Physics Letters*, 62(2):131–133, 1992.
- [47] G.L. Araújo and A. Martí. Limiting efficiencies of GaAs solar cells. *IEEE Transactions on Electron Devices*, 37(5):1402–1405, 1990.
- [48] J.M. Gordon, E.A. Katz, D. Feuermann, and M. Huleihil. Toward ultrahigh-flux photovoltaic concentration. *Applied Physics Letters*, 84(18):3642–3644, 2004.
- [49] I. Luque-Heredia, R. Cervantes, and Quéméré. Goulven. A sun tracking error monitor for photovoltaic concentrators. In *Photovoltaic Energy Conversion, Conference Record of the 2006 IEEE 4th World Conference on*, volume 1, pages 706–709, May 2006.
- [50] R. J. Nelson and R.G. Sobers. Minority-carrier lifetime and internal quantum efficiency of surface-free GaAs. *Journal of Applied Physics*, 49(12), 1978.
- [51] J.M. Olson, R.K. Ahrenkiel, D.J. Dunlavy, B. Keyes, and A.E. Kibbler. Ultralow recombination velocity at Ga_{0.5}In_{0.5}P/GaAs heterointerfaces. *Applied Physics Letters*, 55(12), 1989.
- [52] R.K. Ahrenkiel, D.J. Dunlavy, B. Keyes, S.M. Vernon, T.M. Dixon, S.P. Tobin, K.L. Miller, and R.E. Hayes. Ultralong minority-carrier lifetime epitaxial GaAs by photon recycling. *Applied Physics Letters*, 55(11), 1989.
- [53] M. Deopura, C.K. Ullal, B. Temelkuran, and Y. Fink. Dielectric omnidirectional visible reflector. *Optics Letters*, 26(15):1197–1199, 2001.
- [54] H. Kuhn and B.A. Wilson. Reflectivity of thin silver films and their use in interferometry. *Proceedings of the Physical Society B*, 63, 1950.
- [55] S.J. Orfanidis. *Electromagnetic Waves and Antennas*. 2010. (www.ece.rutgers.edu/~orfanididi/ewa/).

- [56] R.T. Ross. Some thermodynamics of photochemical systems. *Journal of Chemical Physics*, 46(12):4590–4593, 1967.
- [57] O. Miller. *Photonic Design: From Fundamental Solar Cell Physics to Computational Inverse Design*. PhD thesis, University of California, Berkeley, 2012.
- [58] M. A. Green, K. Emery, Y. Hishikawa, W. Warta, and E. D. Dunlop. Solar cell efficiency tables (version 43). *Progress in Photovoltaics*, 22(1):1–9, 2014.
- [59] A. Luque. The confinement of light in solar cells. *Solar Energy Materials*, 23, 1991.
- [60] W.T. Welford and R. Winston. *High Collection Nonimaging Optics*. Academic Press, 1989.
- [61] J. H. Atwater, P. Spinelli, E. Kosten, J. Parsons, C. Van Lare, J. Van de Groep, J. Garcia de Abajo, A. Polman, and H. A. Atwater. Microphotonic parabolic light directors fabricated by two-photon lithography. *Applied Physics Letters*, 99(15):151113, 2011.
- [62] M. Deopura, C.K. Ullal, B. Temelkuran, and Y. Fink. Dielectric omnidirectional visible reflector. *Optics Letters*, 26(15):1197–1199, 2001.
- [63] Y. Fink, S. Winn, J. N. ad Fan, C. Chen, J. Michel, J.D. Joannopoulos, and E.L. Thomas. A dielectric omnidirectional reflector. *Science*, 282:1679–1682, 1998.
- [64] B.E.A. Saleh and M.C. Teich. *Fundamentals of Photonics, 2nd Ed*. Wiley, 2007.
- [65] S. Fahr, C. Ulbrich, T. Kirchartz, U. Rau, C. Rockstuhl, and F. Lederer. Rugate filter for light-trapping in solar cells. *Optics Express*, 16(13):9332–9343, 2008.
- [66] C. Ulbrich, S. Fahr, J. Upping, M. Peters, T. Kirchartz, C. Rockstuhl, R. Wehrspohn, A. Gombert, F. Lederer, and U. Rau. Directional selectivity and ultra-light-trapping in solar cells. *Physics Status Solidi A*, 205(12):2831–2843, 2008.

- [67] B. G. Bovard. Rugate filter theory: an overview. *Applied Optics*, 32(28):5427–5442, 1993.
- [68] W. H. Southwell. Using apodization functions to reduce sidelobes in rugate filters. *Applied Optics*, 28(23):5091–5094, 1989.
- [69] W. H. Southwell. Gradient-index antireflection coatings. *Optics Letters*, 8(11):584–586, 1983.
- [70] W. J. Gunning, R. L. Hall, F. J. Woodberry, W. H. Southwell, and N. S. Gluck. Codeposition of continuous composition rugate filters. *Applied Optics*, 28(14):2945–2948, 1989.
- [71] J.-S. Chen, S. Chao, J.-S. Kao, H. Niu, and C.-H. Chen. Mixed films of TiO₂—SiO₂ deposited by double electron-beam coevaporation. *Applied Optics*, 35(1):90–96, 1996.
- [72] H. Demiryont. Optical properties of SiO₂-TiO₂ composite films. *Applied Optics*, 24(16):2647–2650, 1985.
- [73] M.A. Green. Radiative efficiency of state-of-the-art photovoltaic cells. *Progress in Photovoltaics*, 10.1002, 2011.
- [74] J. N. Munday. The effect of photonic bandgap materials on the shockley-queisser limit. *Journal of Applied Physics*, 112(6):064501, 2012.
- [75] A. Braun, E.A. Katz, D. Feuermann, B.M. Kayes, and J. M. Gordon. Photovoltaic performance enhancement by external recycling of photon emission. *Energy and Environmental Science*, 6:1499–1503, 2013.
- [76] J.F. Geisz, M.A. Steiner, I. García, S.R. Kurtz, and D.J. Freidman. Enhanced external radiative efficiency for 20.8% efficient single-junction GaInP solar cells. *Applied Physics Letters*, 103(4), 2013.
- [77] S.P. Tobin, S.M. Vernon, C. Bajgar, S.J. Wojtczuk, M.R. Melloch, A. Keshavarzi, T.B. Stellwag, S. Venkatensan, M.S. Lundstrom, and K.A. Emery.

- Assessment of MOCVD- and MBE-grown GaAs for high-efficiency solar cell applications. *IEEE Transactions on Electron Devices*, 37(2):469–477, 1990.
- [78] M.T. Sheldon, C.N. Eisler, and H.A. Atwater. GaAs passivation with tri-octylphosphine sulfide for enhanced solar cell efficiency and durability. *Advanced Energy Materials*, 2(3):339–344, 2012.
- [79] A. Niv, Z. R. Abrams, M. Gharghi, C. Gladden, and X. Zhang. Overcoming the bandgap limitation on solar cell materials. *Applied Physics Letters*, 100(8):083901, 2012.
- [80] S. Larouche and L. Martinu. OpenFilters: open-source software for the design, optimization, and synthesis of optical filters. *Applied Optics*, 47(13), 2008.
- [81] J. Zhao, A. Wang, M.A. Green, and F. Ferrazza. Novel 19.8% efficient honeycomb textured multicrystalline and 24.4% monocrystalline silicon solar cells. *Applied Physics Letters*, 73:1991–1993, 1998.
- [82] Sanyo. World record cell press release. 2014.
- [83] Ol. Höhn, T. Kraus, G. Bauhuis, U. T. Schwarz, and B. Bläsi. Maximal power output by solar cells with angular confinement. *Optics Express*, 22(S3):A715–A722, May 2014.
- [84] A. Richter, S.W. Glunz, F. Werner, J. Schmidt, and A. Cuevas. Improved quantitative description of auger recombination in crystalline silicon. *Physical Review B*, 86:165202, Oct 2012.
- [85] A. Richter, M. Hermle, and S.W. Glunz. Reassessment of the limiting efficiency for crystalline silicon solar cells. *IEEE Journal of Photovoltaics*, 3(4):1184–1191, Oct 2013.
- [86] P.J. Cousins, D.D. Smith, Hsin-Chiao Luan, J. Manning, T.D. Dennis, A. Waldhauer, K.E. Wilson, G. Harley, and W.P. Mulligan. Generation 3: Improved

- performance at lower cost. In *Photovoltaic Specialists Conference (PVSC), 2010 35th IEEE*, pages 000275–000278, June 2010. doi: 10.1109/PVSC.2010.5615850.
- [87] P. Bermel, C. Luo, L. Zeng, L. C. Kimerling, and J. D. Joannopoulos. Improving thin-film crystalline silicon solar cell efficiencies with photonic crystals. *Optics Express*, 15(25):16986–17000, 2007.
- [88] M. Rüdiger, J. Greulich, A. Richter, and M. Hermle. Parameterization of free carrier absorption in highly doped silicon for solar cells. *IEEE Transactions on Electron Devices*, 60(7):2156–2163, July 2013.
- [89] A. Schenk. Finite-temperature full random-phase approximation model of band gap narrowing for silicon device simulation. *Journal of Applied Physics*, 84(7):3684–3695, 1998.
- [90] M. Reaz Shaheed and C.M. Maziar. Modeling plasma-induced bandgap narrowing effects for accurate simulation of advanced silicon bipolar transistors. *Solid-State Electronics*, 37(9):1589 – 1594, 1994.
- [91] P. P. Altermatt, A. Schenk, F. Geelhaar, and G. Heiser. Reassessment of the intrinsic carrier density in crystalline silicon in view of band-gap narrowing. *Journal of Applied Physics*, 93(3):1598–1604, 2003.
- [92] A.B. Sproul and M.A. Green. Intrinsic carrier concentration and minority carrier mobility of silicon from 77 to 300 k. *Journal of Applied Physics*, 73(3):1214–1225, Feb 1993.
- [93] M. A. Green. Self-consistent optical parameters of intrinsic silicon at 300k including temperature coefficients. *Solar Energy Materials and Solar Cells*, 92(11):1305 – 1310, 2008.
- [94] Z.C. Holman, A. Descoeur, L. Barraud, F.Z. Fernandez, J.P. Seif, S. De Wolf, and C. Ballif. Current losses at the front of silicon heterojunction solar cells. *IEEE Journal of Photovoltaics*, 2(1):7–15, Jan 2012. ISSN 2156-3381. doi: 10.1109/JPHOTOV.2011.2174967.

- [95] *Standard Tables for Reference Solar Spectral Irradiances: Direct Normal and Hemispherical on 37° Tilted Surface.*, volume 12 of *ASTM Standard G173-03*. ASTM International, West Conshocken, PA, 10.1520/g0173-03r edition, 2003.
- [96] M. A. Green. *Third Generation Photovoltaics: Advanced Solar Energy Conversion*. Springer, 2006.
- [97] C. H. Henry. Limiting efficiencies of ideal single and multiple energy gap terrestrial solar cells. *Journal of Applied Physics*, 51(8):4494–4500, 1980.
- [98] R. R. King, D. C. Law, K. M. Edmondson, C. M. Fetzer, G. S. Kinsey, H. Yoon, R. A. Sherif, and N. H. Karam. 40% efficient metamorphic gainp gainasge multijunction solar cells. *Applied Physics Letters*, 90(18):183516, 2007.
- [99] R. R. King, D. Bhusari, D. Larrabee, X.-Q. Liu, E. Rehder, K. Edmondson, H. Cotal, R. K. Jones, J. H. Ermer, C. M. Fetzer, D. C. Law, and N. H. Karam. Solar cell generations over 40% efficiency. *Progress in Photovoltaics*, 20(6): 801–815, 2012.
- [100] S. Kurtz and J. Geisz. Multijunction solar cells for conversion of concentrated sunlight to electricity. *Optics Express*, 18(S1):A73–A78, 2010.
- [101] M. Yamaguchi. III-V compound multi-junction solar cells: present and future. *Solar Energy Materials and Solar Cells*, 75(1):261 – 269, 2003.
- [102] G. S. Kinsey and K. M. Edmondson. Spectral response and energy output of concentrator multijunction solar cells. *Progress in Photovoltaics*, 17(5):279–288, 2009.
- [103] E.C. Warmann. *Design strategies for ultra-high efficiency photovoltaics*. PhD thesis, California Institute of Technology, 2014.
- [104] M.A. Green, G. Conibeer, D. Knig, S. Shrestha, Shujuan Huang, P. Aliberti, L. Treiber, R. Patterson, B.P. Veetil, A. Hsieh, Yu Feng, A. Luque, A. Marti, P.G. Linares, E. Cnovas, E. Antolin, D.F. Marrn, C. Tablero, E. Hernndez, J.-F.

- Guillemoles, L. Huang, A. Le Bris, T. Schmidt, R. Clady, and M. Tayebjee. Hot carrier solar cells: Challenges and recent progress. In *Photovoltaic Specialists Conference (PVSC), 2010 35th IEEE*, pages 000057–000060, June 2010.
- [105] A. Luque, A. Martí, and C. Stanley. Understanding intermediate band solar cells. *Nature Photonics*, 6:146–152, 2012.
- [106] D. Verma, T.O. Saetre, and O.-M. Midtgard. Review on up/down conversion materials for solar cell application. In *Photovoltaic Specialists Conference (PVSC), 2012 38th IEEE*, pages 002608–002613, June 2012.
- [107] A. Martí and A. Luque. *Next Generation Photovoltaics: High Efficiency through Full Spectrum Utilization*. Wiley-VCH, 2004.
- [108] A.G. Imenes and D.R. Mills. Spectral beam splitting technology for increased conversion efficiency in solar concentrating systems: a review. *Solar Energy Materials and Solar Cells*, 84(1):19 – 69, 2004.
- [109] A. Goetzberger, J.C. Goldschmidt, M. Peters, and P. Löper. Light trapping, a new approach to spectrum splitting. *Solar Energy Materials and Solar Cells*, 92(12):1570 – 1578, 2008.
- [110] U. Ortabasi, A. Lewandowski, R. McConnell, Daniel J. Aiken, P.L. Sharps, and B.G. Bovard. Dish/photovoltaic cavity converter (pvcc) system for ultimate solar-to-electricity conversion efficiency-general concept and first performance predictions. In *Photovoltaic Specialists Conference, 2002. Conference Record of the Twenty-Ninth IEEE*, pages 1616–1620, May 2002.
- [111] E. Yablonovitch. Engineered omnidirectional external-reflectivity spectra from one-dimensional layered interference filters. *Optics Letters*, 23(21):1648–1649, 1998.
- [112] L. Miao, P. Jin, K. Kaneko, A. Terai, N. Nabatova-Gabain, and S. Tanemura. Preparation and characterization of polycrystalline anatase and rutile TiO₂ thin

- films by rf magnetron sputtering. *Applied Surface Science*, 212-213:255 – 263, 2003. 11th International Conference on Solid Films and Surfaces.
- [113] A. V. Tikhonravov, M. K. Trubetskov, and G. W. DeBell. Application of the needle optimization technique to the design of optical coatings. *Applied Optics*, 35(28):5493–5508, 1996.
- [114] W. G. Spitzer and J. M. Whelan. Infrared absorption and electron effective mass in n-type gallium arsenide. *Physical Review*, 114:59–63, 1959.
- [115] W.G. Spitzer, M. Gershenzon, C.J. Frosch, and D.F. Gibbs. Optical absorption in n-type gallium phosphide. *Journal of Physics and Chemistry of Solids*, 11 (3-4):339 – 341, 1959.
- [116] R. Braunstein. Intervalence band transitions in gallium arsenide. *Journal of Physics and Chemistry of Solids*, 8:280 – 282, 1959.
- [117] M. B. M. Rinzan, D. G. Esaev, A. G. U. Perera, S. G. Matsik, G. Von Winkel, A. Stintz, and S. Krishna. Free carrier absorption in Be-doped epitaxial AlGaAs thin films. *Applied Physics Letters*, 85(22):5236–5238, 2004.
- [118] J. W. Leem, Y. T. Lee, and J.S. Yu. Optimum design of InGaP/GaAs dual-junction solar cells with different tunnel diodes. *Optical and quantum electronics*, 41(8):605–612, 2009.
- [119] M. Hermle, G. Létay, S. P. Philipps, and A. W. Bett. Numerical simulation of tunnel diodes for multi-junction solar cells. *Progress in Photovoltaics*, 16(5): 409–418, 2008.